Preclinical Dynamic Contrast Enhanced Imaging for Longitudinal Biophysical Assessments of the Healthy and Malignant Vasculature after Radiotherapy

A DISSERTATION

SUBMITTED TO THE FACULTY OF THE GRADUATE SCHOOL OF THE UNIVERSITY OF MINNESOTA

BY

Jamison Brooks

IN PARTIAL FULFILMENT OF

THE REQUIREMENTS FOR THE DEGREE OF

DOCTOR OF PHILOSOPHY

Susanta K. Hui, PhD

* June 2021 (Month and year degree requirements were met)

Acknowledgements

I would like to thank Dr. Jerry Froelich for his continued financial support through funding from the Merle and Fern Loken Professorship in Radiologic Sciences and for his mentorship throughout my studies. I would like to thank my primary advisor Dr. Susanta Hui for financial support through NCI and NIH grants (R01CA154491, P30CA033572) and through ONCOTEST. I would also like to thank him for the extensive amount of time he committed to designing and supporting my studies. I would also like to thank Dr. Yoichi Watanabe for his mentorship and advice as my co-advisor.

Additionally, I would like to thank my many colleagues, collaborators, and dissertation committee members for their support, discussion, and enthusiasm for cancer research. Lastly, I would like to thank my family and friends for being in my life and encouraging me to pursue my research interests and goals.

Abstract

Dynamic contrast enhanced (DCE) imaging acquires time-lapsed images of intravenously injected contrast agents to quantify changes in their delivery to and clearance from the tissue. It is widely used in clinical imaging to assess tissue perfusion and vascular permeability. However, minimal work has been done using DCE in a murine model to better understand the effects of radiotherapy on the vasculature and tissue. This is due in part to a lack of DCE imaging systems with the resolution to directly observe the underlying changes in single-vessel structure and function. In this thesis, I develop and use macroscopic dynamic fluorescent imaging (DynFI) and microscopic quantitative multiphoton microscopy (QMPM). These DCE techniques identify changes in tissue perfusion several days after radiotherapy in the healthy bone marrow, leukemic bone marrow, and solid tumor tissue. DCE imaging can be performed using QMPM while simultaneously observing changes in the single-vessel characteristics for direct correlation. Using QMPM, changes in bone marrow vasculature were observed with the onset of acute myeloid leukemia (AML) and acute lymphoid leukemia (ALL). Changes included increased angiogenesis, permeability, decreased mean vessel diameter, decreased single-vessel blood flow, and decreased drug delivery. For mice bearing ALL, this resulted in reduced cellular uptake of a chemotherapy surrogate. The results identified potential biomarkers for leukemia using DCE imaging. Treatments ranging from 2 Gy to 10 Gy of total body irradiation (TBI) increased single-vessel blood flow and drug delivery for mice bearing AML and ALL 2 to 5 days after TBI. For mice bearing ALL, targeted 2 and 4 Gy radiotherapy resulted in improved cellular chemotherapy uptake. Additionally, increased survival was observed for mice bearing ALL when administering

4Gy TBI before chemotherapy compared to chemotherapy before 4Gy TBI. Finally, I develop DynFI with principal component analysis to rapidly identify changes in tumor vasculature before and 2 days after 10 Gy targeted radiotherapy. In conclusion, DCE analysis is an effective tool to measure tissue perfusion and vascular function. Increased availability of DCE imaging for preclinical models will allow for a better understanding of the underlying vascular changes that occur in a clinical setting.

Table of Contents

List of Tables

List of Figures

List of Abbreviations

ALL	acute lymphoblastic leukemia
AML	acute myeloid leukemia
BMV	bone marrow vasculature
CT	computed tomography
CTCs	circulating tumor cells
DCE	dynamic contrast enhanced
DynFI	dynamic Fluorescent Imaging
ICG	indocyanine green
K_{ep}	back flux constant
K_{trans}	kinetic transfer constant
LDRT	low dose radiation therapy
L-QMPM	longitudinal quantitative multiphoton microscopy
MOC	murine oral cancer
MRI	magnetic resonance imaging
PB	peripheral blood
PC1	first principal component
PC2	second principal component
PCA	principal component analysis
PH_{blood}	maximum concentration of injected fluorescent contrast in the vascular tissue
PH_{tissue}	maximum concentration of injected fluorescent contrast in the extravascular tissue
PH_{whole}	maximum concentration of injected fluorescent contrast in the extravascular and vascular tissue
QMPM	quantitative multiphoton microscopy
ROI	region of interest

TBI	total body Irradiation
TVR	tumor vascular response
t-LDRT	targeted low dose radiation therapy
v_{ec}	fraction of the extravascular space that is extracellular
WIS_{tissue}	accumulation rate of injected fluorescent contrast in the extravascular tissue
WIS_{whole}	accumulation rate of injected fluorescent contrast in the combined extravascular and vascular tissue
WT	wild type (control)

Chapter 1: Introduction

1.1 Tumor vasculature and drug delivery

1.1.1 The role of the vasculature in the tumor microenvironment

The vascular system is responsible for the delivery of oxygen and nutrients to the tumor microenvironment, where the rapid growth of tumor cells often creates high metabolic demand for oxygen and nutrients [1]. As a result, the formation of new vessels is critical for tumor progression. Tumor induced angiogenesis and vessel remodeling results in a variety of changes including vessel permeability, poor pericyte coverage, altered vessel diameter, and altered vessel spatial distribution [2-4]. Additionally, the tumor vasculature plays a direct role in supporting metastasis by allowing tumor cells to enter the blood and circulate to different regions of the body [5]. While vessel recruitment is necessary to support tumor growth, the unchecked angiogenesis of tumor supporting blood vessels results in heterogeneous vascular structures that have inadequate delivery of oxygen and poor chemotherapy delivery to tumor cells. This results in increased resistance chemotherapy and radiotherapy (RT) for many tumor cell types [6-8].

1.1.2 Vascular based strategies for the treatment of malignancies

In the last few decades, there has been increased emphasis on alternative combination-based therapies for the treatment of malignancies [9]. There are several potential combination treatments that are aimed at altering the vascular system to

improve treatment outcomes. One strategy involves damaging the vascular system to prevent delivery of oxygen and nutrients to malignancy to indirectly kill tumor cells [10, 11]. Other strategies aim to improve the delivery of oxygen and therapeutics to tumor cells to make standard RT or chemotherapy treatments more effective [7, 12].

The optimization of drug delivery is challenging because of the heterogeneity of malignant vasculature and the complex response of the vasculature to treatment [13]. To effectively optimize therapeutic delivery, both the pharmacokinetics of the therapeutics and the functional vascular characteristics (e.g., permeability, density, morphology, and blood flow) must be understood. Attempts to optimize the tumor vasculature on the basis of pharmacokinetics alone may result in further vascular dysfunction [12]. Alternatively, optimization based on solely the characteristics of the tumor vasculature does not account for the wide variety of sizes and types of therapeutics (targeted or non-targeted) [14]. Therefore, effective methods that simultaneously observe vascular functional characteristics and therapeutic pharmacokinetics are essential to condition the vasculature in combination therapy.

“Vascular normalization” is a strategy aimed at creating a more homogenous distribution of blood vessels in terms of vessel density, permeability, and blood flow by balancing proangiogenic and antiangiogenic signaling and other factors to improve drug delivery to malignancies [15]. This strategy has been used successfully in several solid tumor malignancies and has demonstrated how restoring the vascular structure to a state resembling healthy tissue improves standard chemotherapy delivery and treatment outcomes [16, 17]. However vascular normalization is challenging because of the number of pro-angiogenic pathways and the complex response of different individual tumor environments to treatment. Knowledge of the timing of optimal vascular normalization after vascular conditioning is needed to ensure improved efficacy in

combination with chemotherapy or RT, and methods of assessing vascular function are necessary, but not simple or straightforward [18].

An alternative strategy to vascular normalization is the “pro-vascular” approach. Compared to healthy tissues, most solid tumors are characterized by tumor regions or entire tumors with poor vascular blood flow [19]. In solid tumors there is a combination of immature capillaries due to angiogenesis, and more mature vessels pre-existing capillaries, arterioles, and venules [20]. These mature vessels are often more capable of vasoconstriction and vasodilation than newly formed vessels [21, 22]. Provascular therapies exploit vasodilation of mature blood-supplying tumor vessels to transiently improve vessel blood flow and in turn improve the delivery of oxygen or chemotherapy. Examples of this include certain regimens of hyperthermia and regulation of nitric oxide and endothelin-1 to impact vasodilation [7, 23].

Compared to vascular normalization, pro-vascular strategies are less dependent on the optimization of the treatment regimen to “fine tune” the vascular response. Vasodilation can transiently increase blood flow and in turn directly enhance chemotherapy delivery. However, the heterogenous nature of tumor blood vessels may make this type of treatment ineffective for regions where there is low vascular density and does not necessarily promote homogenous blood flow and drug delivery through to the tumor [20].

1.1.3 The response of the solid tumor vasculature to radiotherapy

Many studies have been performed measuring the impact of radiotherapy on the tumor vasculature and blood flow. However, the response of the tumor vasculature to radiotherapy is complex and depends on many factors such as dose, timing, and tumor type. A recent study identified significant increases in cell death several days after

treatment with 15 or 20 Gy radiotherapy compared to immediately after treatment. No differences were noticed in cell death following 10 Gy treatments. 20 Gy treatments also resulted in reduced tumor perfusion, and increased HIF-1α and VEGF after radiotherapy, suggesting that enhanced tumor cell death several days after radiotherapy may be due to vascular damage and poor vascular transport of oxygen [10]. Additionally other studies have noticed differences in the response of the tumor vasculature to radiotherapy dose and fractionation, with more severe longer lasting changes occurring at higher doses and minimal vascular changes occurring at doses of 10 Gy or less [24-26]. A review by Park, et al. summarized the results of 43 representative studies on tumor vasculature and concluded that, in general, radiotherapy from 5-10 Gy in a single dose causes minimal damage, but higher doses than 10 Gy can induce severe vascular damage that reduce blood flow [11].

At lower doses, several studies have noticed increases in vascular tumor perfusion after irradiation, either through vascular normalization or through transient pro-vascular improvements in blood perfusion [27-30]. One study has demonstrated a pro-vascular effect using low-to-moderate dose radiotherapy in mouse hepatocarcinoma tumors. Irradiation resulted in immediate vasodilation in tumor supporting arterioles for 2-3 days which led to transient improvements in tumor perfusion and better tumor control with successive 6 Gy treatments. Vasodilation was shown to be directly dependent on increased endothelial expression of nitric oxide synthase and decreasing caveolin-1 expression after irradiation [31]. These study demonstrates that the proper dose of RT has the potential to transiently improve vascular blood perfusion in solid tumor malignancies and demonstrates the variety of vascular responses that can occur depending on the tumor type, dose, timing and dose fractionation.

1.1.4 The role of the bone marrow vasculature in the treatment of leukemia

While much work has been done studying the impact of the vascular system in the treatment of solid tumor malignancies, less work has been done developing vascular based treatment approaches for leukemia. This is in part due to the relatively large vascular blood volume and high blood flow in the healthy bone marrow [32] as well as the more systemic distribution of leukemia throughout the body. In preclinical studies, vascular leakiness, alterations in vascular structure, and angiogenesis have all been shown with the onset of leukemia. Studies have demonstrated that leukemia induced bone marrow vasculature (BMV) remodeling decreases chemotherapy delivery to leukemia cells residing in the bone marrow of mice bearing acute myeloid leukemia (AML) and that inhibition of leukemia induced BMV remodeling improves chemotherapy delivery and overall survival efficacy when used with chemotherapy [3, 8]. Additional studies using human AML have reported vascular alterations that result in poorly distributed blood flow, similarly to solid tumor models [2]. In patients with leukemia, angiogenesis is commonly observed [33] and increased hypoxia in the bone marrow has been reported, due in part to similar vascular alterations as seen in preclinical studies [34].

Despite the success of anti-angiogenic therapies with some solid tumor malignancies, initial vascular based treatments that have attempted to normalize the leukemic BMV using anti-angiogenic therapies have not improved patient outcomes for leukemia [35, 36]. Several explanations for this are possible including; 1) multiple possible pathways for vascular regulation, 2) the complex response of the vascular system to treatment [37], and 3) a lack of methods to assess the treatment response of the BMV to determine the optimal dosage and timing.

While studies have been performed characterizing changes in the vascular system during RT in solid tumor malignancies, the effects of RT on the malignant BMV have not been characterized. This is likely because RT is not commonly used for the initial clinical treatment of many hematological malignancies. High-dose total body irradiation (TBI) treatments are used for several high-risk hematopoietic malignancies in patients, often as a myeloablative conditioning regimen prior to hematopoietic stem cell transplantation [38]. However, RT is not often considered for induction therapy in many hematopoietic malignancies like leukemia [39]. For induction therapy, non-myeloablative low-dose radiotherapy (LDRT) is a potential option for combination with chemotherapy and has several attractive benefits, including the radiosensitivity of hematological malignancies, the ability to precisely target regions of high disease burden, and lower toxicity compared to myeloablative high-dose RT [40, 41]. Such advantages make LDRT a possible candidate for combination therapy; however, the response of the BMV to LDRT is largely unknown and needs to be considered to optimize the delivery of therapeutics to the malignant bone marrow.

1.2 Dynamic contrast enhanced imaging

1.2.1 Dynamic contrast enhanced imaging tissue uptake and clearance

One effective clinical technique to assess the function of the tumor vasculature is dynamic contrast-enhanced (DCE) imaging with modalities such as magnetic resonance imaging (MRI) or computed tomography (CT), or macroscopic dynamic fluorescent imaging (DynFI). DCE imaging acquires time-lapsed images of intravenously injected molecular contrast agents to quantify changes in their delivery to the tissue [42]. Alterations in BMV function have been shown in hematological malignancies, tumor bone metastasis, and bone diseases by DCE-MRI and DCE-CT [43-46].

Limitations to DCE imaging include; 1) inadequate resolution required to directly observe the features of capillary-sized vessels, making direct observations of the underlying vascular functional characteristics difficult or impossible[47], 2) the resolution makes it challenging to observe tracer uptake in the bone marrow of a mouse model, limiting usefulness in a preclinical setting for hematological applications.

Despite being unable to directly observe the underlying vascular characteristics using DCE imaging, features of the vascular structure can be quantified using the proper molecular contrast agents and time-lapsed imaging analysis methods. These changes can be quantified in several ways, including semi-quantitative descriptive curve analysis, and mathematical compartment modeling to obtain parameters such as vascular permeability, blood flow, vascular blood volume, and extravascular tissue space [42].

1.2.2 Compartment modeling using the Toft model and semi-quantitative curve analysis

Compartmental kinetic modeling has been used frequently for clinical DCE imaging to understand changes in the tissue and vasculature that influence the uptake and clearance of molecular contrast agents. Several models have been developed for DCE imaging applications. For the intravital multiphoton microscopy imaging performed in this work, Toft's model is used [48] which assumes no vascular volume is present in the tissue regions. The rate of exchange between the local vasculature and the tissue compartment assumes two-way passive equal transport of molecular contrast from the blood plasma, to the extravascular extracellular space through a semi-permeable membrane and is shown in Equation 1-1. Negligible cellular uptake of the molecular contrast and a constant total tissue volume is assumed.

$$\frac{dC_t(t)}{dt} = (K_{trans})\left(C_p(t) - \frac{C_t(t)}{v_{ec}}\right) \qquad (1\text{-}1)$$

Where $C_p(t)$ is the concentration of molecular contrast in the blood plasma of the local vasculature and $C_t(t)$ is the concentration of the extravascular tissue. K_{trans} is the transfer rate of a molecular agent between the blood plasma and extracellular extravascular tissue. However, the extracellular extravascular tissue region cannot be directly identified from images, so the fraction of the extravascular space that is extracellular (v_{ec}) is solved for using the model to account for changes in tissue cellularity. An additional term K_{ep} is called the backflux rate and identifies the rate of transfer from the extravascular tissue compartment to the blood plasma for a given tissue concentration. It is equal to K_{trans}/ v_{ec} (Figure 1-1).

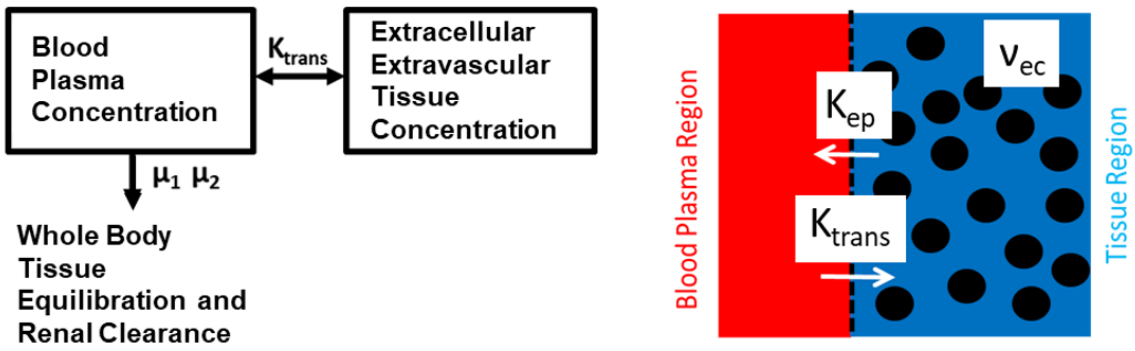

Figure 1-1: Two diagrams illustrating the Toft model and primary parameters Ktrans, vec, and Kep. The diagram on the right illustrates the blood plasma in red, extravascular extracellular tissue in blue, and extravascular cellular tissue region as black circles.

One additional model that has relevance to the bone marrow is the extended toft model [48], which accounts for changes in the vascular volume within the whole bone marrow tissue by adding a term into the model for fractional vascular volume. However, an initial estimate of the fractional vascular volume must be made to fit the extended toft model directly to the extravascular tissue concentration instead of the whole tissue concentration (blood and tissue regions combined). For imaging of the bone marrow in the calvarium, quantitative measurements of the fractional vascular volume have not

been made, making validation of any estimates challenging. Furthermore, observations of large relative differences in vascular volume between the femur and calvarium bone marrow tissues have been made [49], making estimates in blood volume in other bone marrow regions irrelevant for estimating the blood volume the calvarium [50]. For these reasons, we chose to analyze the data using the Toft model rather than the extended Toft model in this work.

For all multiphoton microscopy data in this work, a value of 0.4 for the hematocrit was used to convert the molecular contrast concentration in the vascular tissue to $C_p(t)$. $C_p(t)$ is modeled by a summation of two separately weighted exponential decay curves (Equation 1-2). This allows accurate function fitting to plasma concentration data when renal clearance and leakage of molecular contrast into tissues throughout the body are occurring at different rates.

$$C_p(t) = \sum_{i=1}^{2}[(A_i)(e^{-\mu_i * t})] \quad (1\text{-}2)$$

Where A_i and μ_i are the scaling coefficient and attenuation coefficient for the ith exponential plasma concentration curve, respectively. Substituting Equation 1-2 into Equation 1-1 and setting the initial tissue concentration equal to zero to obtains Equation 1-3.

$$C_t(t) = K_{trans} \sum_{i=1}^{2} \left[\left(\frac{A_i}{(K_{trans}/\nu_{ec}) - \mu_i} \right) \left(e^{-\mu_i * t} - e^{-(K_{trans}/\nu_{ec}) * t} \right) \right] \quad (1\text{-}3)$$

The vascular and extravascular tissue regions of images are identified and the mean signal intensity from these regions is calculated. The mean signal intensity is proportional to the molecular concentration for fluorescent imaging. A_1, A_2, μ_1, and μ_2 can be identified by fitting Equation 1-2 to the blood plasma concentration data through error minimization algorithms. Once A_1, A_2, μ_1, and μ_2 are known, they can be

incorporated in to Equation 1-3 to identify K_{trans}, v_{ec}, by fitting the equation to the extravascular tissue concentration data through least square fitting. It can be shown that K_{trans} is approximately equal to the average vascular permeability times the average vascular surface area per volume of tissue when the majority of the initial molecular contrast just after intravenous injection remains in the vasculature tissue and does not entirely permeate into the tissue bed before reaching the veins [48] (Equation 1-4). This will be true in cases where the relative leakage rage of molecular contrast is much slower than the contrast flow through the vasculature (i.e. large sized molecular contrast and well perfused tissue such as the bone marrow).

$$Permeability = \frac{K_{trans}}{Vascular\ Surface\ Area} \qquad (1\text{-}4)$$

Clinical DCE imaging will identify $C_p(t)$ through contouring of an arterial input function and sampling the concentration of the arterial blood. However, this is not possible for microscopic imaging methods, where only the local vasculature in the tissue can be observed. Differences between the arterial blood and local blood molecular contrast concentrations are possible, making direct comparisons between macroscopic and microscopic modeling parameters challenging. In the case of high blood flow with slow leakage of contrast to the extravascular tissue (i.e. blood flow>>vascular leakage rate), the arterial blood concentration will be equal to the vascular tissue blood concentration and the modeling parameters can be directly compared. Alternatively, in the case of low blood flow and fast leakage of contrast to the extravascular tissue (i.e. blood flow<< vascular leakage rate), the arterial blood concentration will not match the vascular tissue blood concentration before the extravascular tissue concentration reaches steady state with the arterial blood plasma concentration. In this context,

modeling using arterial blood or the vascular tissue blood concentration to solve for K_{trans} will give different results.

1.2.3 The effects of total body irradiation on DCE imaging

No work has been published using clinical DCE imaging in the bone marrow of patients receiving TBI. DCE imaging using MRI has been able to detect increased peak contrast uptake in the bone marrow after TBI using a macromolecular iron contrast agent 1 to 2 days after completion of 3 fractions of 4Gy TBI in rabbits [51]. Additional studies observed increased K_{trans}, and v_{ec} 4 to 7 days after 6 Gy TBI treatments in rats using the extended Toft's model with a small molecular weight gadolinium-based contrast agent (Multihance^{TM}). Decreases in K_{ep} and blood volume were also observed [52]. Such observations suggest increased vascular permeability and/or increased vascular surface area due to vascular damage.

1.2.4 Clinical DCE imaging for leukemia and lack of preclinical translation

DCE-MRI imaging with a small molecular weight (938 Da) gadolinium contrast agents in patients with AML after standard induction chemotherapy has been shown to have predictive value for disease-free survival [43], demonstrating the prognostic value of DCE imaging for leukemia. DCE imaging using the same contrast agent has also identified increased contrast peak height and wash-in slope (rate of initial accumulation) in the bone marrow of patients with AML compared to healthy volunteers [53]. Increased blood flow and blood volume have been proposed as reasons for changes in peak height and wash-in slope, respectively. However, the results of these experiments are not in agreement with observations of poor chemotherapy delivery in mice bearing leukemia shown in section 1.1.4. Additionally the causes behind changes in contrast uptake and clearance are not always easily interpreted as they depend on many factors

such as BMV permeability, BMV surface area, diffusion, convection and interstitial pressure [54]. The relatively poor spatial resolution of clinical imaging modalities combined with the known vascular heterogeneity in areas of malignancy highlight the need for better preclinical methodologies to interpret clinical imaging. A quote from Jain et al. [12] in one of the primary publications regarding vascular normalization treatment summarizes this problem:

"As we interpret these human data obtained from MRI, PET, and CT, two key limitations of these imaging methods must be kept in mind. First, because most of these methods yield a parameter that depends on both blood flow and permeability [K_{trans}], the blood flow and permeability cannot be calculated unambiguously. Second, tumor blood flow is highly heterogeneous. It is not the total blood flow, but the distribution of blood flow, that determines the distribution of a drug or oxygen in tumors. Therefore, the global (total) blood flow, as estimated by the currently available resolution of MRI, CT, or PET, does not inform us about the degree of spatial heterogeneity in vascular normalization or drug distribution... Thus, improved imaging techniques, which can measure the spatial and temporal changes in blood flow and other physiological parameters with higher resolution, are needed to definitively establish the effects of antiangiogenic treatment on vascular function in human tumors growing at different sites."

The lack of agreement between clinical and preclinical information demonstrate the need for preclinical methodology capable of performing clinically relevant contrast-based time-lapsed imaging, while directly observing BMV alterations and tissue drug uptake at the single-vessel resolution. This would allow a better understanding of the underlying factors influencing DCE imaging and ensure accurate interpretations of changes in DCE parameters found in patients with AML.

1.3 Intravital fluorescent multiphoton microscopy

1.3.1 Intravital calvarium imaging

In the previous sections, the need for vascular imaging techniques at higher resolution to better understand the effectiveness of vascular based treatments is outlined. Intravital fluorescent multiphoton microscopy is one such approach that can be used to observe the small bone marrow compartments in the calvarium in mice. This approach has been shown to be an effective way to observe bone marrow related changes in live mice. The calvarium bone region is used because 1) it contains sinusoidal vessels similar to those in other hematopoietic bone marrow regions [55, 56], 2) it has similar proportions of hematopoietic stem cells and similar hematopoietic reconstitution potential compared to bone marrow regions that are considered the primary sites of hematopoiesis [49], and 3) it is a flat, thin, superficial bone requiring minimal invasive surgery before live imaging. Many studies have utilized intravital calvarium imaging to observe changes in vascular morphology, single-vessel blood flow, and vascular permeability with the onset of leukemia as well as for other bone marrow related applications [2, 3, 8, 49, 56, 57].

1.3.2 Dynamic multiphoton microscopy to measure vascular permeability and drug delivery

Fluorescent multiphoton imaging is one microscopy technique that has gained popularity for intravital imaging in the last several decades. Compared to standard fluorescent confocal microscopy, multiphoton microscopy has several advantages including 1) increased imaging depth, 2) reduced out of field phototoxicity, and 3) the acquisition of second harmonic generation from the collagen in the bone of the calvarium [58, 59].

Fluorescent dextran conjugates of a variety of molecular weights are commonly used for multiphoton microscopy as a contrast agent. Vascular leakage of dextran with molecular weights up to 150 kDa has been observed in the bone marrow [3] due to the presence of highly permeable sinusoidal vessels [57].The macromolecular size of 150kDa dextran makes it ideal for measurements of vascular permeability [3, 57]. In comparison to 150 kDa sized dextran, 4kDa sized dextran rapidly permeates the BMV, and it is closer in molecular weight to typical chemotherapies used in the treatment of leukemia such as daunorubicin (563.98 Da) or cytarabine (243.22 Da) [39]. It is additionally closer in size to clinically used gadolinium-based contrast agents for DCE imaging with MRI (Gd-DTPA 547.6 Da). Compared to chemotherapy, 4kDa dextran has a minimal effect on the bone marrow microenvironment [60], making it ideal for longitudinal studies as a drug surrogate and is useful for comparison with DCE imaging.

While multiphoton microscopy has the resolution to distinguish between the blood and tissue regions, analysis of vascular leakiness is typically done in a semi-quantitative fashion [61] or by obtaining the slope of the ratio of the extravascular tissue signal intensity to the blood signal intensity after injection of molecular contrast agents and equating that ratio to vascular permeability [3, 62]. However, this ratio method is only accurate very early after contrast injection, when the accumulation of contrast in the extravascular tissue space is minimal. Additionally, it cannot identify the extravascular extracellular tissues space parameter, which is dependent on cellularity and changes dramatically during RT. Models like the Toft's model or extended Toft's model[48] can be applied to multiphoton microscopy to identify the extravascular extracellular space and to make dynamic microscopy imaging more quantitative. Additionally, the use of these models with microscopy may give insight into the accuracies of commonly used MRI

based modeling approaches through direct visualization of the vascular and extravascular tissue regions [47].

1.3.3 Assessments of single-vessel blood flow

An additional advantage of multiphoton microscopy is its ability measure the velocity of cells flowing through the individual blood vessels. Several works have used measurements of the velocity of cells flowing through the vasculature as measurements of single-vessel blood flow. This can be done using scanning confocal or multiphoton microscopy by using repeated scans in parallel with the center of the vessels after molecular fluorescent contrast has been injected (Figure 1-2) [56]. Cells in the blood vessels are observed as dark streaks on plots of position versus time. A correction factor is often applied to measurements to account for differences between the central velocity of cells and the corrected mean velocity of cells flowing through the microvasculature and is given by Equation 1-5 [63, 64].

$$V_{corrected} = \frac{V_{centerline}}{\alpha} \qquad (1\text{-}5)$$

Where $V_{centerline}$ is the velocity of cells as measured at the center of the measured vessel. α is a correction factor calculated from the vessel diameter (D) by Equation1-6.

$$\alpha = 1.3 \; when \; D < 10\mu m$$

$$linear \; extrapolation \; 1.3 < \alpha < 1.6 \; when \; 10\mu m < D < 15\mu m$$

$$\alpha = 1.6 \; when \; D > 15 \; \mu m \qquad (1\text{-}6)$$

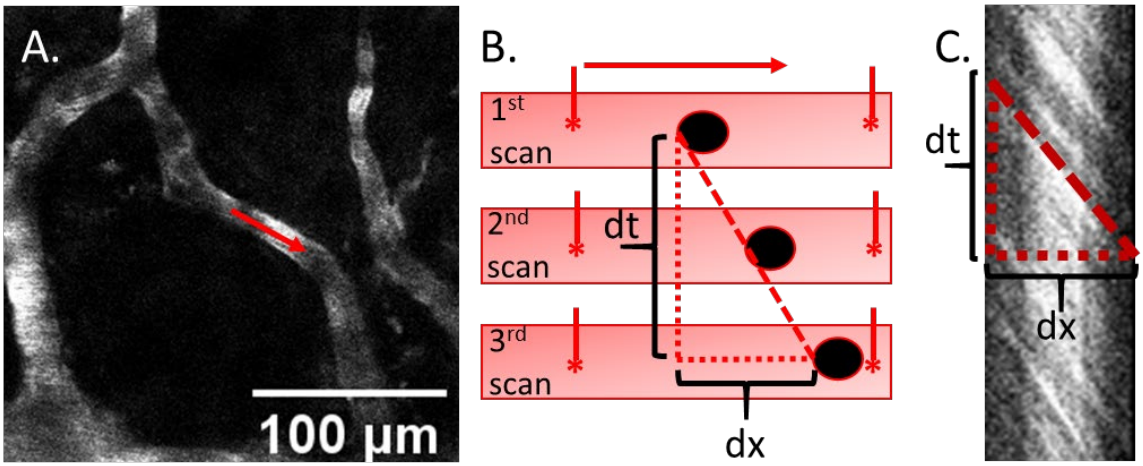

Figure 1-2: (A) An image of the BMV in the calvarium of a mouse injected with a fluorescent molecular contrast agent. The red arrow indicates the region designated to perform repeated centerline blood vessel scanning by the multiphoton microscopy system. (B) A diagram of repeated centerline blood vessel scanning showing a cell (black) flowing through a vessel with fluorescent contrast scanned repeatedly by the excitation laser (red). (C) As the cell moves through the vessel they will show up as dark streaks on the position versus time plot for the centerline scan of the vessel depicted in A.

Chapter 2: QMPM imaging of the leukemic bone marrow vasculature reveals benefits of low-dose radiotherapy

This chapter is based largely on the following published work: Brooks J, Kumar B, Zuro DM, Raybuck JD, Madabushi SS, Vishwasrao P, Parra LE, Kortylewski M, Armstrong B, Froelich J, Hui SK. Biophysical Characterization of the Leukemic Bone Marrow Vasculature Reveals Benefits of Neoadjuvant Low-Dose Radiation Therapy. Int J Radiat Oncol Biol Phys. 2021 Jan 1;109(1):60-72. doi: 10.1016/j.ijrobp.2020.08.037.

2.1 Introduction

In the previous chapter, clinical DCE imaging using either MRI or CT was identified as effective for characterization of some parameters pertaining to the BMV, however it lacked the resolution necessary to observe the underlying single-vessel sized BMV characteristics for direct correlation. To address the need for a single imaging platform capable of observing the BMV functional characteristics and pharmacokinetic alterations from RT, we developed and validated compartmental modeling for quantitative multiphoton microscopy (QMPM) time-lapsed imaging of the BMV in the calvarium of live mice bearing GFP+ Philadelphia chromosome B-cell acute lymphoblastic leukemia (ALL). For QMPM, time-lapsed images of 150 kDa fluorescent dextran leakage from the vascular lumen to the interstitial tissue were fit to the compartmental Toft's model to primarily assess vascular permeability, as well as Ktrans,

and v_{ec}. 150 kDa dextran was chosen as it has a slower leakage rate than smaller sized molecular contrast agents, making it a better molecular contrast agent to identify vascular permeability. Single-vessel functional BMV characteristics including single vessel blood flow, functional vessel surface area, vascular morphology, and vascular density were also measured.

After seeing changes in the BMV with the onset of ALL, we hypothesized that LDRT (2-4Gy) may improve vascular function and morphology, as well as reduce leukemic burden, leading to better uptake of therapeutics and enhanced efficacy when used as a neo-adjuvant therapy prior to therapeutic treatment. The response of the BMV to LDRT in mice bearing ALL was assessed using two treatment types 1) targeted LDRT to half of the calvarium and to the left femur (tLDRT) and 2) TBI. tLDRT was used to only irradiate small volumes of interest ensuring that the systemic blood flow of the cardiovascular system was not affected with treatment. To assess the uptake of therapeutics, cellular uptake of fluorescent agents in regions receiving tLDRT and matching regions outside of the radiation field (abscopal) were compared to assess therapeutic delivery. Assessments were made two days after tLDRT and 20 minutes after intravenous injection of Hoechst 33342 dye (Hoechst, MW: 615.99) or daunorubicin HCL (daunorubicin, MW: 563.98), a chemotherapy used in the treatment of ALL and other hematological malignancies [65]. Both agents are of similar size to many small sized therapeutic agents used for the treatment of hematological malignancies [39]. Finally, the efficacy of nilotinib (MW: 529.52),a similar sized therapeutic agent effective for the treatment of ALL [65], was administered before or after 4Gy TBI to determine whether LDRT-related changes to the malignant bone marrow and BMV may have an impact on treatment outcome in combination therapy.

2.2 Methods

2.2.1 Mice, cell lines, and drug treatments

All procedures for animal experimentation were performed according to City of Hope guidelines and approved by the Institutional Animal Care and Use Committee. C57BL/6J mice (Strain 000664, Jackson Laboratory, Bar Harbor, ME) mice were injected with $1x10^6$ GFP^+ BCR-ABL (p190Kd) expressing B-cell ALLcells [66], suspended in 200 µl of phosphate buffered saline, through the tail vein. To test drug delivery, injection concentrations of 10 mg/kg and 40 mg/kg were used for fluorescent Hoechst 33342 dye (ThermoFisher Scientific Waltham, MA) and fluorescent daunorubicin HCL (Selleck Chemicals LLC Houston, TX), respectively. Mice were imaged or euthanized for tissue processing 20 minutes after tail vein injection of Hoechst dye or daunorubicin. Nilotinib (LC Laboratories Woburn, MA) treatments for survival studies were given at 50 mg/kg using oral gavage.

Eight-to-ten week-old female mice were used in experiments pertaining to endothelial cell analysis, QMPM tile image acquisition, and QMPM vessel morphology analysis. Experiments pertaining to vascular compartmental modeling, dextran well counter fluorescence, total bone marrow cell counts, and Hoechst dye uptake were performed using 7-10 week-old female mice. Intravascular cellular velocity measurements were performed using 7-12 week-old female mice. Daunorubicin QMPM imaging and daunorubicin cellular uptake assays were performed using 10-12 week-old male mice at moderate ALL burden (10-50% femur engraftment). Survival study experiments were performed using 8 week-old female mice. The age range of mice used for individual experiments was minimized to minimize potential age-dependent effects.

Mice for survival studies were monitored for disease progression by peripheral blood sampling. Survival study treatment intervention started seven days after ALL injection when ALL was detectable in the blood of all the mice. Nilotinib treatment was administered using oral gavage at 50 mg/kg suspended in 100 µl of 79% phosphate buffered saline and 21% DMSO. Mice not receiving nilotinib were administered 100 µl of 79% phosphate buffered saline and 21% DMSO on matching days.

2.2.2 Mouse surgery, multiphoton image acquisition, and image display

For QMPM imaging, mice were anesthetized initially with 3% isoflurane at a flow rate of 2 L/min, and then maintained with 1.5% isoflurane at a flow rate of 1.5 liters per minute. A stereotactic apparatus with a bite bar was utilized to keep the mouse stable during surgery. The skin and membrane above the calvarium were removed, and a custom titanium head plate with an inner diameter of 8 mm was fixed to the calvarium using Alpha-Dent Polycarboxylate Cement (Dental Technologies, Lincolnwood, IL). The head plate was then inserted into a custom built heated stage maintained at 37°C allowing for easy viewing of the mouse calvarium [67].

For QMPM imaging, a Prairie Ultima multiphoton microscope (Bruker Corporation Billica, MA) was used. QMPM imaging was primarily performed on the frontal bone region of the calvarium, however 2-3 mice with high leukemic burden were imaged on the superior parietal bone near the coronal suture, as ALL-induced bone degradation made imaging difficult on the frontal bone region. All imaging in this chapter was performed at single-day time points and mice were euthanized after imaging sessions.

Fluorescent excitation was performed using a Chameleon Ultra II tunable Ti:Sapphire laser with 140 femtosecond pulses (Coherent, Santa Clara, CA). An Olympus XLUMPlanFL 20x objective (1.00 NA water objective) was used for image

acquisition of all images. Simultaneous four channel acquisition was performed at 660/40 (far red), 595/50 (red), 525/50 (green), and 460/50 (blue) for visualization of ALL, blood pool agents and second harmonic generation from the collagen in the bone. Data acquisition using the Prairie Ultima microscope was handled by Prairieview 5.3 software and imaging was performed at room temperature.

Vascular blood pool imaging was performed with intravenous injections of 20 µL of Qtracker™ 655 Vascular Label (Invitrogen, Carlsbad, CA) mixed with 80-180 µL of phosphate buffered saline. For time-lapsed imaging and measurements of permeability, K_{trans}, and v_{ec}, mice were intravenously catheterized [61] and injected with 500 µg of 150kDa TRITC dextran (TdB Consultancy, Uppsala Sweden) during image acquisition. Second harmonic generation imaging was used to observe pockets of calvarium marrow within the bone. Second harmonic generation of collagen co-localized with the bone regions surrounding the calvarium marrow compartment.

Fluorescent excitation was performed at 900 nm for GFP+ ALL fluorescence, 150kDa TRITC dextran fluorescence, and Qtracker™ 655 Vascular Label fluorescence (acquired in the green, red, and far red channels respectively). Additional excitation was performed at 840 nm and 960 nm for visualization of both daunorubicin fluorescence (red channel) and GFP^+ ALL fluorescence (green channel), respectively. The second harmonic generation image of the collagen in the bone was performed at 900 nm and 960nm and was detected in the blue channel.

Comparison imaging of 4kDa TRITC dextran was performed with injections of 350 µg suspended in 100 µl of phosphate buffered saline. Time lapsed imaging of 4kDa TRITC dextran was performed at 820 nm.

Color channel windows were adjusted individually in Fiji/ImageJ to improve image display quality. Individual color window adjustments were identical between sets of comparative images. Static image processing and tiling of large image sets were performed using Fiji/ImageJ [68] and CellProfiler (v.2.2.0) [69].

Tiled images were acquired by collecting approximately a 5x4 grid series of overlapping z-stack images. The images were overlapping by 15% with a resolution of 512 by 512 pixels and a z-slice spacing of 15 μm. Tiled images were stitched together using a Fiji/ImageJ grid collection/stitching plug-in [70]. Vascular diameter and the number of vessel branches per area were quantified using Fiji/ImageJ.

Image subtraction and cellular segmentation was performed using Cell Profiler. Image subtraction was used for quantitative GFP+ ALL and static daunorubicin fluorescence analysis as well as for the presentation of all images except time-lapsed daunorubicin and time-lapsed dextran image sets. Image subtraction minimized signal due to background fluorescence, which came from auto-fluorescent cells and collagen and is present in several acquisition channels. For image display and quantification of GFP+ ALL fluorescence in images acquired at 900 nm excitation, auto fluorescence from blue and red channels were multiplied by a scalar and subtracted from the green channel to eliminate signal from both collagen and auto-fluorescent cells respectively. For image display and quantification of daunorubicin and GFP+ ALL fluorescence in single time-point image sets, image subtraction was performed by multiplying the 840 nm excitation blue channel signal by a scalar and subtracting from the 960 nm excitation green channel and 840 nm excitation red channel to identify GFP^+ ALL and daunorubicin fluorescence, respectively. Healthy mice without daunorubicin injections were used to determine image subtraction scalars.

Uncorrected centerline velocities of cells flowing through the BMV network were measured using QMPM and calculated in a similar fashion as in previous works [56, 57]. Vessel cellular velocities were measured after injection of either 150 kDa TRITC dextran or Qtracker™ 655 Vascular Label. Repeated line scans were taken transaxially on the center of blood vessels with frequencies of approximately 0.4 to 3 kHz. The average slope of 3 separate cells was found from time-space images using Fiji/ImageJ to calculate intravascular cellular velocity for a given vessel.

2.2.3 Time-lapsed image acquisition and analysis

Time-lapsed single or z-stack images of dextran leakage into the tissue were taken initially with 6-15 second intervals, increased to approximately 60 seconds after peak tissue concentration had been reached for 150 kDa TRITC dextran. Image drift over time was accounted for by co-registration of time frames in Matlab® (R2018a 9.41.0.81364, MathWorks Natick, MA). To identify blood and tissue compartment regions, time-lapsed images of dextran were cropped to in focus regions. The first frame after dextran had completely perfused the vasculature was selected to perform vascular segmentation in Fiji/Imagej. Images were smoothed with a median filter of four pixels in diameter and an Otsu's thresholding algorithm [71] was applied to segment the vasculature from the tissue and background. If a single Otsu's thresholding algorithm was not adequate to properly identify the vasculature, the first thresholded region was removed from the smoothed image and a second Otsu's thresholding algorithm was applied to identify the remaining vascular regions. After vascular segmentation, an image frame after the dextran tissue concentration had reach maximum (typically the 100^{th} frame) was selected. A Gaussian filter of four pixels in diameter was applied to the image and the vascular regions found earlier were removed from the image. Another Otsu's threshold was applied to segment the regions of tissue uptake from the

background. Since spatial overlap in the dextran fluorescent signal of blood and tissue compartments occurred primarily near boundary pixels in the region of interest (ROI), four- and eight-pixel erosions to the edges of the vascular and tissue ROI were performed respectively. This better isolated dextran fluorescence from tissue and blood compartments. After applying Otsu's thresholding, regions of obvious segmentation mismatch were identified and removed, as such regions would significantly affect quantification accuracy. In general, needed removals were less than 10% of the total segmented volume (Figure 2-3). For daunorubicin compartment identification, blood and tissue compartments were identified in similar fashion as dextran compartments, while the daunorubicin cellular compartment was identified using simple manual selection of representative cellular signal at a late time point after blood and tissue clearance.

Dextran fluorescent intensity in blood and tissue compartments was quantified after spectral unmixing of GFP+ ALL signal bleed through into dextran signal calculated using Equation (2-1).

$$I_D(t) = \frac{R(t) - R_B * \frac{G(t)}{G_B}}{A} \qquad (2\text{-}1)$$

Where R(t) and G(t) are the total red and green channel signal intensity at time t for the ROI. R_B and G_B are the background signal intensities prior to dextran injection for the red and green channels, respectively. A is the area of the ROI being analyzed. The equation for spectral unmixing was used to account for photobleaching of GFP+ ALL cells during time-lapsed imaging. Daunorubicin and 4 kDa TRITC dextran time-lapsed quantification was performed using pre-injection signal background subtraction rather than spectral unmixing, as minimal amounts of ALL signal was present in the daunorubicin channel.

Dextran leakage from tissue and blood ROIs was modeled using Equation 1-3. The blood region was well described by the model using bi-exponential decay (only negative exponential terms were input). Good agreement between data and fit was obtained for all mice. Curve fitting was performed in Matlab® using the lsqnonlin() function. The fitting was performed from a range of starting conditions across the acceptable boundary conditions to ensure the error function was globally minimized.

Vascular permeability was calculated by dividing K_{trans} by vessel surface area per imaging volume. The length and diameter of the lumen for each vessel was measured manually in Fiji/ImageJ, and the respective surface area was calculated by approximating vessels as cylinders. The amount of available calvarium marrow space in each imaging area was accounted for by observation of the second harmonic generation image of the collagen in the bone.

2.2.4 Blood pressure measurements

Pulse rate, systolic blood pressure, and diastolic blood pressure measurements were acquired by tail cuff method on conscious mice using the BP-2000 Blood Pressure Analysis System (Vistech Systems). Thirty successive tail cuff measurements were taken on each day. The first 10 measurements were discarded to allow time for mice to grow accustomed to the tail cuff. Successful measurements from the last 20 measurements were averaged together to obtain results.

2.2.5 Computed tomography and LDRT treatments

Computed tomography (CT) images were administered and acquired with the Precision X-RAD SMART Plus / 225cx small animal image guided irradiation system (Precision X-Ray, North Branford, CT) [72]. CT skull imaging was performed with 40 kVp, 1 mA, and a 100 μm pixel resolution. Square or circular collimators are used to

shape the treatment beam field. CT image processing, contouring, and visualization were performed with Vivoquant (Invicro, Boston, USA) software. Dose calculations were performed by the small animal RT planning system [72], using a Monte Carlo dose engine [73, 74].

Mice were administered tLDRT treatments in a single-fraction of 2-4 Gy soft-tissue-equivalent dose to the left half of the calvarium and left femur. Treatment was performed at 255 kVp and 13 mA. For calvarium treatment, the edge of an anterior 10 mm square beam treated the calvarium with a soft-tissue-equivalent dose of 2 Gy or 4 Gy. This resulted in a dose of approximately 5 Gy or 10 Gy to treated calvarium bone respectively as calculated using the Monte Carlo simulated treatment planning software on the small animal image guided irradiation system. This dose enhancement is largely due to the increased effective atomic number of bone compared to soft tissue. At an effective treatment photon energy of 78.8keV there will be increased dose absorption in bone compared to soft tissue due to photo-electric based dose absorption. The beam was placed 200 μm to the mouse's right side from the sagittal suture and completely covered the parietal and frontal bones on the mouse's left side. The left femur was treated with 10 mm square anterior to posterior and posterior to anterior beams. Dose was normalized to 2 Gy or 4 Gy 2 mm below the surface of the skull for parietal beam and 2 Gy or 4 Gy within the marrow for the femur beams.

tLDRT treatments were used to assess drug delivery and disease burden by comparing treated regions (left femur and left half of the calvarium) and abscopal regions (right femur and right half of the calvarium). TBI single-fraction treatments of 2-4 Gy were administered at matching soft-tissue doses to tLDRT treatments, enabling comparisons of the irradiated BMV in the left half of the calvarium for tLDRT treatments

(local vascular treatment) and TBI treatments (systemic cardiovascular treatment). QMPM imaging and tissue harvests were performed 40-48 hours post-irradiation.

2.2.6 Flow cytometry

Endothelial cell analysis was performed according to Kumar et al [75]. The tibias and femurs from mice were crushed and incubated with collagenase (3 mg/ml, Sigma Aldrich, St Louis, MO) for 45 min at 37°C to liberate the leukemic and bone marrow microenvironment cells from the bone surface. Cells were incubated with ACK lysis buffer (Gibco) for 5-10 minutes and washed with phosphate buffered saline. The cells were filtered through a 40 μm filter and centrifuged at 300xg for 5 min with phosphate buffered saline (0.1%BSA) solution at 4°C. The cells were then blocked with CD16/32 blocking antibody, followed by staining with CD45 (PE/Cy5, clone 30-F11), Ter119 (PE/Cy5, Ter119), CD31 (PE/Cy7, clone 390) (Bio Legend, San Diego), and endomucin (A660, eBioV.7C7 ebioscience) antibodies and with AmCyan viability dye for 30-45 min at 4°C in dark. After staining, cells were washed in phosphate buffered saline (0.1% BSA). Stained cells were analyzed on FACSARIAIII (BD bioscience, Franklin Lanes, NJ) and analyzed in live (AmCyan-), non-leukemic (GFP-) CD45-Ter119-CD31+ fraction. Flow cytometry analysis was performed using FlowJo 10.5.3 software (FlowJo, Ashland, OR).

For measurements of Hoechst dye uptake, tLDRT-treated and abscopal femur and calvarium samples were crushed in phosphate buffered saline (0.1%BSA) solution. Cells suspensions were filtered through a 40 μm filter and centrifuged at 300xg for 5 min at 4°C, then incubated with ACK lysis buffer for 5-10 minutes to remove red blood cells. The cells were analyzed for Hoechst uptake in both the total cell and GFP+ ALL cell populations using the BD Fortessa (BD bioscience, Franklin Lanes, NJ) on the same day.

For measurements of daunorubicin uptake, tLDRT-treated and abscopal femur samples were crushed in phosphate buffered saline (0.1%BSA) solution. Cells suspensions were filtered through a 40 μm filter and centrifuged at 300xg for 5 min at 4°C, then incubated with ACK lysis buffer for 5-10 minutes to remove red blood cells. The cells were stained with AmCyan viability dye (1 μg/ml) for 15 min and washed with phosphate buffered saline. Cells were analyzed on AmCyan- (live) GFP+ (leukemic) cell population using BD FACSARIAIII sorter 2-3 hours post-harvest and were kept on ice throughout the staining process.

To monitor GFP+ ALL progression, 5-10 μL of peripheral blood was taken from the tail vein of mice. Samples were incubated with ACK lysis buffer for 5-10 minutes to remove red blood cells, then washed with phosphate buffered saline and read using the BD Fortessa within 24 hours. Measurements of GFP+ ALL femur engraftment were analyzed in similar fashion after femur samples were crushed in phosphate buffered saline (0.1%BSA) solution, filtered through a 40 μm filter, and centrifuged at 300xg for 5 min at 4°C.

2.2.7 Dextran well plate readings

Well plate fluorescence readings of TRITC dextran concentration were read from supernatants taken from crushed single-femur cell suspensions after removal of cells with centrifugation. Dextran femur supernatant fluorescence was measured in imaged mice that were euthanized 50 minutes after 150kDa TRITC dextran injection. Femurs were crushed in 7 ml of phosphate buffered saline (0.1%BSA) solution and centrifuged at 300xg for 5 minutes at 4°C. A total of 200 μl of supernatant was removed and read using a FilterMax F5 Multi-Mode Microplate Reader (Molecular Devices San Jose, CA). Well plate readings were linear over the read range (data not shown).

2.2.8 Statistical analysis

All statistical testing in this chapter was performed using Prism (V.7.01, GraphPad). Unless otherwise noted, significance testing between groups was performed using Welch's two-sided t test with a P value<0.05 considered significant. Significance testing for survival data was calculated using the log-rank Mantel-Cox test. For linear correlation testing, R squared coefficient of determination tests were used. All distribution error bars are displayed as the mean plus or minus one standard error of the mean.

2.3 Results

2.3.1 Bone marrow microenvironment remodeling and leukemia localization during ALL growth

Large QMPM three-dimensional tiled images of separate mice showed steady progression of ALL disease burden in the calvarium from 2 to 14 days post ALL injection. ALL was predominately homogenously distributed throughout calvarium marrow space. However, occasional regions of the calvarium did contain heterogeneous pockets of ALL (Figure 2-1). Degradation of the calvarium was present in mice at high ALL burden resulting in a loss of bone-collagen second harmonic signal near the sagittal and coronal calvarium sutures. Additionally, X-ray CT scans revealed reduced Hounsfield Units on the frontal lobe of mice bearing ALL as compared to healthy control mice suggesting a loss of bone mineral density with the onset of ALL (Figure 2-2).

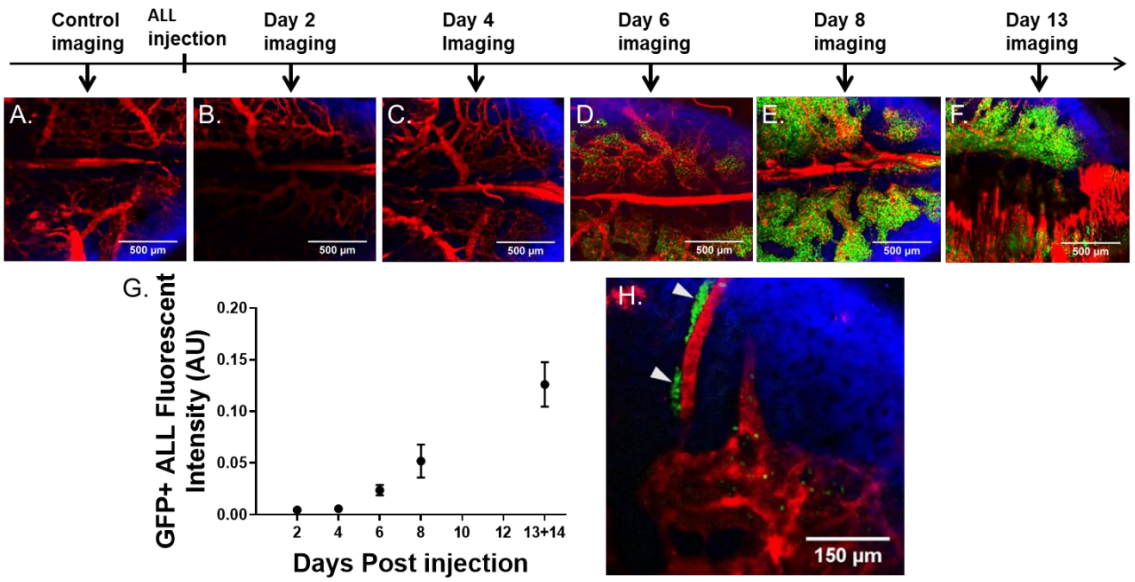

Figure 2-1: Tiled multiphoton microscopy images of the calvarium in (A) a healthy control mouse and mice 2, 4, 6, 8, and 13 days post ALL injection (B-F) are shown. Red is Qtracker™ 655 labeled vascular blood pool fluorescence, green is GFP ALL fluorescence, and blue is second harmonic generation from the collagen in the bone. (G) GFP+ ALL fluorescent intensity in images from mouse calvarium their respective days post injection (one time point per mouse, n=4, 4, 4, 3, and 3 mice for each time point, respectively). (H) A region of heterogeneous ALL distribution. Pockets of heterogeneous ALL are marked with white triangles.

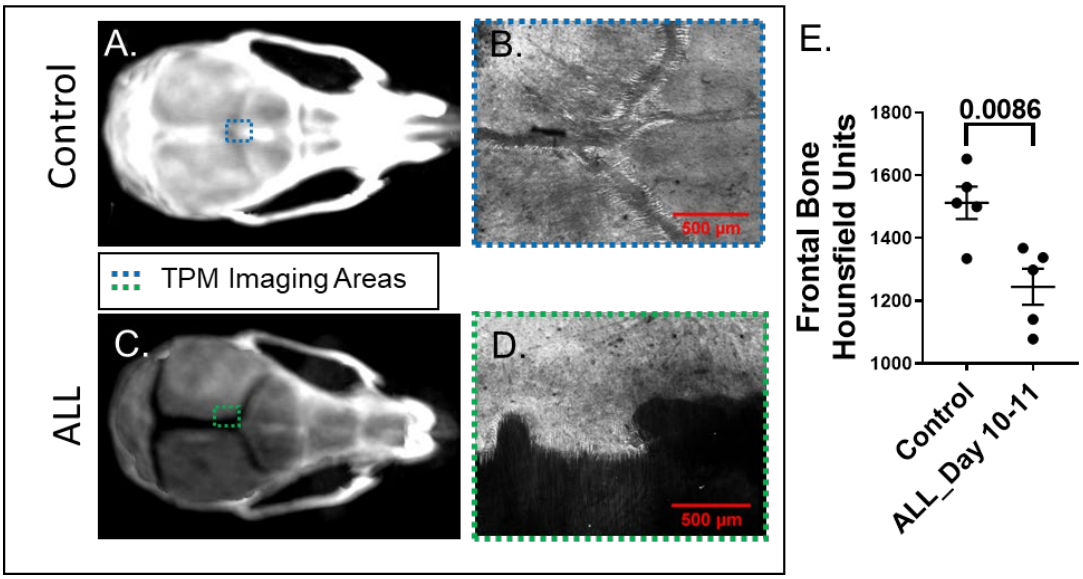

Figure 2-2: (A, C) Three-dimensional intensity projection images of CT scans from healthy control mice and mice bearing ALL 12 days post ALL injection. Colored dotted lines indicate relative regions of multiphoton microscopy imaging performed in A and C.

(B, D) Multiphoton microscopy images of bone-collagen second harmonic generation are shown from a healthy control mouse and a mouse bearing ALL 14 days post ALL injection. (E) CT Hounsfield units from contoured frontal bones of healthy control mice and mice bearing ALL 10-11 days post ALL injection (n=5 mice per group).

2.3.2 Changes in K_{trans} and increased BMV permeability in mice bearing ALL

For all time-lapsed QMPM images, 150kDa dextran had reached the BMV between 6 and 12 seconds after injection. The fluorescent time-lapsed intensity of 150kDa dextran in the vascular ROI was well described by bi-exponential decay suggesting semi-consistent BMV blood flow. Dextran uptake into the extravascular calvarium bone marrow tissue started immediately after dextran flow into the BMV. The time-lapsed fluorescent intensity of dextran in blood and tissue compartments showed good agreement with the Toft's compartmental model which was used for analysis (Figure 2-3).

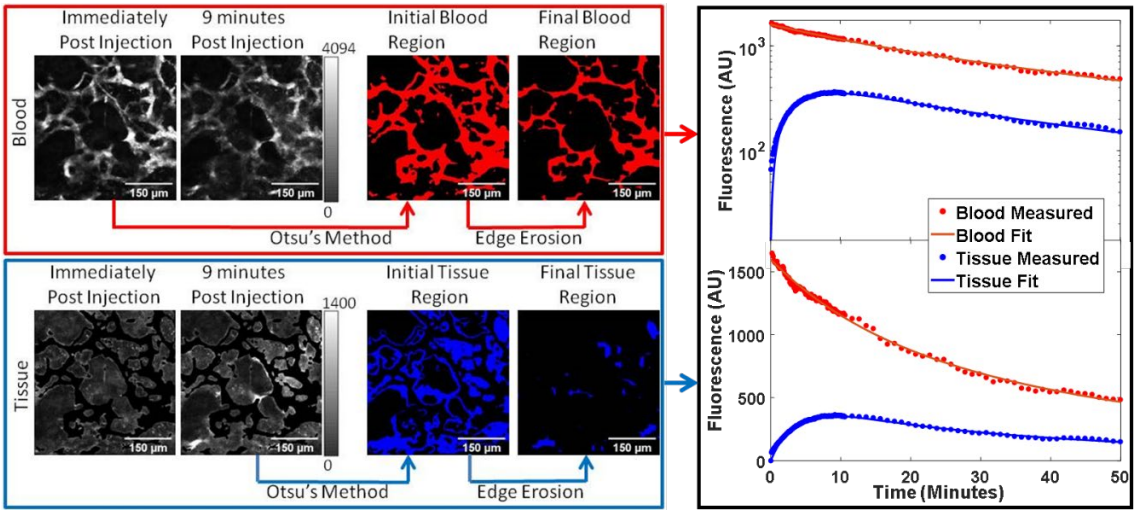

Figure 2-3: The segmentation schemas for the blood compartment and the tissue compartment for 150kDa TRITC dextran compartmental analysis are shown. Briefly, the time-lapsed images are co-registered, and Otsu's method is used on images at an early time point to segment the vascular regions. To segment the tissue region, a later time point image is selected after dextran leakage into the tissue. The previously segmented vascular region is removed, and Otsu's method is used to segment the tissue regions. Edge erosion is applied to the segmented regions to better isolate dextran fluorescent

signal in the blood and tissue compartments. Scale bars indicate the imaging window range for displayed early and late blood and tissue image sets. The corresponding blood and tissue compartment time-lapsed dextran fluorescent intensity from the segmented regions is displayed in linear and log scale with corresponding fitting function curves.

We additionally performed QMPM imaging with two smaller sized molecular contrast agents, 4kDa TRITC dextran and daunorubicin chemotherapy. The kinetics of these smaller contrast agents were compared to the kinetics of 150kDa sized dextran to ensure that QMPM-based, time-lapsed, imaging can be used for fluorescent agents of varying sizes and pharmacokinetic uptake patterns. Daunorubicin imaging was performed in a mouse bearing ALL. A clear distinction between vascular, tissue, and cellular compartments could be seen in daunorubicin images. A faster blood clearance and faster peak tissue uptake of daunorubicin is observed compared to dextran (because of its smaller molecular weight. Figure 2-4). Additionally, 4kDa dextran had a much faster uptake and clearance than 150kDa dextran in healthy control mice (Figure 2-5). After ensuring that QMPM could identify changes in the kinetics of several different molecular contrast agents, we selected 150kDa dextran for use to measure vascular permeability due to its slower leakage rate.

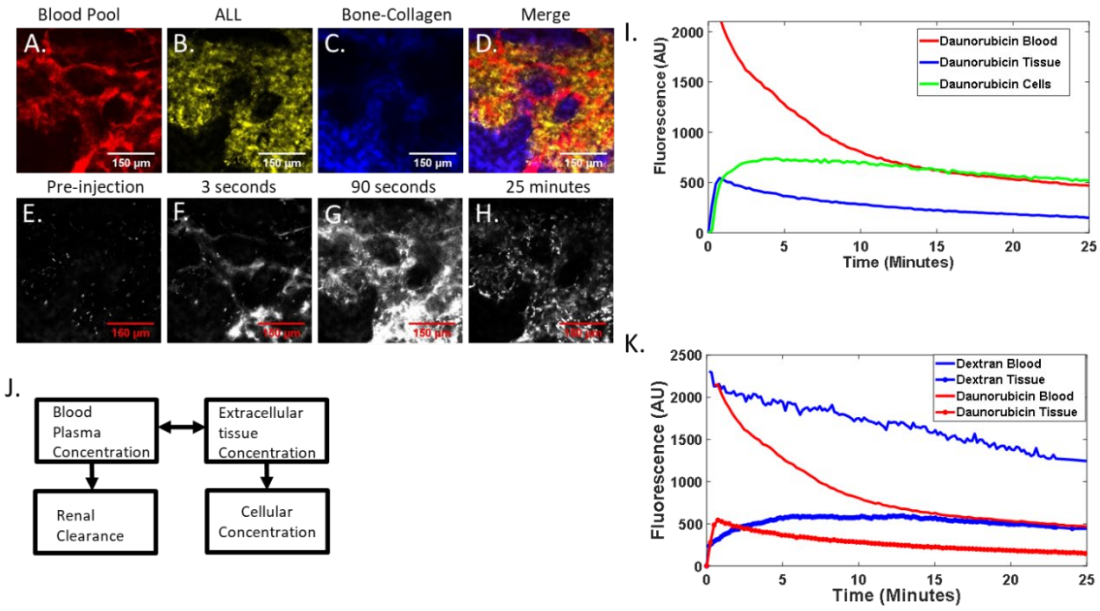

Figure 2-4: QMPM images of ALL burdened mouse calvarium showing (A) Qtracker™ 655 vascular blood pool fluorescence, (B) GFP+ ALL fluorescence, (C) the second harmonic generation image of the collagen in the bone, and (D) a merged image are shown for a daunorubicin-injected mouse. Time-lapsed imaging of daunorubicin fluorescence (E) before, (F) three seconds post, (G) 90 seconds post, and (H) 25 minutes post daunorubicin injection are shown. A clear distinction between blood, tissue, and cellular compartments can be seen. (I) Plots of fluorescent intensity versus time for contoured blood, tissue, and cellular compartments are shown. (J) A representative image of a three-tissue compartment model applicable to daunorubicin is shown. (K) A comparison of fluorescent intensities of blood and tissue compartments for daunorubicin and 150kDa TRITC dextran in separate mice bearing ALL is shown.

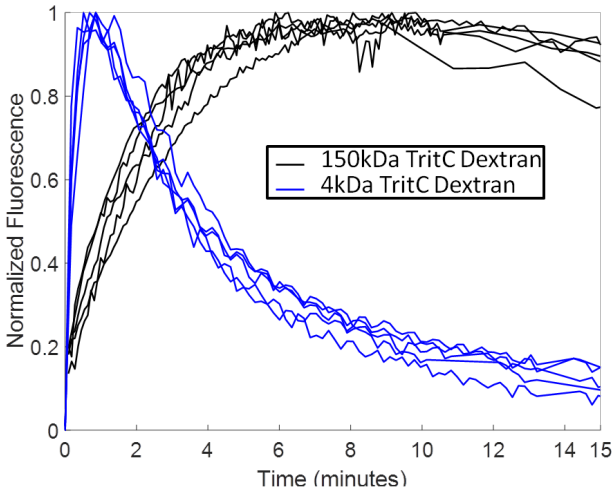

Figure 2-5: Normalized fluorescent intensity of the extravascular tissue compartment from time-lapsed images taken of the calvarium in healthy untreated mice using 150kDa TRITC dextran (black) and 4kDa TRITC dextran (blue) (n=5 mice each group). Peak

uptake of 150kDa dextran occurs at approximately 6-10 minutes compared to approximately one minute with 4kDa dextran.

Validation of the compartmental model was performed by perturbing the system using tLDRT to the left femur and left half of the calvarium in healthy mice, as radiation has been shown to both increase v_{ec} (by decreasing total tissue cell number) and damage vasculature, causing increased leakage [51, 76, 77]. A corresponding reduction in total cell number in irradiated femur and calvarium bone marrow regions was found compared to abscopal regions. Significantly higher dextran fluorescence in crushed femur supernatants was found for tLDRT-treated femurs compared to abscopal femurs ($P=0.0003$), suggesting LDRT significantly increases total dextran concentration in the bone marrow tissue. A negative correlation between femoral bone marrow total cell count and dextran fluorescence of crushed femur supernatants was found, confirming that extracellular space and the total dextran uptake in the bone marrow are influenced by total cellular density ($R^2=0.7905$, $P<0.0001$, Figure 2-6).

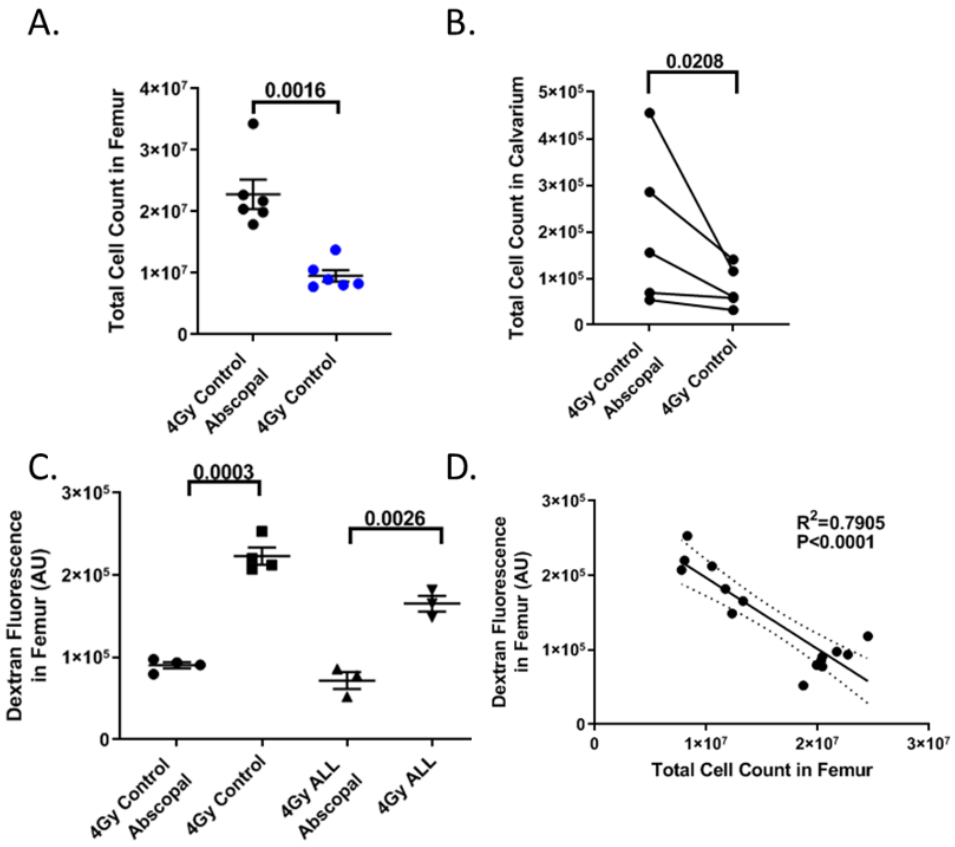

Figure 2-6: (A) Total number of bone marrow cells in crushed 4 Gy tLDRT-treated and abscopal femur samples from non-leukemic mice (n=7, 6 mice per group respectively). (B) Total number of calvarium bone marrow cells in crushed tLDRT-treated and abscopal calvarium regions of non-leukemic mice with a two-sided paired t-test calculation (n=5 mice). (C) Dextran fluorescence of crushed femur supernatants from non-leukemic abscopal, non-leukemic 4Gy tLDRT-treated, ALL abscopal, and ALL 4Gy tLDRT-treated single femurs (n=4, 3 non-leukemic mice and mice bearing ALL respectively). (D) The number of total bone marrow cells in crushed single femur samples versus dextran fluorescence of crushed femur supernatants is shown (n=15 single femurs). Abscopal and treated femurs taken from LDRT-treated non-leukemic mice and LDRT-treated mice bearing ALL are shown. The corresponding R-squared value and best fit line are also displayed.

Four-Gy tLDRT significantly increased v_{ec} and K_{trans} in tLDRT-treated calvarium regions compared to regions in untreated healthy mice (P=0.0003 and P=0.0320, respectively). After validation, time-lapsed QMPM images in the calvarium of mice bearing ALL found an increase in v_{ec} compared to healthy control mice (P=0.0172). No significant difference in femoral bone marrow total cell number was observed

(P=0.1744), indicating that the change in v_{ec} may be due to other additional factors, such as bone degradation or high interstitial fluid pressure. At low-to-moderate ALL engraftment, K_{trans} was significantly higher than healthy control mice (P=0.0488). Functional BMV surface area per volume in time-lapsed QMPM images decreased with ALL burden. A significant increase in vascular permeability was observed in mice with low-to-moderate ALL engraftment compared to healthy control mice (P=0.0085, Figure 2-7 Figure 2-8).

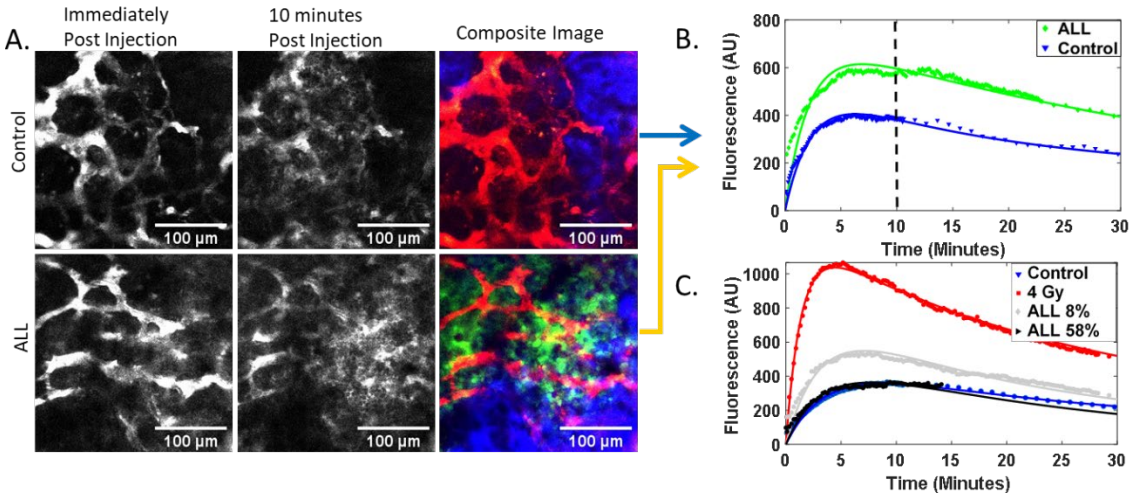

Figure 2-7: (A) TRITC dextran fluorescence is shown for a healthy mouse and a mouse bearing ALL immediately and ten minutes after dextran injection is shown in gray. Merged images verifying the local presence of ALL are shown. Green is GFP+ ALL fluorescence, red is TRITC dextran fluorescence, and blue is bone-collagen second harmonic generation. (B) Time-lapsed dextran fluorescent intensity from segmented tissue compartment regions is plotted with corresponding fitted tissue compartment curves for the control mouse and mouse bearing ALL shown in A. The vertical striped line indicates the 10 minutes post injection time point depicted in the images. (C) A plot of time-lapsed dextran fluorescent intensities from the segmented tissue compartments of a healthy control mouse, a non-leukemic 4 Gy tLDRT-treated mouse, a mouse with 8% ALL femoral bone marrow engraftment, and a mouse with 58% ALL femoral bone marrow engraftment. The fitted tissue compartment curves for each mouse are also plotted.

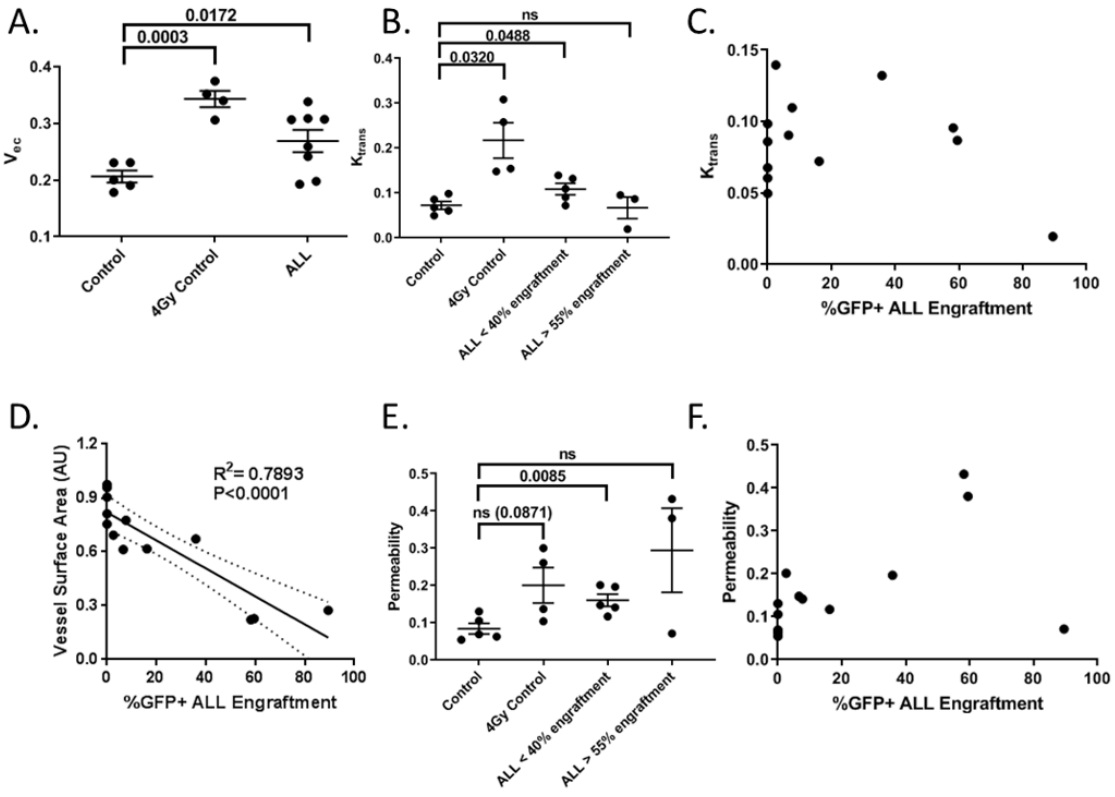

Figure 2-8: (A) Values for v_{ec} are shown for healthy control mice, non-leukemic LDRT-treated mice, and mice bearing ALL (n=5, 4, 8 mice per group respectively). (B, E) Values for K_{trans} and vascular permeability are shown for healthy control mice, non-leukemic tLDRT-treated mice, mice with less than 40% ALL femoral bone marrow engraftment, and mice with more than 55% ALL femoral bone marrow engraftment. (n=5, 4, 5, 3 mice respectively). (D) Vessel surface area versus GFP+ ALL femur bone marrow engraftment with the corresponding R-squared value and best fit line are plotted for untreated mice analyzed with QMPM compartmental modeling (n=13 mice). (C, F) Plots of ALL femur bone marrow engraftment compared to K_{trans} and permeability for healthy control mice and mice bearing ALL is shown (n=13 mice).

2.3.3 BMV remodeling results in angiogenesis, poor blood flow, and loss of functional vessels with ALL

Crushed femur and tibia samples were analyzed by flow cytometry to observe endothelial cell changes with ALL progression. An increase in the CD45/TER119-CD31+ endothelial cell fraction in total live cells was observed in mice bearing ALL compared to control mice (P=0.0032). No significant differences in femoral bone marrow total cell number between healthy mice and mice bearing ALL were observed,

suggesting an overall increase in the total number of endothelial cells present in the bone marrow of mice bearing ALL (P=0.1744). Additionally, a significant reduction in the high endomucin expressing endothelial cell fraction in total endothelial cells was found for mice bearing ALL compared to control mice (P<0.0001, Figure 2-9). High endomucin expressing endothelial cells have previously been reported to co-localize with osteoblast progenitors in the growth plate regions of the femoral bone and are responsible for hematopoietic stem cell (HSC) maintenance by secreting HSC-supporting cytokines [78]. These data suggest that ALL transforms the endothelial subset away from a hematopoietic supporting niche in support of ALL.

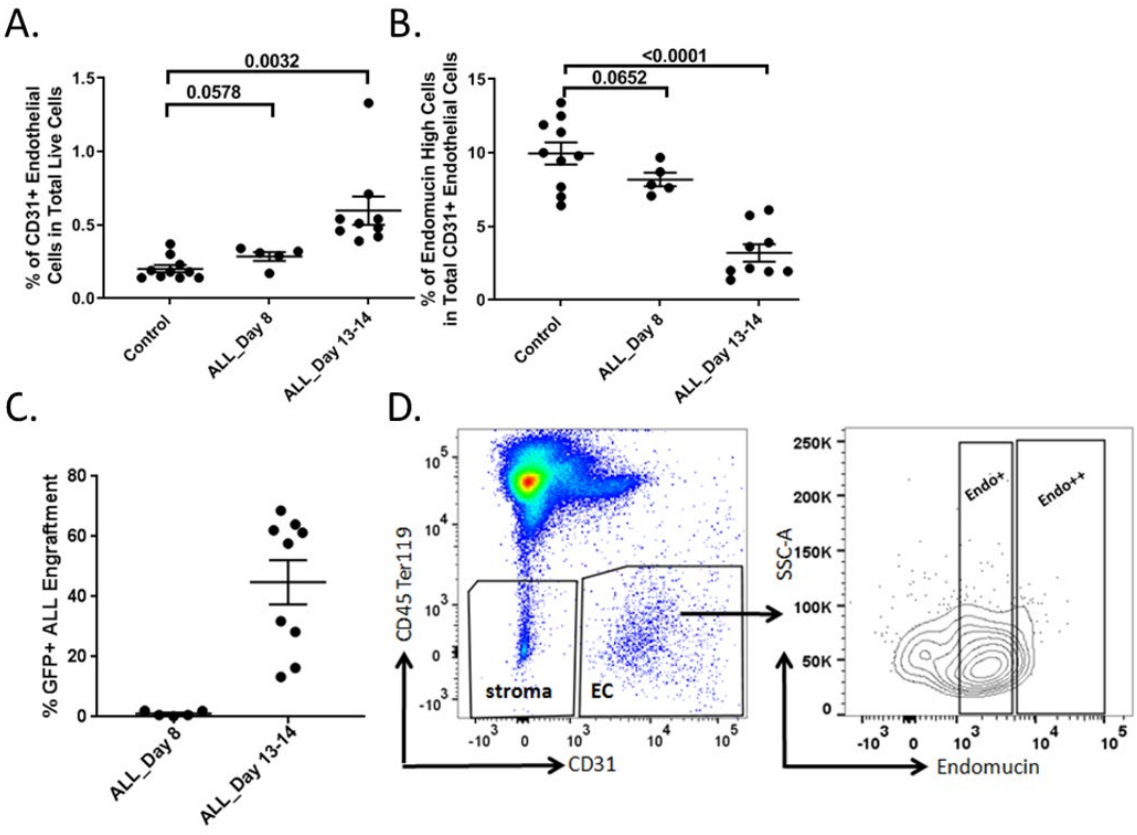

Figure 2-9: (A) Flow cytometry analysis of the percentage of CD31+ endothelial cells in total live cells for control, 8 days, and 13-14 days post ALL injection are shown (n=10,5,9 mice per group respectively). (B) The fraction of high endomucin-expressing endothelial cells in total endothelial cells for control, 8 days post ALL injection, and 13-14 days post ALL injection mice is shown (n=10,5,9 mice per group respectively). (C) Corresponding GFP+ ALL engraftment for mice analyzed for endothelial cell flow cytometry analysis in

subfigures A & B (n=5, 9 mice per group respectively).(D) The flow cytometry gating scheme for CD45Ter119- CD31+ endothelial cell population and high endomucin subpopulation is shown.

Endothelial expansion was accompanied by large changes in BMV function and morphology. QMPM measurements of calvarium mean vessel density were higher in mice bearing ALL compared to those in healthy control mice (319 mm^{-2}, P= 0.0017). QMPM revealed a significant reduction (8.93 μm) in the average inner diameter of vessels in the calvarium in mice bearing ALL compared to healthy control mice (P<0.0001, Figure 2-10).

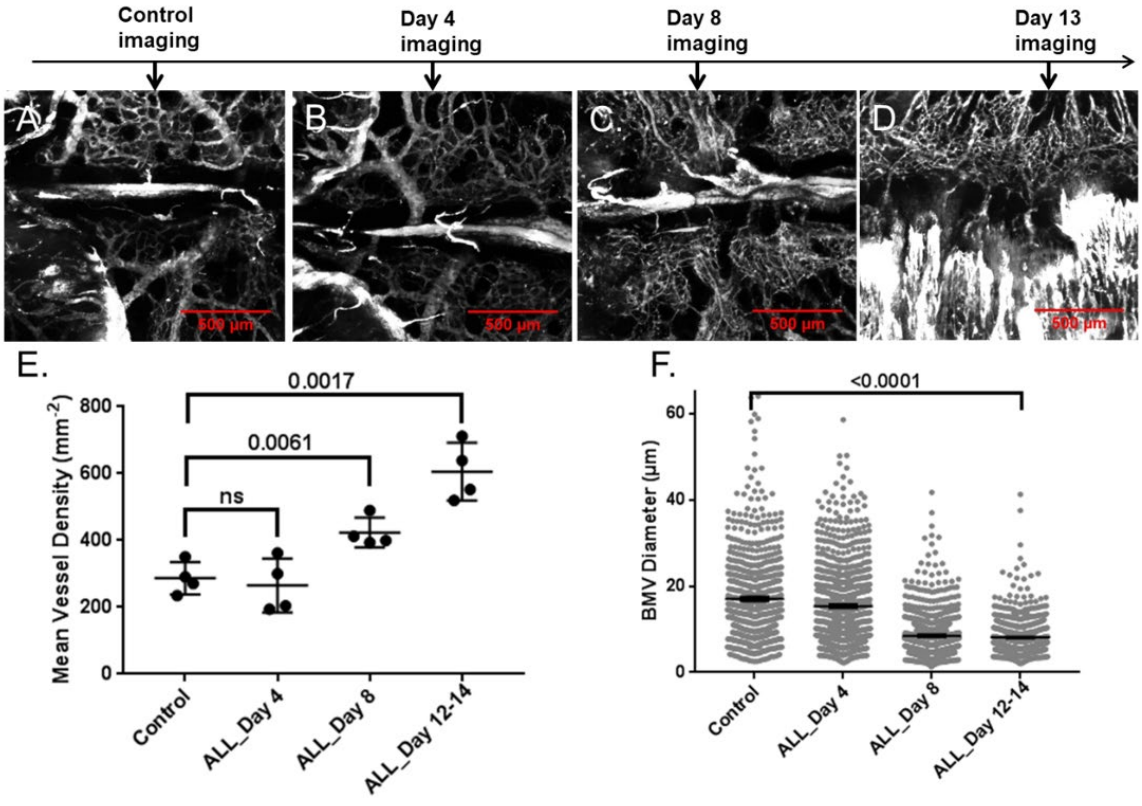

Figure 2-10: Representative tiled maximum intensity projection images of Qtracker™ 655 vascular blood pool fluorescence for (A) control mice and mice (B) 4 days, (C) 8 days, and (D) 13 days post ALL injection are shown. Measurements of (E) mean vessel density and (F) vessel diameter from images of healthy control mice and BCR-ABL mice 4, 8, and 12-14 days post ALL injection are shown (n=4 mice per group).

Average velocities of cells flowing through the BMV of mice bearing ALL (1.34±0.11 mm/s) were reduced compared to healthy control mice (3.70 ± 0.484 mm/s, $P<0.0001$). Control mice typically had small inner diameter vessels with rapid blood flow connected to slow flowing vessels with a large inner diameter. Alternatively, mice with moderate-to-high ALL burden displayed a more homogenous population of vessels in terms of both blood flow velocity and vessel diameter, suggesting that typical cellular extravasation, oxygen delivery, and drug delivery may be altered in mice bearing ALL (Figure 2-11).

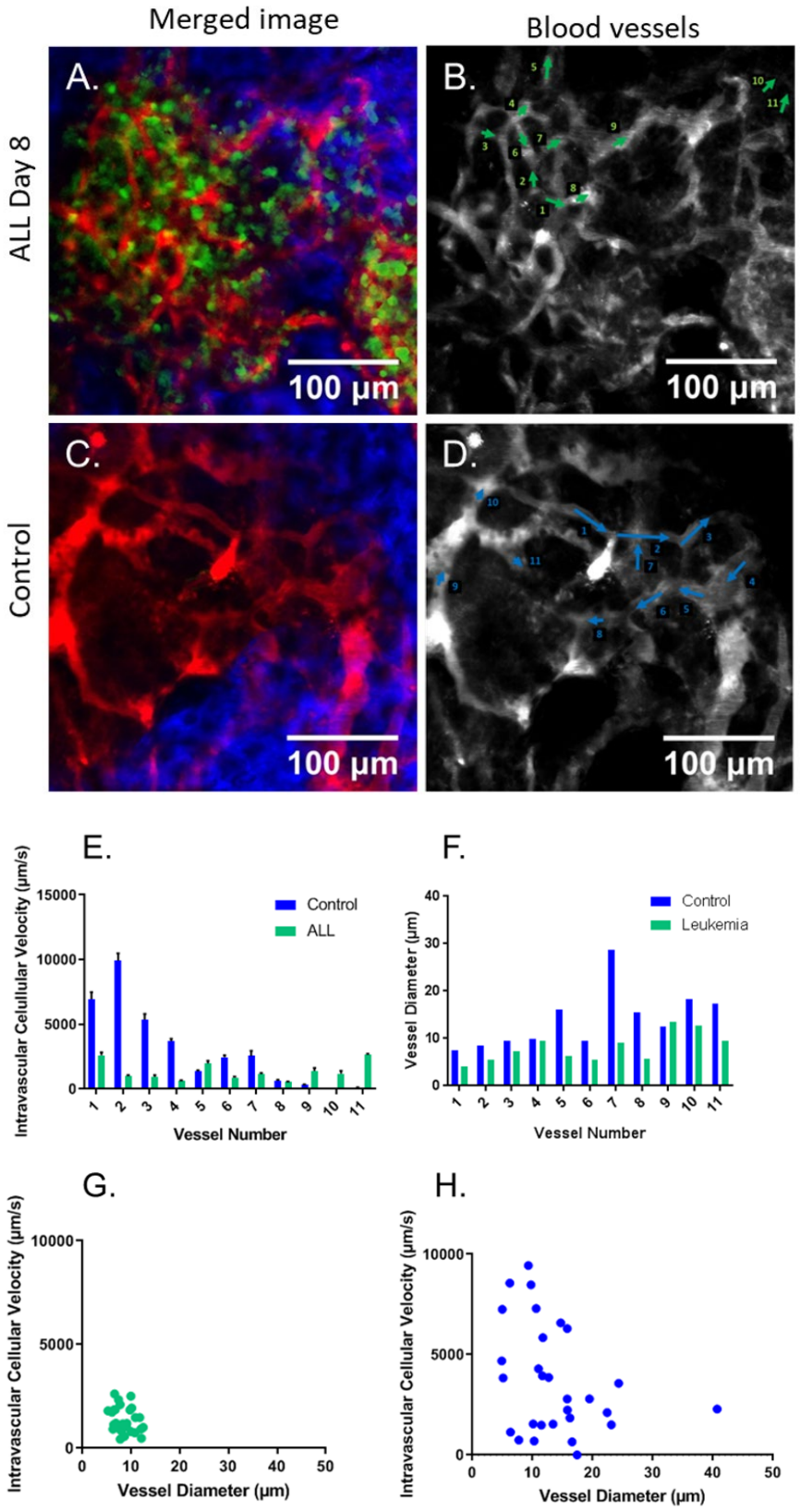
Merged image
Blood vessels
ALL Day 8
Control
A.
B.
C.
D.
100 µm
E.
F.
Intravascular Celullular Velocity (µm/s)
Control
ALL
Vessel Number
Vessel Diameter (µm)
Control
Leukemia
Vessel Number
G.
H.
Intravascular Cellular Velocity (µm/s)
Vessel Diameter (µm)
Intravascular Cellular Velocity (µm/s)
Vessel Diameter (µm)

Figure 2-11: Merged color images of the calvarium of (A) mice bearing ALL and (C) control mice. Green is GFP+ ALL fluorescence, red is Qtracker™ 655 blood pool fluorescence, and blue is the second harmonic generation of collagen in the bone. Vascular blood pool images with corresponding blood velocity mapping of upstream to downstream vessels labeled 1-11 are displayed for (B) ALL burdened vessels and (D) healthy vessels. Mice bearing ALL were imaged 8 days post ALL injection. (E) Intravascular cellular velocity and (F) vessel diameter measurements from labeled vessels in B and D show the loss of upstream, fast-flow, small-diameter vessels and downstream, large-diameter, slow-flow vessels in mice bearing ALL. Plots of cell velocity versus diameter for (G) ALL burdened vessels eight days post ALL injection and (H) healthy control vessels (n=3 mice per group, 10 vessel measurements per mouse).

QMPM imaging revealed regions of semi-collapsed vessels in the calvarium of mice as early as day 8 post ALL injection. Accumulation of non-moving cells in blood vessels was observed near regions of partial BMV collapse. The BMV opened and closed intermittently in some mice bearing ALL during time-lapsed imaging, but not in control mice (Figure 2-12). Measurements of systolic and diastolic pressure were taken to better understand the mechanics behind BMV closing. Reductions in systolic (56.2 mm Hg) and diastolic pressure (31.0 mm Hg) were measured with the onset of ALL ($P=0.0002$ and 0.0375, respectively, Figure 2-13), suggesting that reduced systemic blood pressure may contribute to BMV collapse.

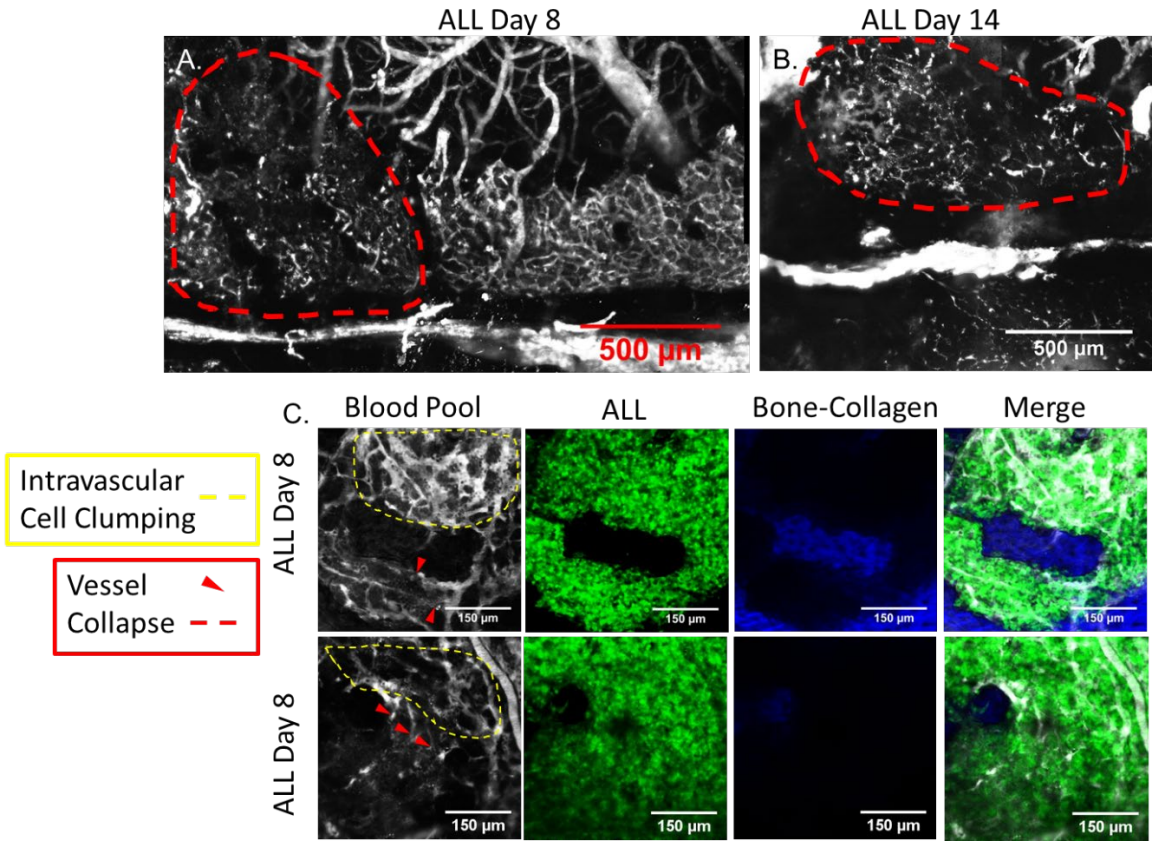

Figure 2-12: Tiled QMPM images of Qtracker™ 655 vascular blood pool fluorescence in the calvarium of ALL-transplanted mice at (A) 8 days and (B) 14 days post ALL injection. Red dashed lines indicate regions of vascular collapse. (C) Merged composite images of Qtracker™ 655 blood pool fluorescence (gray), GFP+ ALL fluorescence (green), and the second harmonic generation image of the collagen in the bone (blue) for ALL injected mice 8 days post injection. Red triangles and red dashed lines indicate specific vessel collapse and regions of vascular collapse, respectively. Yellow dashed lines indicate regions of accumulated non-moving cells in the BMV.

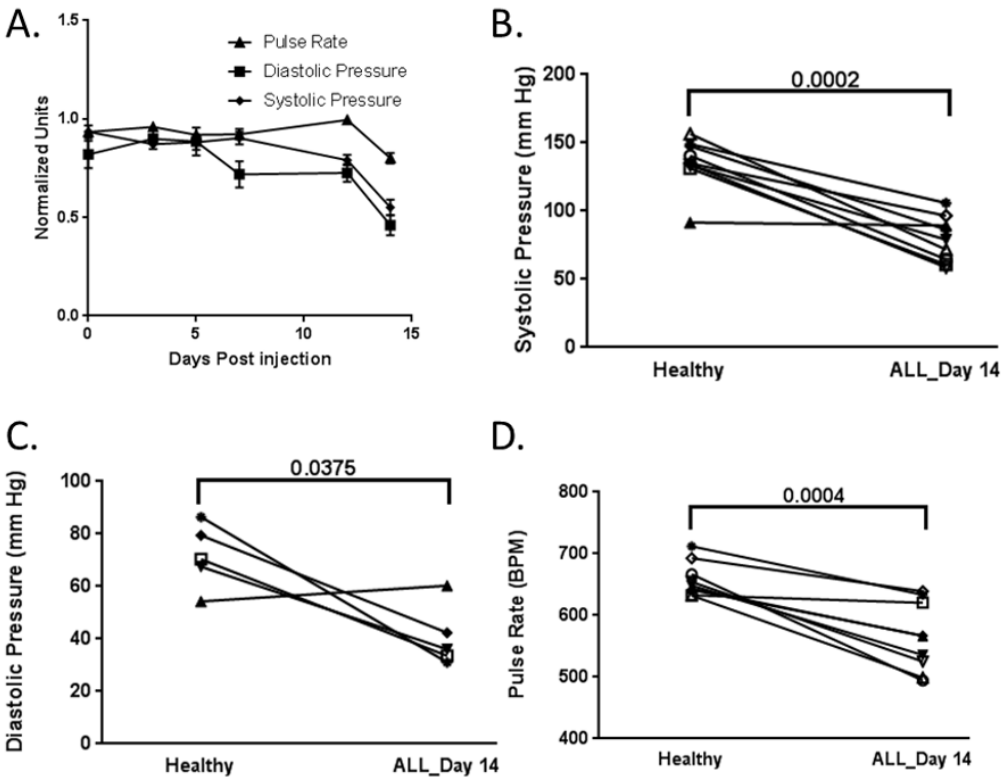

Figure 2-13: (A) A normalized plot of mouse pulse rate, diastolic blood pressure, and systolic blood pressure before ALL injection and 3, 5, 7, 12, and 14 days following ALL injection. (B-D) Plots of systolic blood pressure, diastolic blood pressure, and pulse rate in mice before and 14 days after receiving ALL injection with two-sided paired t-test significance values.

2.3.4 LDRT improves blood flow, improves chemotherapy delivery, and increases survival in combination therapy

Next the effects of LDRT on the BMV in mice bearing ALL were tested with the hypothesis that LDRT would be beneficial to 1) improve the function and morphology of the BMV, 2) enhance therapeutic uptake, and 3) increase treatment efficacy when used prior to the administration of therapeutics. tLDRT treatments altered the morphology and function of the BMV in mice bearing ALL two days post treatment. Two-Gy tLDRT treated mice bearing ALL had increased average vascular diameter (13.4 μm) and

increases in the average velocity of cells flowing through the BMV network (2.41 mm/s) compared to untreated mice bearing ALL (P< 0.0001 and 0.0001, respectively). These treatments increased average cellular vascular velocity to similar levels as in healthy control mice (P=0.9497). Similar BMV changes were observed with 2 Gy TBI treatments, suggesting that systemic LDRT to the cardiovascular system does not largely impact blood flow, and that functional vascular changes may be beneficial for a variety of systemic or targeted RT treatments (Figure 2-14).

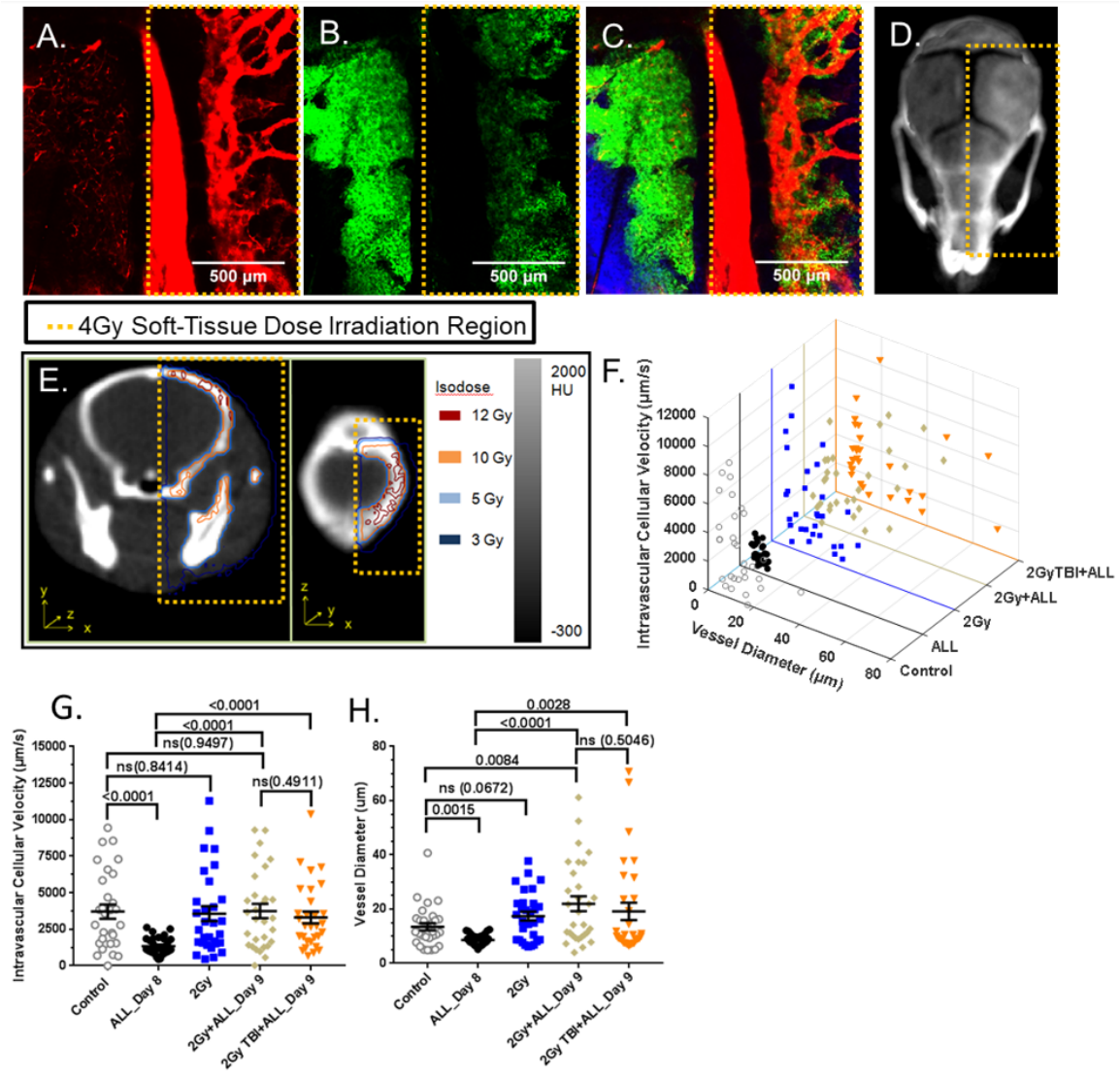

Figure 2-14: Tiled images taken two days post 4 Gy tLDRT and 13 days post ALL injection, showing irradiated and abscopal regions of the mouse calvarium with (A)

Qtracker™ 655 vascular blood pool fluorescence in red, (B) GFP+ ALL fluorescence in green, and (C) a merged image with bone-collagen second harmonic generation in blue. (D) A representative three-dimensional intensity projection CT image depicting the tLDRT treatment region. (E) CT images with isodose lines showing the corresponding 4Gy tLDRT irradiated calvarium region shown in A-C. (F-H) Intravascular cellular velocity and vessel diameter plots for individual blood vessels are plotted for healthy control mice, non-treated mice bearing ALL, 2 Gy tLDRT-treated healthy mice, 2 Gy tLDRT-treated mice bearing ALL, and 2 Gy TBI-treated mice bearing ALL (n=3 mice per group). Ten individual vessel measurements were taken from each mouse. Untreated and irradiated mice bearing ALL were imaged 8 days and 9 days post-ALL injection, respectively.

After seeing changes in the BMV with tLDRT and TBI, the therapeutic delivery of Hoechst and daunorubicin to the bone marrow was measured by cellular uptake using flow cytometry. Mice were administered intravenous injections of Hoechst or daunorubicin two days after 2Gy and 4Gy tLDRT and 20 minutes before euthanizing mice for tissue harvest. To observe changes in drug uptake, tLDRT-treated calvarium and femur regions were compared to matching abscopal regions in mice bearing ALL. The percentage of total cells stained positive for Hoechst in abscopal calvarium regions had a negative correlation with ALL engraftment, whereas no significant changes in overall total cell number were seen in the femoral bone marrow of mice bearing ALL compared to healthy mice (P=0.1744). This suggests that cellular Hoechst uptake is inhibited by the onset of ALL but not reduced due to a change in total cell number. Non-leukemic tLDRT-treated mice showed high percentages of total calvarium marrow cells labeled positive for Hoechst in both 2 Gy tLDRT-treated (94.7 ± 3.9%) and abscopal calvarium regions (90.5 ± 1.0%, Figure 2-15).

In 2Gy tLDRT-treated regions compared to abscopal regions, increases in the percentage of ALL cells labeled positive for Hoechst (88.3±3.6% and 63.5±3.0% respectively, P=0.0067) and daunorubicin (90.8±2.3% and 72.3±1.8% respectively, P=0.0036) were found (Table 2-1). Similar trends were observed with 4 Gy tLDRT treatments. QMPM-based image segmentation of ALL cells revealed higher

daunorubicin fluorescence for cells in 2 Gy tLDRT-treated calvarium compared to abscopal calvarium (P=0.0362, Figure 2-16). Results demonstrate enhanced cellular uptake of small molecular weight therapeutics after neo-adjuvant LDRT.

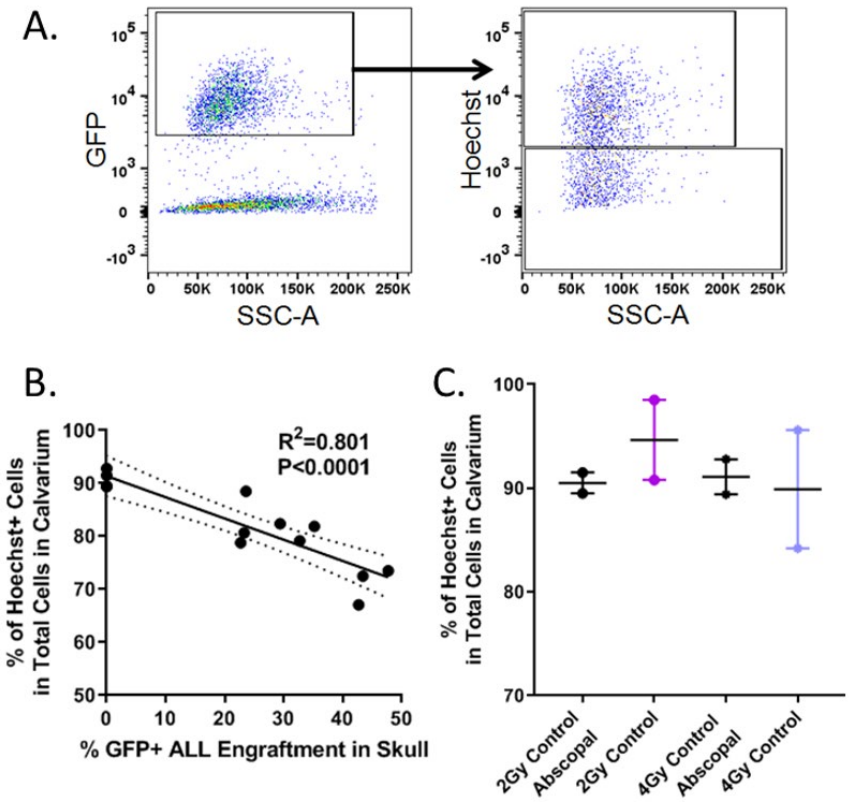

Figure 2-15: (A) A representative gating scheme for Hoechst+ GFP+ and Hoechst- GFP+ ALL populations. (B) Flow cytometry analysis of the percentage of total cells stained positive for Hoechst versus the percentage of cells in the abscopal calvarium that are GFP+ ALL (n=13 mice). The corresponding R-squared value and non-zero significance value are shown. (C) A plot of the percentage of total cells labeled positive for Hoechst dye in 2 Gy tLDRT-treated, 4Gy tLDRT-treated and corresponding abscopal calvarium regions for non-leukemic mice (n=2 mice per group, one abscopal and one treated calvarium region per mouse).

	2Gy tLDRT (n=3 mice)		4Gy tLDRT (n=3 mice)	
	Abscopal	Targeted Tissue	Abscopal	Targeted Tissue
Mice 9 Days post ALL Injection				
Femur ALL Engraftment (%)	28.5±6.3	12.2±1.7	34.5±0.8	16.4±2.7*
Calvarium ALL Engraftment (%)	35.4±7.0	28.1±3.6	25.2±2.1	18.4±5.3
Hoechst+ Cells in ALL Fraction In Femur (%)	95.3±0.9	96.4±0.7	92.0±1.1	93.9±1.0
Hoechst Mean Fluorescent Intensity of ALL Cells in Femur (AU)	12.0±1.0	13.4±0.9	10.4±0.5	12.8±0.6*
Hoechst+ Cells in ALL Fraction In Calvarium (%)	63.5±3.0	88.3±3.6**	72.6±7.2	84.5±0.7
Hoechst Mean Fluorescent Intensity of ALL Cells in Calvarium (AU)	10.4±0.7	12.3±0.9	10.4±0.3	13.7±1.2
Mice 7 Days post ALL injection				
Femur ALL Engraftment (%)	26.8±3.8	6.4±1.3*	35.3±11.4	5.4±2.6
Daunorubicin+ Cells in ALL Fraction in Femur (%)	72.3±1.8	90.8±2.3**	78.0±3.4	93.5±3.7*
Daunorubicin Mean Fluorescent Intensity of ALL Cells in Femur (AU)	27.0±1.1	37.8±2.5*	27.9±2.8	48.0±10.4

Table 2-1: ALL cellular uptake of Hoechst Dye and Daunorubicin

* Indicates Welch 2-sided t test value of $P < .05$ when comparing matching abscopal and targeted tissue regions.

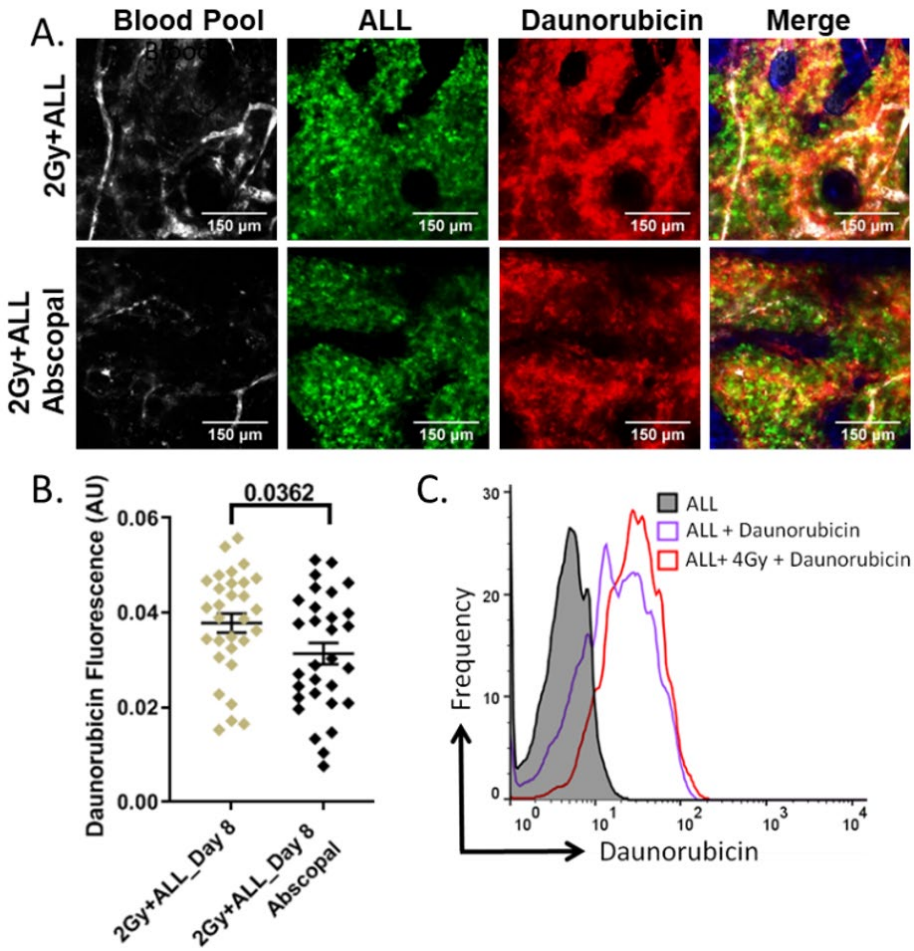

Figure 2-16: (A) QMPM images of treated and abscopal calvarium regions for a mouse receiving 2 Gy tLDRT. Qtracker™ 655 vascular blood pool fluorescence is in gray, GFP ALL fluorescence is in green, daunorubicin fluorescence is in red, and bone-collagen second harmonic generation displayed in the merged image is in blue. Daunorubicin was injected 20 minutes prior to imaging. (B) Cellular daunorubicin fluorescence taken from image segmentation of 30 single ALL cells with the highest GFP fluorescent intensity for 2 Gy tLDRT-treated and abscopal regions shown in A. (C) Representative histograms of daunorubicin fluorescence from ALL cells from crushed femur bone marrow samples.

To test the treatment efficacy of the therapeutic delivery enhancements after neo-adjuvant LDRT, we treated mice with 4 Gy TBI in combination with nilotinib. TBI was chosen for treatment since it had similar effects on the BMV as tLDRT and it was more suitable as a treatment regimen. Four-Gy dose was chosen because it exhibits increased cell killing effects compared to 2Gy with similar enhancements in therapeutic delivery. A treatment schema is shown in Figure 2-17 showing untreated, nilotinib, 4 Gy

TBI, 4Gy TBI after nilotinib, and 4 Gy TBI before nilotinib treatment groups. Significantly increased percentages of ALL in the peripheral blood were found in mice treated with 4Gy TBI after nilotinib compared with mice treated with 4 Gy TBI before nilotinib at both 15 days (22.3%, P=0.031) and 17 days (36.5%, P=0.0086) after the start of treatment. A significant increase of 8.5 days in median survival was found when administering 4 Gy TBI before nilotinib compared to 4 Gy TBI after nilotinib (P=0.0036). Results show a substantial survival benefit when performing 4 Gy TBI before administering nilotinib (Figure 2-17).

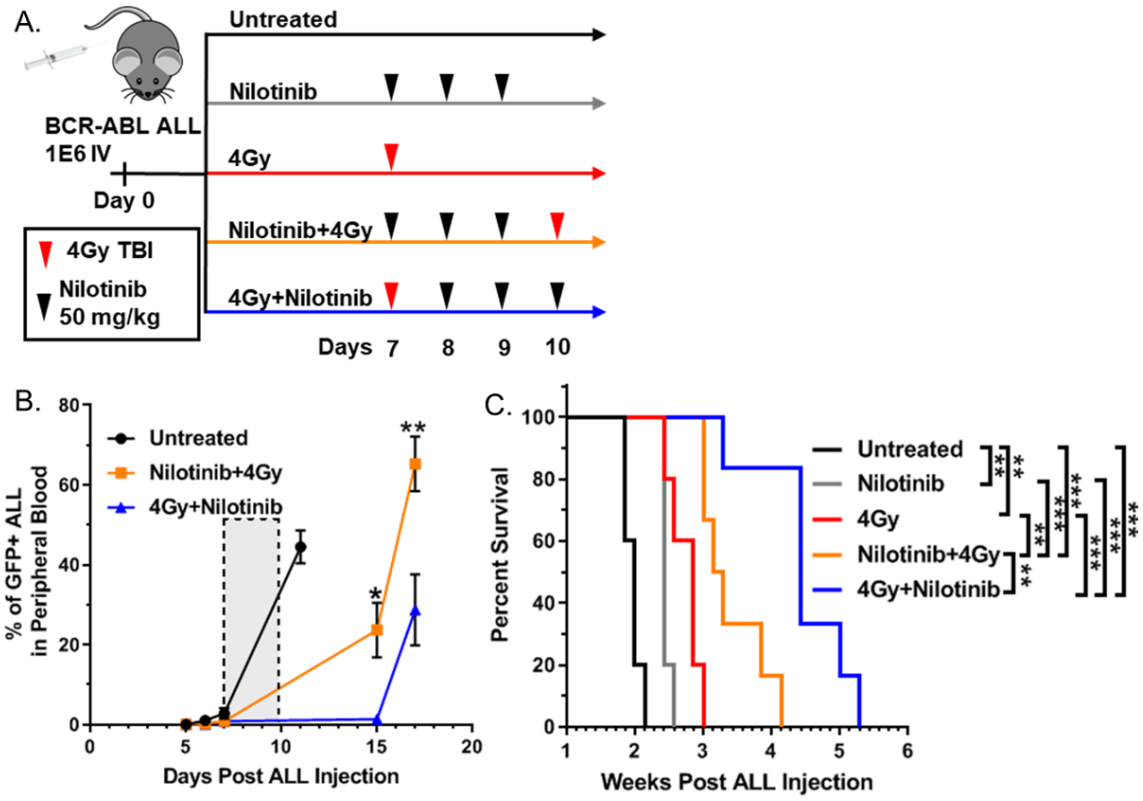

Figure 2-17: (A) A treatment schema for mice bearing ALL is shown for untreated, nilotinib , 4 Gy TBI, nilotinib before 4 Gy TBI, and 4 Gy TBI before nilotinib treatment groups. Treatment was started at day 7, when ALL could be detected in the peripheral blood of all the mice. (B) A plot of the percentage of ALL in peripheral blood for untreated (n=4, 5, 5, 5 mice per time point for days 5, 6, 7, 11 respectively), 4Gy TBI after nilotinib (n=6 mice per time point), and 4 Gy TBI before nilotinib (n=6, 6, 6, 4, 6 mice per time point for days 5, 6, 7, 15, 17 respectively) treatment groups (*=p<0.05, **=p<0.01).The gray shaded box indicates days 7-10 when treatment was administered. (C) The survival plot for mice bearing ALL receiving no treatment, nilotinib only, 4 Gy TBI

only, 4Gy TBI after nilotinib, and 4 Gy TBI before nilotinib is shown (n=5, 5, 5, 6, 6 mice per group respectively). Significant differences in survival are seen between all treatments except nilotinib only and 4 Gy TBI only treatments (*=p<0.05, **=p<0.01, ***=p<0.001, ****=p<0.0001).

2.4 Discussion

In this study, compartmental modeling and multiphoton microscopy were combined to create QMPM, a single-platform method to both measure BMV functional characteristics and assess the pharmacokinetics of fluorescent therapeutic analogues. Assessments of mice bearing ALL revealed increased permeability, altered K_{trans}, increased v_{ec}, reduced vascular blood flow, increased mean vessel density, and reduced mean vessel diameter. ALL-induced alterations reduce cellular drug uptake of therapeutics. As hypothesized, LDRT increased BMV blood flow and enhanced therapeutic delivery to ALL cells in the bone marrow. Consequently, 4 Gy TBI prior to the administration of nilotinib significantly increased the survival of mice bearing ALL compared to treatment with TBI after nilotinib administration. These results demonstrate the ability of QMPM to characterize and optimize the malignant vasculature for combination therapy.

QMPM can model the transport of therapeutic analogues in the local tissue and vascular compartments to obtain K_{trans} and v_{ec}. Changes in the vascular transport of molecular agents occur early in the progression of malignant disease, making v_{ec} and K_{trans} useful as potential biomarkers and for assessing drug or oxygen delivery [43, 79]. Limited work has been done with microscopy to perform tissue compartmental modeling for the identification of vascular permeability [47, 57]. Moreover, to our knowledge there have been no successful attempts using time-lapsed microscopy data to perform compartment modeling and obtain both K_{trans} and v_{ec} for the local vasculature. Differences in tracer concentration between the local vasculature and arterial blood may

be present in poorly perfused tissues [48, 80]. In such a case, QMPM images of the local vasculature will represent the local tracer transport rather than the typical transport from arterial blood to whole tissue. However, in the case of well perfused tissue, as is likely in this work, arterial and local vascular blood concentration measurements will be relatively similar. QMPM can be used in many different tissue types with many fluorescent agents, making it applicable to a wide variety of biological applications such as delivery of nutrients, oxygen, and therapeutics.

At low to moderate leukemic burden, dextran-based K_{trans} is increased compared to that in healthy mice, likely because of increased BMV permeability, enabling faster dextran leakage through the endothelial wall. Increased K_{trans} values in low to moderate burden ALL may indicate a therapeutic window of enhanced delivery for ALL antibody therapies, such as those targeting CD19 or CD22, which are similar in size to 150KDa dextran [81, 82]. However, differences in vascular transport mechanisms of dextran and therapeutic antibodies make further assessments of antibody delivery kinetics necessary [83]. In contrast to 150kDa dextran, small molecular agents such as Hoechst and daunorubicin can easily cross the vessel wall of both healthy and ALL-burdened BMV. This results in decreased cellular uptake of small sized therapeutics with the onset of ALL, due in part to reduced blood flow.

Previous reports have shown arterial and sinusoidal blood vessels to be linked with phenotypes observed in healthy mice. Small diameter, fast flow BMV correlates with arterial vessels, whereas large diameter, slow flow BMV correlates with sinusoidal vessels and venules for healthy mice [56, 57]. With ALL vascular remodeling, the structure of the healthy BMV is lost because of unchecked angiogenesis, creating semi-collapsed, immature, permeable vessels. This results in poor delivery of therapeutic agents, oxygen, and nutrients through the BMV. Increased hypoxia in the bone marrow

has been reported with multiple hematological malignancies and is likely due to similar vascular alterations as reported in this work [34]. Additionally, early preservation of the healthy BMV by the inhibition of vascular remodeling *in vivo* has been shown to give a survival advantage for leukemic mice treated with chemotherapy, suggesting drug delivery is hampered by the onset of malignancy [8]. A restoration of BMV blood flow and reduction of high disease burden are crucial to improve the delivery of therapeutics to the bone marrow.

This study suggests a possible new role for LDRT in restoring the biophysical function of the malignant BMV for combination therapies. Neo-adjuvant, LDRT treatments to ALL-burdened mice enhance BMV blood flow, increase delivery of therapeutics, and improve treatment efficacy. Similar RT-induced vascular alterations in solid tumors have been reported and may stem from nitrous oxide-dependent vasodilation [31]. Our results demonstrate the ability of LDRT to actively alter the BMV and indicate a possible new treatment approach for hematological malignancies. While recently developed total marrow irradiation is capable of delivering highly conformal treatment to the bone marrow [40, 84, 85] or to smaller regions of high disease burden, it is often used in conjunction with high dose regimens to enhance cell killing [86]. In contrast, LDRT can provide both cell killing and vascular modulation to enhance therapeutic delivery in desired regions.

With the wide variety of therapeutics that can be used with LDRT, consideration should be given to select synergistic treatment approaches. LDRT treatments may be particularly effective for vasculature targeting therapeutics, where delivery depends only on vascular blood flow to endothelial cells. Vascular disrupting agents frequently illicit off-target toxicity [87], and therapies designed for vascular normalization frequently lead to pathway resistance, making combination therapy with RT desirable [88, 89]. Vascular

targeted therapeutics show synergistic effects following low-to moderate-dose RT in solid tumor models, allowing for reduction in drug delivery without compromising treatment efficacy [90]. Immunotherapy has also shown synergy with LDRT in solid tumor models [91]. Additionally, LDRT for hematopoietic malignancies can be explored with more traditional therapeutic agents that elicit off-target toxicity or have synergistic effects [92, 93].

2.5 Conclusion

In conclusion, LDRT-induced alterations to functional BMV characteristics are one example of the many possible applications for QMPM. Simultaneous measurements of both functional single-vessel BMV characteristics and therapeutic pharmacokinetics using QMPM can observe and optimize oxygen, nutrient, and drug transport for many disease models and tissues. In the context of ALL, such measurements are crucial to understand LDRT treatment-induced BMV alterations and their effects on treatment outcome. Future work exploring LDRT will investigate the effects of timing, dose, and dose fractionation on the treatment of hematological malignancies. QMPM measurements will be essential to observe the BMV for LDRT-based combination therapies.

Chapter 3: L-QMPM to directly assess drug delivery potential of the bone marrow vasculature

This chapter is based largely on a manuscript that has been submitted to the international journal of radiation oncology, biology physics for publication in February 2021, by Brooks J, Zuro D, Song J, Madabushi S, Sanchez J, Kortylewski M, Chen B, Gupta K, Storme G, Froelich J, Hui S titled "Longitudinal preclinical imaging characterization of drug delivery potential after radiotherapy in the healthy and leukemic bone marrow vascular microenvironment". It is available for viewing in pre-print at: https://doi.org/10.1101/2021.02.23.432514

3.1 Introduction

In chapter 2, QMPM was used to discover that low dose (2-4 Gy) RT increases single-vessel blood flow in mice bearing ALL [94]. Increases in blood flow coincided with increased cellular uptake of chemotherapy, as well as improved survival outcome for mice treated with chemotherapy after neo-adjuvant low-dose radiotherapy. However, the correlation between improved BMV blood flow and improved cellular uptake of chemotherapy does not assure increased drug delivery potential after RT. Additional factors influence cellular uptake of therapeutics, such as tissue cellularity and the affinity of cells to uptake chemotherapy [95]. Furthermore, measurements of cellular drug uptake are limited to single time-point measurements, and do not have the ability to

observe longitudinal changes required for sustained drug delivery. Therefore, longitudinal measurements of drug delivery potential would be beneficial to assess the effectiveness of RT in conditioning the BMV for chemotherapy delivery.

In this chapter we develop longitudinal quantitative multiphoton microscopy (L-QMPM) to, 1) directly assess the drug delivery potential of the BMV after RT, 2) quantify potential time-lapsed imaging-based disease biomarkers, and 3) better understand the relationship between underlying vascular alterations and measurements obtained from DCE imaging. We quantified drug delivery potential primarily as the extravascular tissue wash-in slope (WIS_{tissue}) calculated using time-lapsed imaging of 4kDa dextran. 4kDa sized dextran was chosen as it is similar in size to typical DCE MRI imaging contrast agents as well as most standard chemotherapies for leukemia and has a minimal effect on the bone marrow microenvironment [60]. We measured several additional time-lapsed imaging and microvascular parameters, including K_{trans} and single-vessel blood flow to understand how the BMV influences changes in DCE imaging parameters and WIS_{tissue}. We performed L-QMPM imaging in the calvarium of mice bearing ALL or AML, two common types of leukemia, as well as wild-type (WT) controls, to assess the response of the healthy and leukemic BMV to RT. We hypothesized that RT would increase WIS_{tissue} in the calvarium bone marrow of mice bearing leukemia after both low (2 Gy) and high (10 Gy) dose total body irradiation (TBI).

3.2 Methods

3.2.1 Mice, cell lines, and study timing

All procedures for animal experimentation were performed according to City of Hope's guidelines and approved by the Institutional Animal Care and Use Committee. For all imaging studies, male and female C57BL/6 WT mice (Strain 556,

Charles River, Wilmington MA USA) 7-11 weeks in age were used. Mice were injected with $1x10^6$ green fluorescent protein $(GFP)^+$ BCR-ABL (p190Kd) expressing B-cell ALL cells [66] or $1x10^6$ GFP^+ *Cbfb-MYH11/Mpl*$^+$ AML cells [96]. The percentage of leukemia in peripheral blood (PB) and in bone samples was measured by flow cytometry as described previously [94].

For initial non-imaging studies of ALL growth kinetics, 6-week-old C57BL/6N mice (Strain 556, Charles River, Wilmington, MA) were used. Initial growth kinetic studies of AML were performed with 9-week-old male and female albino B6 mice (B6 Tyrc-2J/J-B6 stock No: 000058, Jackson Laboratories, Bar Harbor, ME). For ALL and AML cell injections, cells were suspended in 200 µl or 100 µl of phosphate buffered saline (PBS) respectively. ALL and AML injections were administered using tail vein or retro-orbital injections respectively.

Surgery on WT mice was performed 2 days before the start of imaging. ALL injections and headplate surgery on mice bearing ALL were performed 7-8 days and 2-3 before the start of imaging respectively. ALL was detectable in the peripheral blood (PB) of all sampled mice at the first imaging timepoint with PB readings ranging from 0.5% to 12.9%. Approximately 75% of the mice bearing ALL were sampled. An additional group of mice bearing ALL were treated with 10Gy at higher burden. ALL injections and headplate surgery for these mice was performed 10 and 2 days before the start of imaging respectively. PB readings of these mice at the start of imaging ranged from 32% to 55% for all mice. Headplate surgery on mice bearing AML was performed after mice reached 25% AML cells in PB. AML injections and headplate surgery were performed 10-16 and 2 days before the start of imaging, respectively. AML in the PB at the start of imaging ranged from 28% to 75.8% for all mice bearing AML (Figure 3-1). Each

treatment group for healthy and leukemic mice consisted of a minimum of two mice of each sex.

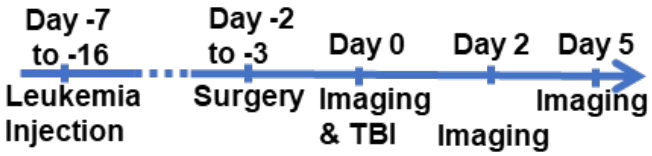

Figure 3-1: The timing schema for ALL or AML intravenous injection, cranial window surgery, TBI, and L-QMPM imaging is shown.

3.2.2 Cranial window surgery

Two days before surgery mice were given MediGel® Sucralose gel cups (Clear H_2O, Portland, ME) mixed with 1.125 mg of carprofen per cup. An additional cup was given on the day of surgery. For surgery, mice were anesthetized using 5% isoflurane initially at a flow rate of 1.0 L/min, and then maintained with 1.3% isoflurane at a flow rate of 0.8 liters per minute. A stereotactic apparatus with a bite bar was utilized to keep the mouse stable during surgery. The hair on the top of the skull was removed using a hair trimmer and the skin above the skull was sterilized using a topical antiseptic (Betadine®, Purdue Products L.P., Stamford, CT), and rinsed with saline. An incision was made to remove the skin and membrane above the calvarium, and a custom head plates made of carbon fiber or titanium with an inner diameter of 7mm or 8mm respectively was fixed to the calvarium using glass ionomer cement (Pearson PQ, Sylmar, CA). A round 5mm glass coverslip was placed on top of the exposed skull in the middle of the headplate, and was sealed with cyanoacrylate glue (Loctite 401™, Henkel, Düsseldorf, Germany). Mice were administered 0.5-1.0 mg/kg of buprenorphene-SR (ZooPharm, Fort Collins, CO) as an additional analgesic at the time of surgery.

3.2.3 L-QMPM image acquisition and analysis

For imaging, mice were anesthetized using 5% isoflurane initially at a flow rate of 1.5 L/min, and then maintained with 1.3% isoflurane at a flow rate of 0.8 liter per minute. The stereotactic head plate was inserted into a custom-built heated stage maintained at 37°C allowing for easy viewing of the mouse calvarium. Imaging was performed on the frontal bone region of the calvarium, near the sagittal suture for all mice, using the same system as described in section 1378065747.745753680.978588032.

Mice were catheterized intravenously through the tail vein [61] and injected with 350 µg of 4kDa TRITC dextran (TdB Consultancy, Uppsala Sweden) suspended in 100 µl of phosphate buffered saline (PBS) during time-lapsed imaging to observe drug delivery potential. Time-lapsed imaging consisted of 120 frames with 10.3 second frame interval at a 512 by 512 pixel resolution.

To identify the vascular region from the tissue region, a second injection of either 400 µg of 2MDa FITC dextran (TdB Consultancy, Uppsala Sweden) suspended in 100 µl of PBS or 10µl of Qtracker™ 655 Vascular Label mixed with 90 µl of PBS was performed after time-lapsed imaging. Immediately after injection, a series of fast, five-slice z-stack images with 15 µm spacing, 512 by 512 pixel resolution, and no averaging were taken from 5 locations before tissue leakage of FITC dextran or Qtracker™ occurred. Substantial leakage was often present in mice treated with TBI due to loss in cellularity and vascular damage. This made clear viewing vascular morphology difficult after the first 2-3 minutes in most irradiated mice. Three-dimensional tiled z-stack images of ALL and blood pool fluorescent contrast were obtained with settings of 10um slice spacing, 512 by 512 pixel resolution, two averages and individual image overlap of 15-20%. FITC and TRITC dextran excitation was performed at 820nm. Qtracker™

excitation, GFP+ leukemia excitation, and second harmonic generation of the collagen in the bone was performed at 900nm.

Three separate fast z-stack images were used to manually measure mean vessel density and mean vessel diameter for each mouse using Fiji/ImageJ [68]. Measurements of corrected single-vessel blood flow were acquired using Equations 1-5 & 1-6 [2]. Tiled z-stack images were stitched together using a Fiji/ImageJ plugin [70].

To identify the vascular tissue ROI, an Otsu's threshold [71] was applied to blood pool agent images of the vasculature. To identify the extravascular tissue ROI, the vascular tissue ROI was cropped out of the 4kDa dextran image and an Otsu's threshold was applied to the 15^{th} frame of the dextran time-lapsed images. If a single threshold was not adequate to properly segment the extravascular tissue ROI from the background, the first extravascular ROI region was subtracted from the image and a second Otsu's threshold was applied. The two extravascular tissue regions were then combined to identify the extravascular tissue ROI. Two thresholds were only applied in a few cases where there was extensive heterogeneity in tissue signal intensity in the image. The whole tissue ROI was identified by combining extravascular and vascular ROIs. After identifying initial ROIs, boundary edge erosion was applied to the regions to better isolate dextran fluorescent signal coming from the respective tissue compartments. An 8 pixel boundary erosion was applied to extravascular and whole tissue ROIs. A 4 pixel boundary erosion was applied to the vascular tissue ROI.

Time-lapsed imaging of 4kDa TRITC dextran were analyzed using a custom Matlab® (R2018a 9.41.0.81364, MathWorks Natick, MA) script obtaining compartmental modeling parameters and descriptive curve analysis of dextran uptake. Images frames were co-registered to minimize spatial drift between frames of time-lapsed images. For calculation of K_{trans}, K_{ep}, and v_{ec} removal of saturated pixels from extravascular and

vascular ROI's was performed prior to analysis. To do this, the percentage of saturated pixels from the ROI with the highest percentage of saturated pixels was identified, and that percentage of pixels was removed from both the vascular and extravascular ROIs. Saturated pixels were only present for a subset of the total images, and in general the removal of saturated pixels made little change to the overall signal intensity from ROIs. The concentration of dextran in the vascular and extravascular tissue ROI was modeled using Equation 1-3.

Analysis of the extravascular tissue ROI signal contributions to PH_{whole} was performed using Equation (3-1)

$$SC_{tissue} = \frac{\mathrm{SI}_{tissue} * A_{tissue}}{\mathrm{SI}_{tissue} * A_{tissue} + SI_{blood} * A_{blood}} \qquad (3\text{-}1)$$

Where SI_{tissue} and SI_{blood} are the mean fluorescent intensities from the extravascular and vascular tissue ROIs after boundary erosion is performed at the time that PH_{whole} is measured. A_{tissue} and A_{blood} are the areas covered by the extravascular and vascular tissue ROIs before boundary erosion is performed.

The additional parameters of dextran accumulation that we quantified included WIS_{tissue} , wash-in slope for the whole tissue ROI (WIS_{whole}), peak height for the extravascular tissue ROI (PH_{tissue}), peak height for the whole tissue ROI (PH_{whole}), and peak height for the vascular tissue ROI (PH_{blood}). WIS_{whole} and PH_{whole} were quantified as measurements similar to macroscopic DCE imaging to identify how signal contributions from the vascular and extravascular tissue influence DCE imaging (Figure 3-2) [47].

We obtained WIS_{tissue} and WIS_{whole} by dividing the largest positive change in fluorescent intensity between each frame by the time interval between frames for the ROIs of the extravascular and whole tissues, respectively. PH_{blood}, PH_{tissue}, and PH_{whole}

were calculated by first subtracting the pre-injection background fluorescence from time-lapsed images, then measuring the dextran fluorescent intensity value of the frame with the highest fluorescent intensity for vascular, extravascular, and whole tissue ROIs, respectively [42].

A.

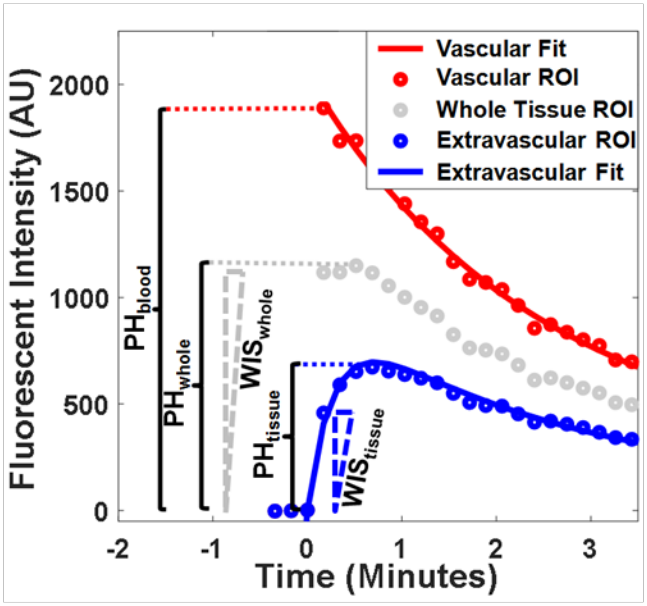

B.

	Measurement description	Related to:
WIS_{tissue}	Accumulation rate of dextran in the tissue	Drug delivery potential
PH_{tissue}	Maximum concentration of dextran in tissue	Extracellular tissue space and local vascular concentration
PH_{blood}	Maximum concentration of dextran in the local vasculature	Arterial blood concentration and local blood flow
WIS_{whole}	Accumulation rate of dextran in the combined tissue and vasculature	Primarily volumetric blood flow rate (macroscopic imaging-capable measurement)
PH_{whole}	Maximum concentration of dextran in the tissue and vasculature	PH for vascular and extravascular tissue combined (macroscopic imaging-capable measurement)
v_{ec}	Fraction of extravascular space that is extracellular	Cellular density
K_{trans}	Transfer rate of dextran between the local vasculature and tissue	Vascular permeability, vascular surface area, and blood flow
K_{ep}	Backflux rate	equal to K_{trans}/v_{ec}

Figure 3-2: (A) Fluorescent intensity data from extravascular tissue, vascular tissue, and whole tissue ROIs from time-lapsed L-QMPM images shown to graphically illustrate measurements. Solid lines represent fitted functions for the vascular and extravascular tissue compartments used to obtain K_{trans}, K_{ep}, and v_{ec}. WIS_{tissue} and WIS_{whole} are depicted as the maximum positive slope between image frames for the extravascular tissue ROI and whole tissue ROI, respectively. (B) The list provides a description of the parameters of interest for Chapter 3 and the relation of the parameters to physiological parameters in the bone marrow.

3.2.4 TBI treatments, head plate dosimetry, and dose simulations

We used the Precision X-RAD SMART Plus / 225cx small animal image guided irradiation system[72] to administer TBI treatments in a single-fraction of a 2 or 10 Gy soft-tissue-equivalent dose, acquire CT images, and perform dose calculations [73, 74]. TBI treatments were performed while mice were conscious with x-ray tube settings of 225 kVp and 13 mA with a 0.32 mm copper filter. CT imaging was performed on mice under anesthesia (2% isoflurane at a flow rate of 1.5 liters per minute) with x-ray tube settings of 40 kVp and 13 mA at a 0.2 mm voxel size with a 2.0 mm aluminum filter. Film dosimetry was performed using Gafchromic™ EBT3 film (Ashland Specialty Ingredients, Bridgewater NJ). The film was initially calibrated at the isocenter of the system after verification of the dose with an externally calibrated ion chamber (PTW TN30013 Farmer Chamber, Freiburg, Germany). An output dose of approximately 1.5 Gy was chosen for headplate dosimetry as it was the dose in the center of the linear response of the film (data not shown). Dose calculations and isodose line visualization were performed by the small animal RT planning system [72], using a Monte Carlo dose engine [73, 74].

3.2.5 Histology preparation and scoring

After completion of imaging 5 days after RT, bone tissues were dissected and fixed in 10% neutral buffered formalin for 48 hours. Bone tissues were decalcified using Richard-Allan Scientific™ Decalcifying Solution (Thermo Scientific™) with 6 hours incubation and raised. Dehydration, clear, and paraffinization was performed on a Tissue -Tek VIP Vacuum Infiltration Processor (Sakura Finatek, Torrence, CA, USA). The samples were then embedded in paraffin using a Tissue-Tek TEC Tissue Embedding Station (Sakura Finatek), cut at 5 μm and stained with a Tissue -Tek Prism Plus automated H&E Stainer (Sakura Finatek) according to standard laboratory procedures.

Dual IHC stain for CD31 (Clone: D8V9E Rabbit monoclonal antibody, Cell Signaling Technologies, Danvers, MA, USA) and GFP (Clone: D5.1 Rabbit monoclonal antibody, Cell Signaling Technologies, Danvers, MA) was performed on Ventana Discovery Ultra automated IHC stainer (Ventana Medical Systems, Roche Diagnostics, Indianapolis, USA). Briefly, after deparaffinization, rehydration, endogenous peroxidase activity inhibition and antigen retrieval, the two antigens were sequentially detected, and heat inactivation was performed to prevent antibody cross-reactivity between the same species. Following each primary antibody incubation, DISCOVERY anti-Rabbit HQ and DISCOVERY anti-HQ-HRP were incubated. The stains were then visualized with DISCOVERY Teal kit and DISCOVERY Purple Kit, respectively, counterstained with haematoxylin (Ventana), and coverslipped. Whole slide images were acquired with a Ventana iScan HT Scanner (Roche Diagnostics, Indianapolis, IN, USA) and viewed by iScan image viewer software. Histological vessel density scoring was performed manually using femur sections stained for CD31 to identify endothelial cells. Two separate images were quantified for vessel density per mouse. All pathological findings were verified by a board-certified pathologist with expertise in bone marrow pathology (Joo Y Song MD, City of Hope National Medical Center).

3.2.6 Statistical analysis

We performed all statistical testing using Prism (V.9.00 (121), GraphPad). For analysis of the treatment effects, a two-way mixed-effects model was performed followed by Tukey's post-hoc comparison when appropriate. We performed post-hoc comparisons with 3 families and 3 comparisons per family for both time and treatment group comparisons. Measurements of leukemia in the PB of mice in treatment groups were compared using a one-way mixed-effect model for cross group and longitudinal comparisons. Unless stated otherwise, we performed all other significance testing using

a Welch's two-sided t-test. All distribution error bars are displayed as the mean plus or minus one standard deviation.

3.3 Results

3.3.1 Head plate dosimetry

Dosimetry measurements and CT-based dose simulations were performed to ensure minimal perturbation in dose due to cranial window surgery and implantation of the cranial window headplate. Significant differences in dose were noticed between a lack of head plate and directly under the titanium head plate material, whereas no significant differences were noticed between a lack of head plate and carbon fiber headplates (Figure 3-3).

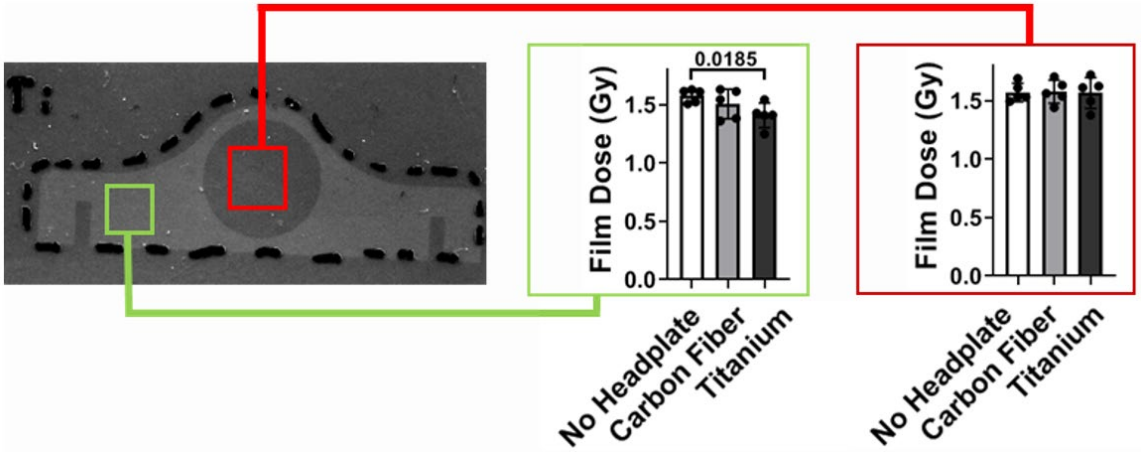

Figure 3-3: A picture of dosimetric film after x-ray exposure while directly underneath a titanium head plate. Film dose measurements from a lack of head plate, carbon fiber head plates, and titanium head plates obtained both underneath the head plate (Green) material and in the imaging area (Red).

We observed significant artifacts in CT images of mice with titanium head plates. However, no artifacts were present for carbon fiber head plates (Figure 3-4). For these reasons, we utilized carbon fiber head plates for all L-QMPM imaging studies.

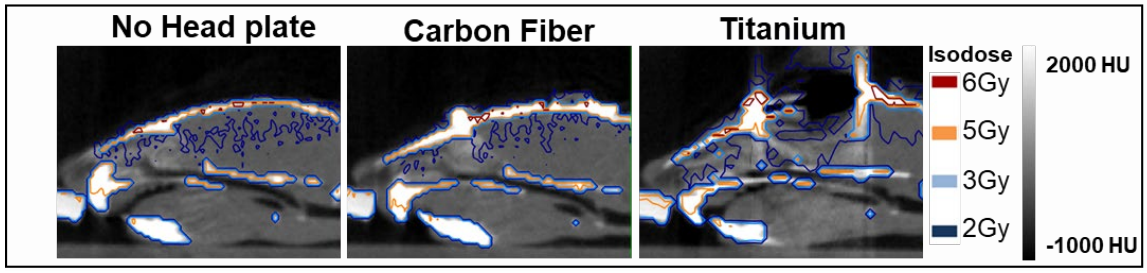

Figure 3-4: CT images with corresponding isodose lines for mice with no head plate, carbon fiber head plate, and titanium head plate.

3.3.2 AML and ALL alterations result in increased vessel density, reduced blood flow, and reduced WIS_{tissue}

We split L-QMPM imaging data into different relative low and high leukemic burden groups using PB measurements based on the timing of changes in single vessel blood flow with the onset of ALL or AML (Figure 3-5). A single measurement time-point from each mouse, typically matching the highest untreated disease burden was used for analysis of all imaging parameters for pretreatment analysis.

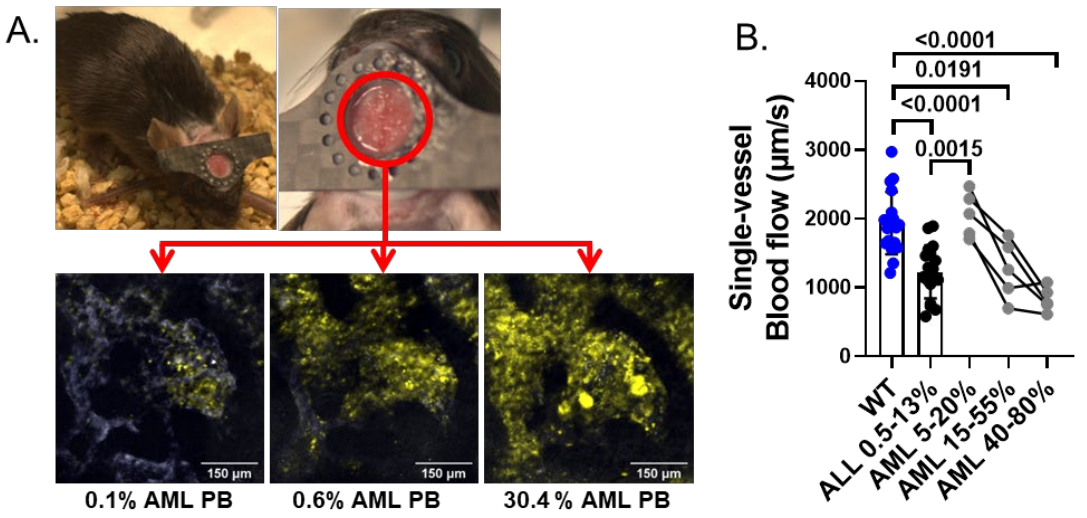

Figure 3-5: (A) Photos of mice with longitudinal cranial windows and L-QMPM Images of GFP+ AML cell growth (Green) in the calvarium at 4, 6, and 10 days post AML injection shown with corresponding percentages of AML in the peripheral blood. (B) Single-vessel blood flow values for WT mice and mice with varying percentages of leukemia in PB. Mice bearing ALL were imaged 7-8 days after ALL injection and mice bearing AML were imaged longitudinally 9, 11, and 14 days after AML injection.

To understand the differences between the timing of single-vessel blood flow changes in mice bearing AML or ALL, we characterized the growth kinetics of leukemia in the PB, femur, and calvarium. No significant time-matched differences in the percentage of leukemia in the PB of mice were found between mice bearing ALL and AML post leukemia-cell injection (P=0.5757). However, in the calvarium, we observed significantly higher engraftment of ALL compared to AML (P=0.014). Similar differences were found in the femur bone marrow (P=0.0330). The data suggest that differences in vascular function may be due to differences in the onset of leukemia engraftment in the calvarium and femur bone marrow (Figure 3-6).

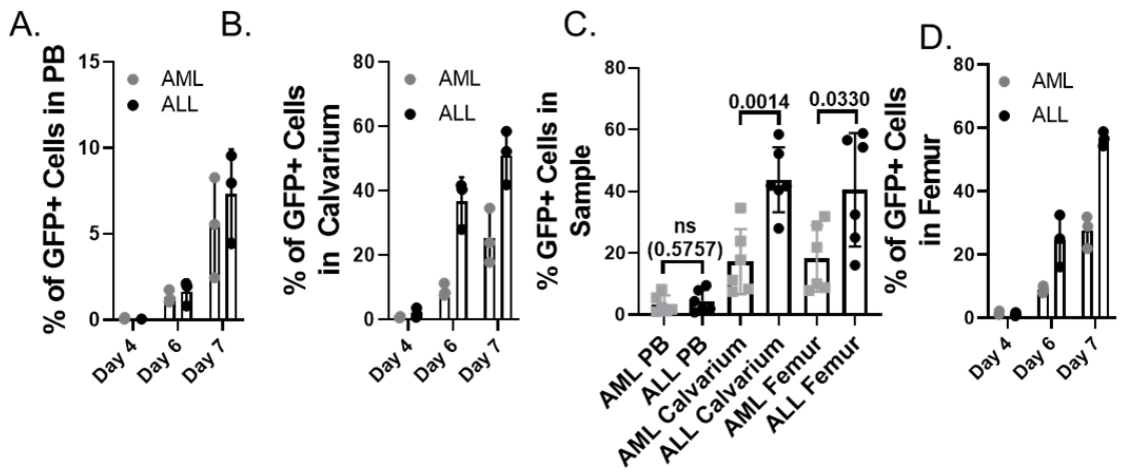

Figure 3-6: The percentage of GFP+ ALL or AML cells in total cells for (A) peripheral blood, (B) crushed calvarium marrow, and (D) crushed femur marrow samples 4, 6, and 7 days post AML or ALL injection. Measurements were taken using flow cytometry.(C) Comparison of the percentage of GFP+ ALL or AML cells in total cells for peripheral blood, crushed calvarium marrow, and crushed femur marrow samples taken from matching mice harvested 6 and 7 days after AML or ALL injection.

Reduced vascular diameter, increased vessel density, and reduced single-vessel blood flow were observed in mice bearing leukemia at both low and high leukemic burden compared to WT mice (Figure 3-7). BMV changes at low disease burden coincided with decreased WIS_{whole} for mice bearing leukemia compared to WT mice (P=0.0178 and P=0.0018, respectively). We observed decreases in K_{ep} and increases in v_{ec} in mice bearing AML at low leukemic burden compared to WT mice (P<0.0001 and P=0.0412, respectively).

At high leukemic burden, we observed decreases in WIS_{tissue} for mice bearing ALL and AML compared to WT mice (P=0.0001 and 0.0001, respectively). We additionally observed decreased K_{trans} at high AML burden (P<0.0001, Figure 3-8). Significant differences for time-lapsed imaging parameters in mice bearing leukemia at high disease burden included decreased WIS_{tissue}, WIS_{whole}, PH_{whole}, PH_{blood}, K_{ep}, as well as increased v_{ec} compared to WT mice (Table 3-1). The most effective time-lapsed

imaging parameter to distinguish between mice bearing leukemia and WT mice was WIS_{whole} (Figure 3-9).

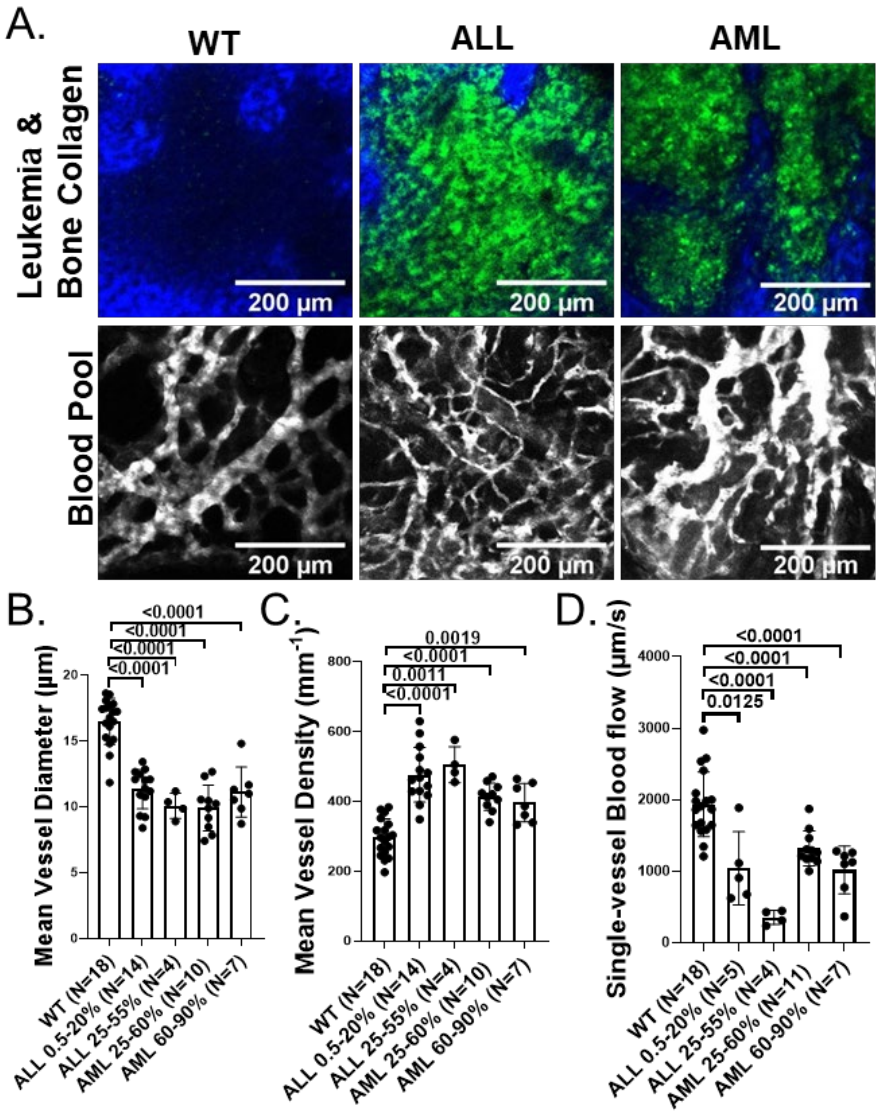

Figure 3-7: (A) Top images: L-QMPM images of GFP+ leukemia (green) and second harmonic generation from the collagen in the bone (blue); bottom images: L-QMPM images of BMV blood pool fluorescence from Qtracker™ 655 vascular labels (white). Plots of L-QMPM measurements of (B) mean vessel diameter, (C) mean vessel density, and (D) single-vessel blood flow for WT mice, and mice bearing low and high burdens of AML or ALL as measured by the percentage of leukemia in the peripheral blood.

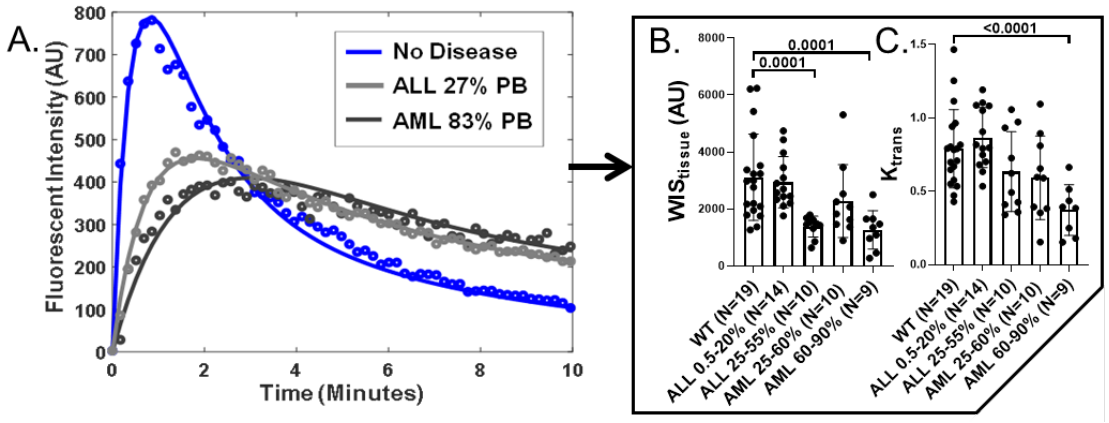

Figure 3-8: (A) Dextran fluorescence from extravascular tissue ROIs used for time lapsed images from a WT mouse, and mice bearing AML or ALL. Solid lines indicate the corresponding fitting function used for compartmental modeling. L-QMPM measurements of (B) WIS_{tissue} and (C) K_{trans} for WT mice and mice with varying ALL or AML burdens measured through PB sampling.

	No Disease		ALL 0.5-20% PB		ALL 25-55% PB		AML 25-60% PB		AML 60-90% PB	
	Mean ± Standard Deviation	(N)	Mean ± Standard Deviation	P value (N)	Mean ± Standard Deviation	P value (N)	Mean ± Standard Deviation	P value (N)	Mean ± Standard Deviation	P value (N)
WIS_{tissue}	3114 ± 1518	(19)	2940 ± 899	0.6835 (14)	1380 ± 363.9	**0.0001** (10)	2280 ± 1279	0.1326 (10)	1268 ± 673.5	**0.0001** (9)
WIS_{whole}	7907 ± 3648	(19)	5525 ± 1621	**0.0178** (14)	2153 ± 671.8	**<0.0001** (10)	4417 ± 1776	**0.0018** (10)	3024 ± 1549	**<0.0001** (9)
PH_{tissue}	955 ± 524	(19)	989 ± 468	0.844 (14)	741 ± 230	0.1404 (10)	926 ± 421	0.8726 (10)	634 ± 286	**0.04688** (9)
PH_{whole}	1445 ± 654	(19)	1293 ± 487	0.449 (14)	865 ± 292	**0.0028** (10)	1099 ± 430	0.0999 (10)	753 ± 328	**0.001** (9)
PH_{blood}	2512 ± 749	(19)	2286 ± 496	0.3063 (14)	1268 ± 356	**<0.0001** (10)	2256 ± 486	0.2779 (10)	1809 ± 866	0.0554 (9)
v_{ec}	0.276 ± 0.067	(19)	0.274 ± 0.084	0.9625 (14)	0.364 ± 0.055	**0.001** (10)	0.365 ± 0.114	**0.0412** (10)	0.37 ± 0.069	**0.006** (8)
K_{trans}	0.79 ± 0.267	(19)	0.866 ± 0.205	0.361 (14)	0.634 ± 0.272	0.1557 (10)	0.593 ± 0.285	0.0865 (10)	0.372 ± 0.173	**<0.0001** (8)
K_{ep}	2.93 ± 0.89	(19)	3.39 ± 1.07	0.1989 (14)	1.73 ± 0.64	**0.0003** (10)	1.61 ± 0.53	**<0.0001** (10)	1 ± 0.46	**<0.0001** (8)
Vessel Density (mm^{-2})	296 ± 53	(18)	476 ± 78	**<0.0001** (14)	505 ± 52	**0.0011** (4)	413 ± 39	**<0.0001** (10)	396 ± 55	**0.0019** (7)
Mean Vessel Diameter (μm)	16.5 ± 1.7	(18)	11.4 ± 1.5	**<0.0001** (14)	10.1 ± 1	**<0.0001** (4)	9.9 ± 1.7	**<0.0001** (10)	11.1 ± 1.9	**<0.0001** (7)
Single-vessel Bloodflow (μm/s)	1938 ± 454	(18)	1043 ± 511	**0.0125** (5)	357 ± 99	**<0.0001** (4)	1320 ± 243	**<0.0001** (11)	1020 ± 334	**<0.0001** (7)

Table 3-1: The imaging parameters for WT mice and mice bearing ALL or AML.

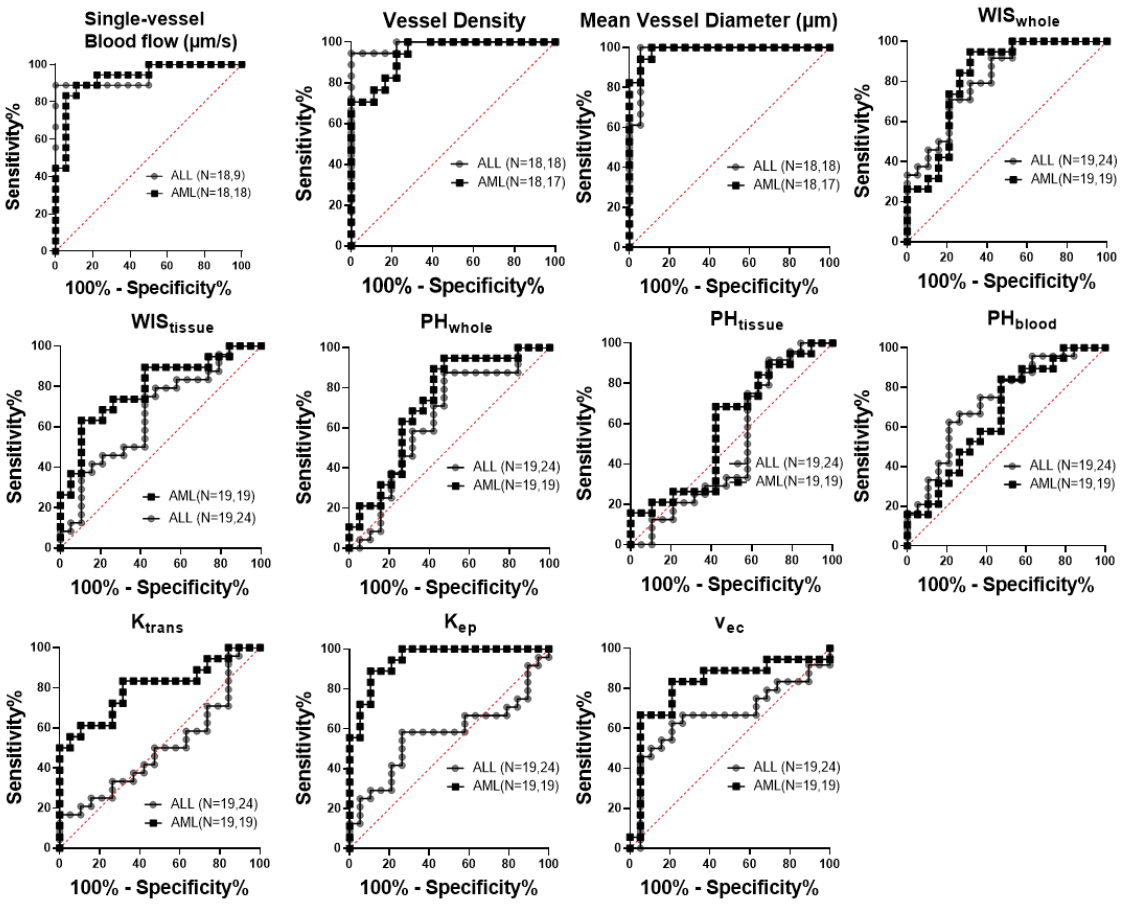

Figure 3-9: Receiver operating characteristic curve for a variety of L-QMPM parameters from L-QMPM images of untreated WT mice and untreated mice bearing AML and ALL.

We measured the percent signal contribution to PH_{whole} from the extravascular tissue ROI, to better understand peak height measurements in DCE imaging. Mean signal contribution was 55.7±16.7%, 64.9±3.7%, and 71.7±20.7% for untreated WT mice, and mice bearing ALL or AML, respectively. We observed no correlation between PH_{whole} and vascular density using data from untreated WT mice and mice bearing AML and ALL. (R^2=0.005, P=0.5235, Figure 3-10).

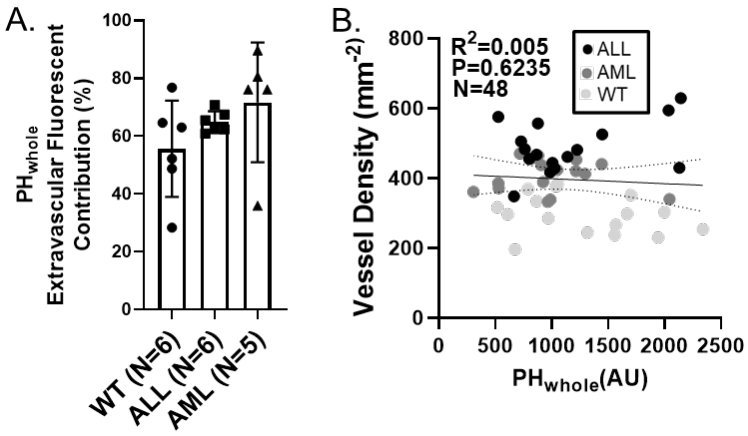

Figure 3-10: (A) The percentage contribution of the extravascular tissue ROI region fluorescent signal to the total signal in PH_{whole} for WT mice, and mice bearing AML or ALL. (B) A correlation plot of PH_{whole} and vessel density showing no significant non-zero correlation between the parameters.

3.3.3 Longitudinal validation, leukemia growth, and the effects of TBI on the bone marrow vasculature

We observed no significant differences in any imaging parameters in WT untreated mice between imaging time-points (Table 3-2). Additionally, no significant differences in any of the imaging parameters or leukemia PB measurements were observed prior to TBI treatments in treatment subgroups with matching types of disease, validating longitudinal and cross-group comparisons post-treatment (Table 3-3 & Table 3-4).

Treatment intervention for mice bearing AML and ALL was performed approximately when the percentage of leukemia in the PB reached the level where changes in BMV function were observed. An additional group of mice were treated at higher ALL burden to observe the effects of TBI after ALL had caused significant reductions in WIS_{tissue} (Figure 3-11, Table 3-5).

WT		Pretreatment Mean ± Standard Deviation	Day 2 Post-treatment Mean ± Standard Deviation	Day 5 Post-treatment Mean ± Standard Deviation
WIS_{tissue}	No RT (N=7)	3233 ± 1881	2887 ± 954	2227 ± 970
	2Gy (N=6)	2593 ± 898	3612 ± 1504†	1749 ± 462†¶
	10Gy (N=6)	3496 ± 1649	6317 ± 1927*	4938 ± 3232
WIS_{whole}	No RT (N=7)	7982 ± 4007	7241 ± 3590	5603 ± 3411
	2Gy (N=6)	6793 ± 2977	7492 ± 4395	4480 ± 2933
	10Gy (N=6)	8935 ± 4124	10513 ± 3891	8392 ± 3770
PH_{tissue}	No RT (N=7)	1097 ± 737	1043 ± 537	737 ± 399
	2Gy (N=6)	697 ± 223	826 ± 340	569 ± 255¶
	10Gy (N=6)	909 ± 257	2090 ± 588*§†	1703 ± 650*§†
PH_{whole}	No RT (N=7)	1503 ± 772	1407 ± 671	1048 ± 583
	2Gy (N=6)	1213 ± 497	1369 ± 736	891 ± 459†
	10Gy (N=6)	1609 ± 691	1929 ± 705	1610 ± 757
PH_{blood}	No RT (N=7)	2669 ± 782	2367 ± 907	2072 ± 1245
	2Gy (N=6)	2178 ± 626	2011 ± 854	1657 ± 968
	10Gy (N=6)	2663 ± 834	2460 ± 629	1997 ± 647
v_{ec}	No RT (N=7)	0.295 ± 0.096	0.337 ± 0.055	0.329 ± 0.074
	2Gy (N=6)	0.254 ± 0.054	0.308 ± 0.033	0.307 ± 0.086
	10Gy (N=6)	0.274 ± 0.031	0.422 ± 0.039*§§†	0.392 ± 0.097
K_{trans}	No RT (N=7)	0.725 ± 0.266	0.72 ± 0.21	0.793 ± 0.314
	2Gy (N=6)	0.726 ± 0.126	1.249 ± 0.35*†	0.688 ± 0.317¶
	10Gy (N=6)	0.93 ± 0.348	2.062 ± 0.409**§†	2.112 ± 1.334
K_{ep}	No RT (N=7)	2.49 ± 0.57	2.18 ± 0.73	2.52 ± 1.05
	2Gy (N=6)	2.92 ± 0.5	4.04 ± 1.03*†	2.37 ± 1.28¶
	10Gy (N=6)	3.45 ± 1.28	4.89 ± 0.9**	5.26 ± 2.32
Vessel Density (mm^{-2})	No RT (N=6)	291 ± 73	288 ± 41	273 ± 43
	2Gy (N=6)	307 ± 41	300 ± 51	277 ± 40
	10Gy (N=6)	290 ± 49	253 ± 26	200 ± 32*§†¶
Mean Vessel Diameter (μm)	No RT (N=6)	16.6 ± 1.9	15.6 ± 1.7	16.1 ± 1.9
	2Gy (N=6)	16.7 ± 0.9	20.3 ± 2.2*†	19.1 ± 3.2
	10Gy (N=6)	16.2 ± 2.4	20.8 ± 1.9*†	26.6 ± 4*§†¶
Single-vessel Blood flow (μm/s)	No RT (N=6)	2045 ± 485	1770 ± 352	1975 ± 445
	2Gy (N=6)	1863 ± 371	2300 ± 521	2338 ± 628
	10Gy (N=6)	1902 ± 550	2062 ± 600	1908 ± 455

Table 3-2: The imaging parameters for WT mice during treatment

$^{\#}$-PB samples were not taken in mice bearing ALL after RT as an appropriate number of cells could not be obtained from the maximum sampled blood volume
†-Significantly different from pretreatment time-point P<0.05
¶-Significantly different from 2 days post-treatment time-point P<0.05
* -Significantly different from no RT group P<0.05
§-significantly different from 2Gy treatment group P<0.05
††-Significantly different from pretreatment time-point P<0.001

¶¶-Significantly different from 2 days post-treatment time-point P<0.001
**-Significantly different from no RT group P<0.001)
§§-Significantly different from 2Gy treatment group P<0.001

AML		Pretreatment Mean ± Standard Deviation	Day 2 Post-treatment Mean ± Standard Deviation	Day 5 Post-treatment Mean ± Standard Deviation
% AML in PB	No RT (N=8,8,4)	47.7 ± 7.7	63.0 ± 12.0†	82.4 ± 6.7†
	2Gy (N=7)	54.9 ± 15.5	#	#
	10Gy (N=6)	47.9 ± 8.8	#	#
WIS_{tissue}	No RT (N=7,7,4)	2199 ± 655	1332 ± 622†	1138 ± 537†
	2Gy (N=7,7,6)	2082 ± 1528	4984 ± 1685*†	1785 ± 738¶
	10Gy (N=6)	2193 ± 737	6793 ± 1932*†	4723 ± 1943*§
WIS_{whole}	No RT (N=7,7,4)	5050 ± 1653	3599 ± 2063	3007 ± 1411†
	2Gy (N=7,7,6)	4299 ± 2257	7469 ± 2426*	3662 ± 1994
	10Gy (N=6)	4168 ± 909	10195 ± 3604*†	7041 ± 2392*
PH_{tissue}	No RT (N=7,7,4)	954 ± 259	571 ± 200†	549 ± 260
	2Gy (N=7,7,6)	902 ± 479	1817 ± 470**	721 ± 257¶
	10Gy (N=6)	909 ± 257	2090 ± 588*†	1703 ± 650*§†
PH_{whole}	No RT (N=7,7,4)	1111 ± 261	745 ± 302†	681 ± 322
	2Gy (N=7,7,6)	1084 ± 489	2004 ± 474**	871 ± 319¶
	10Gy (N=6)	1043 ± 279	2282 ± 633*†	1847 ± 630*§†
PH_{blood}	No RT (N=7,7,4)	2526 ± 367	2068 ± 949	1702 ± 856
	2Gy (N=7,7,6)	2374 ± 639	2581 ± 645	1857 ± 590
	10Gy (N=6)	2114 ± 497	2600 ± 841	2090 ± 599
v_{ec}	No RT (N=6,6,4)	0.366 ± 0.124	0.321 ± 0.051	0.367 ± 0.06
	2Gy (N=7,7,6)	0.344 ± 0.118	0.449 ± 0.045*	0.359 ± 0.072¶
	10Gy (N=6)	0.403 ± 0.091	0.509 ± 0.088*	0.533 ± 0.109*§†
K_{trans}	No RT (N=6,6,4)	0.448 ± 0.129	0.328 ± 0.155	0.308 ± 0.13
	2Gy (N=7,7,6)	0.543 ± 0.295	1.038 ± 0.302**	0.496 ± 0.167¶
	10Gy (N=6)	0.614 ± 0.22	1.746 ± 0.388**§†	1.336 ± 0.214**§§†
K_{ep}	No RT (N=6,6,4)	1.27 ± 0.27	1.05 ± 0.52	0.82 ± 0.27
	2Gy (N=7,7,6)	1.56 ± 0.56	2.31 ± 0.63*	1.37 ± 0.4
	10Gy (N=6)	1.55 ± 0.49	3.54 ± 1.09*†	2.62 ± 0.77*§
Vessel Density (mm^{-2})	No RT (N=6,6,4)	400 ± 42	380 ± 30	381 ± 43
	2Gy (N=6)	409 ± 47	380 ± 39	365 ± 57
	10Gy (N=6)	432 ± 30	337 ± 53*†	275 ± 36*§††
Mean Vessel Diameter (µm)	No RT (N=6,6,4)	10.3 ± 1	10.5 ± 1.6	11.3 ± 2.6
	2Gy (N=6)	10.7 ± 1.3	14.7 ± 1.5*†	13 ± 2.7
	10Gy (N=6)	9.4 ± 1.9	16 ± 1.9**††	20.2 ± 2.5*§††¶
Single-vessel Bloodflow (µm/s)	No RT (N=6,6,3)	1299 ± 257	1259 ± 377	895 ± 459
	2Gy (N=6)	1231 ± 70	2312 ± 405*†	1852 ± 584
	10Gy (N=6)	1420 ± 281	2096 ± 295*†	2503 ± 536*††

Table 3-3: The imaging parameters for mice bearing AML during treatment

#-PB samples were not taken in mice bearing ALL after RT as an appropriate number of cells could not be obtained from the maximum sampled blood volume
†-Significantly different from pretreatment time-point P<0.05
¶-Significantly different from 2 days post-treatment time-point P<0.05
* -Significantly different from no RT group P<0.05

§-significantly different from 2Gy treatment group P<0.05
††-Significantly different from pretreatment time-point P<0.001
¶¶-Significantly different from 2 days post-treatment time-point P<0.001
**-Significantly different from no RT group P<0.001
§§-Significantly different from 2Gy treatment group P<0.001

ALL Low Disease Burden		Pretreatment Mean ± Standard Deviation	Day 2 Post-treatment Mean ± Standard Deviation	Day 5 Post-treatment Mean ± Standard Deviation
% ALL in PB	No RT (N=9)	5.5 ± 3.3	24.0 ± 9.8††	30.0 ± 8.4††
	2Gy (N=7)	7.6 ± 4.3	#	#
	10Gy (N=7)	6.6 ± 3.5	#	#
WIS_{tissue}	No RT (N=7)	3347 ± 1986	1860 ± 895	1928 ± 1280
	2Gy (N=6)	2797 ± 843	6706 ± 1469**††	2244 ± 1528¶¶
	10Gy (N=6)	2825 ± 1042	7956 ± 1285**†	6472 ± 2465*§†
WIS_{whole}	No RT (N=7)	6960 ± 3423	3820 ± 2271	3057 ± 2476†
	2Gy (N=6)	5849 ± 2067	11518 ± 3019*††	3729 ± 2752¶¶
	10Gy (N=6)	4847 ± 1115	12224 ± 2105**†	10047 ± 3358*§†
PH_{tissue}	No RT (N=7)	955 ± 396	848 ± 381	883 ± 505
	2Gy (N=6)	846 ± 407	1577 ± 261*††	783 ± 342¶
	10Gy (N=6)	941 ± 452	2806 ± 527**§††	2299 ± 522*§§†
PH_{whole}	No RT (N=7)	1339 ± 542	1072 ± 486	1011 ± 579
	2Gy (N=6)	1245 ± 511	2188 ± 422*††	937 ± 437¶¶
	10Gy (N=6)	1173 ± 430	3020 ± 406**§††	2548 ± 403**§§††
PH_{blood}	No RT (N=7)	2400 ± 821	1805 ± 597	1530 ± 707†
	2Gy (N=6)	2427 ± 783	3061 ± 423*	1716 ± 803¶
	10Gy (N=6)	2123 ± 408	3267 ± 251**†	2887 ± 525*§
v_{ec}	No RT (N=7)	0.277 ± 0.081	0.289 ± 0.041	0.357 ± 0.066
	2Gy (N=6)	0.229 ± 0.076	0.305 ± 0.024	0.304 ± 0.078†
	10Gy (N=6)	0.278 ± 0.062	0.513 ± 0.061**§§††	0.491 ± 0.083*§†
K_{trans}	No RT (N=7)	0.93 ± 0.247	0.685 ± 0.192	0.609 ± 0.222
	2Gy (N=6)	0.833 ± 0.192	1.983 ± 0.433**†	0.892 ± 0.363¶
	10Gy (N=6)	0.902 ± 0.262	1.444 ± 0.149**†	1.316 ± 0.399*
K_{ep}	No RT (N=7)	3.68 ± 1.51	2.37 ± 0.61	1.69 ± 0.5†¶
	2Gy (N=6)	3.89 ± 1.16	6.6 ± 1.67*†	3.04 ± 1.26¶
	10Gy (N=6)	3.3 ± 0.82	2.85 ± 0.44§†	2.65 ± 0.48*
Vessel Density (mm^{-2})	No RT (N=6)	419 ± 46	456 ± 40	529 ± 64†¶
	2Gy (N=6)	461 ± 69	480 ± 70	481 ± 87
	10Gy (N=6)	457 ± 72	356 ± 59*§†	282 ± 63**§†¶
Mean Vessel Diameter (µm)	No RT (N=6)	12.3 ± 2.1	10.2 ± 1.2	10.2 ± 1.0†
	2Gy (N=6)	11.3 ± 1.5	13.3 ± 1.3*†	9 ± 1.4†¶
	10Gy (N=6)	11.7 ± 1.6	18.6 ± 1.9**§§†	19.8 ± 4.2*§†
Single-vessel Blood flow (µm/s)	No RT (N=6)	1292 ± 453	595 ± 302†	494 ± 242†
	2Gy (N=6)	1340 ± 337	2312 ± 580**†	1367 ± 596*
	10Gy (N=6)	1049 ± 352	2017 ± 668*†	1204 ± 374*

Table 3-4: The imaging parameters for mice bearing ALL at low disease burden during treatment

#-PB samples were not taken in mice bearing ALL after RT as an appropriate number of cells could not be obtained from the maximum sampled blood volume

†-Significantly different from pretreatment time-point P<0.05

¶-Significantly different from 2 days post-treatment time-point P<0.05

* -Significantly different from no RT group P<0.05
§-significantly different from 2Gy treatment group P<0.05
††-Significantly different from pretreatment time-point P<0.001
¶¶-Significantly different from 2 days post-treatment time-point P<0.001
**-Significantly different from no RT group P<0.001
§§-Significantly different from 2Gy treatment group P<0.001

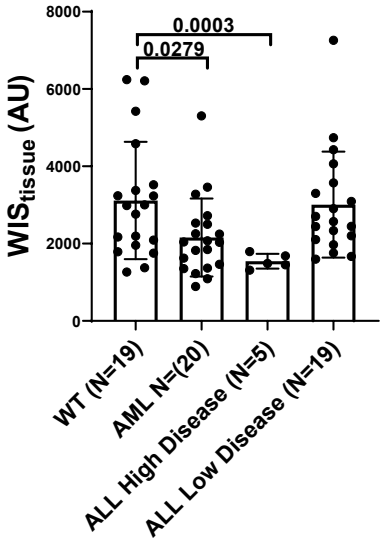

Figure 3-11: The pretreatment values for WIS_{tissue} in WT mice, mice bearing AML, mice bearing ALL at high disease burden, and mice bearing ALL at low disease burden from tables Table 3-2, 3-3, 3-5, and 3-4 respectively.

ALL High Disease Burden (N=5)	Pretreatment Mean ± Standard Deviation	2 days post 10Gy TBI Mean ± Standard Deviation	Paired t-test P value
% ALL in PB	41.4 ±9.2	#	#
WIS_{tissue}	1546 ± 192	5056 ± 1626	**0.0091**
WIS_{whole}	2661 ± 363	7202 ± 2078	**0.0054**
PH_{tissue}	872 ± 263	2295 ± 670	**0.0041**
PH_{whole}	1033 ± 332	2398 ± 626	**0.0028**
PH_{blood}	1365 ± 387	2491 ± 602	**0.0029**
v_{ec}	0.387 ± 0.017	0.550 ± 0.091	**0.0245**
K_{trans}	0.759 ± 0.315	1.241 ± 0.365	0.0698
K_{ep}	1.95 ± 0.77	2.25 ± 0.51	0.3627
Single-vessel Blood flow (μm/s)	1045 ± 74	2217 ± 361	**0.0010**

Table 3-5: The imaging parameters for mice bearing ALL with high disease burden before and 2 days post treatment
#-PB samples were not taken in mice bearing ALL after RT as an appropriate number of cells could not be obtained from the maximum sampled blood volume

Changes in local disease burden, vascular morphology and vascular leakage of Qtracker 655 blood pool agent extravascular accumulation could be clearly observed in large tiled images of the calvarium (Figure 3-12).

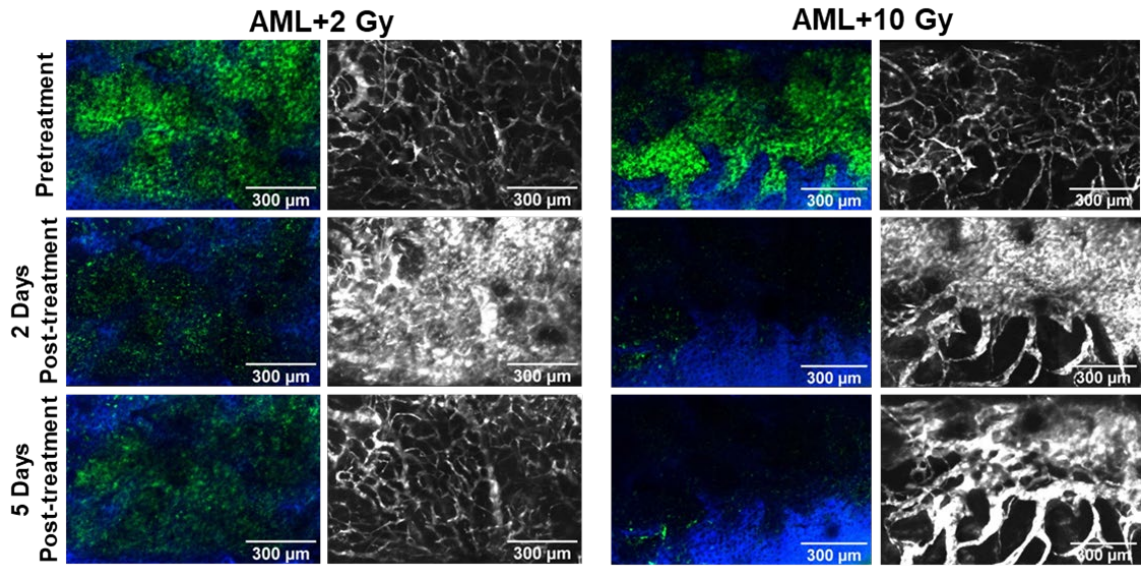

Figure 3-12: Left: images of AML (Green) and second harmonic generation from the collagen in the bone (blue); right: maximum intensity projections of QtrackerTM 655 vascular label (white). Images of 2 Gy and 10 Gy TBI are shown depicting substantial vascular leakage and reduction in AML burden 2 days after TBI.

We observed increases in mean vessel diameter, for all mice 2 days after 2 Gy and 10 Gy TBI as well as 5 days after 10 Gy TBI compared to that in pretreatment time-points and untreated mice. For mice bearing AML or ALL, we observed increases in single-vessel blood flow 2 days after 2 Gy TBI and 10 Gy TBI compared to levels in pretreatment time-points and untreated mice. Compared to untreated mice, increases in single-vessel blood flow were observed 5 days after 10 Gy TBI treatments for mice bearing leukemia. We observed decreases in vessel density 2 days after 10 Gy TBI for mice bearing leukemia, compared to that in pretreatment time-points and, for mice bearing ALL, untreated mice. Decreases in vessel density were also observed 5 days after 10 Gy TBI for all mice, compared to levels in pretreatment time-points and

untreated mice. Decreases in vessel density and increases in vessel diameter were also observed 5 days after 10 Gy TBI compared to 2 Gy for all mice (Figure 3-13). We observed similar trends between femur histology, calvarium histology, and L-QMPM imaging of the BMV for vessel diameter and vessel density measurements (Figure 3-14).

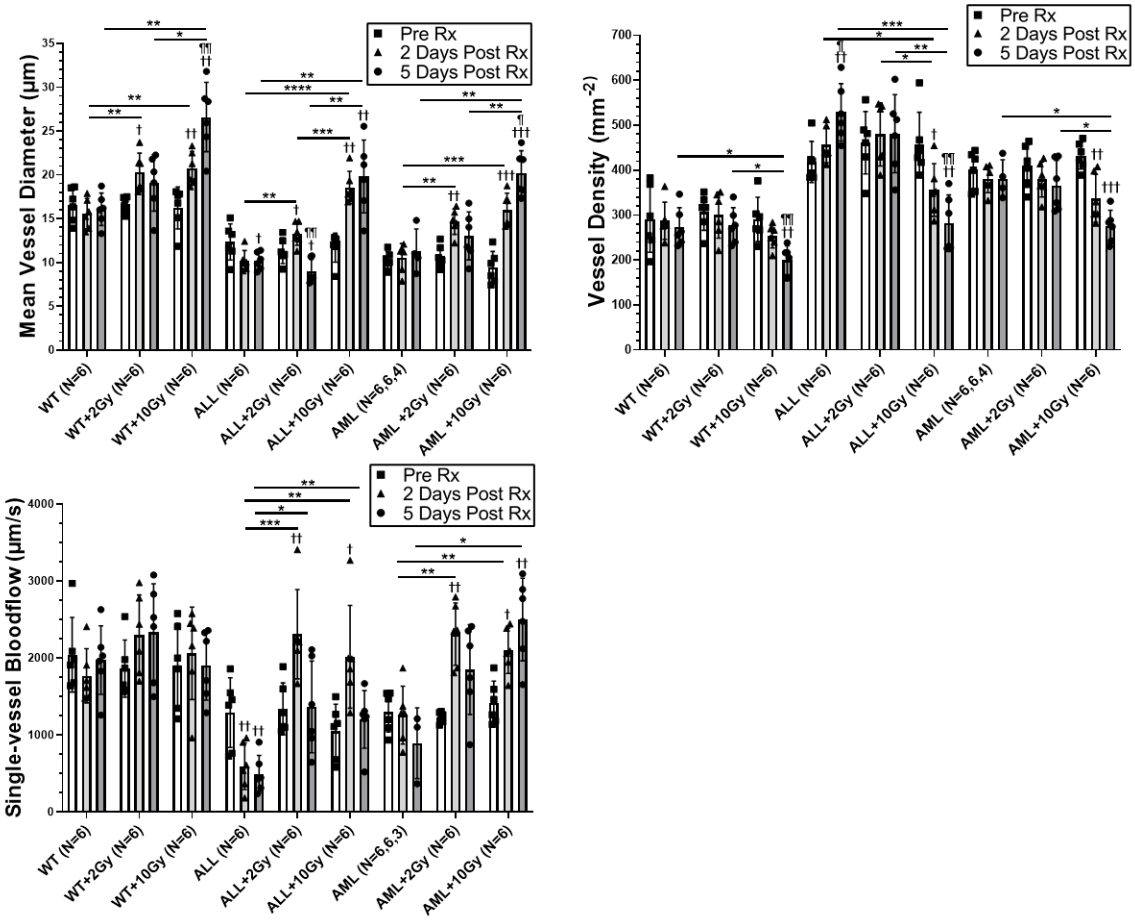

Figure 3-13: The effects of TBI on mean vessel diameter, vessel density, and single-vessel blood flow for WT mice, and mice bearing ALL and AML (∗P < .05, ∗∗P < .01, ∗∗∗P < .001, ∗∗∗∗P < .0001, compared to pretreatment time-point: †P < .05, ††P < .01, †††P < .001, ††††P < .0001, compared to 2 days post-treatment time-point: ¶P < .05, ¶¶P < .01, ¶¶¶P < .001, ¶¶¶¶P < .0001).

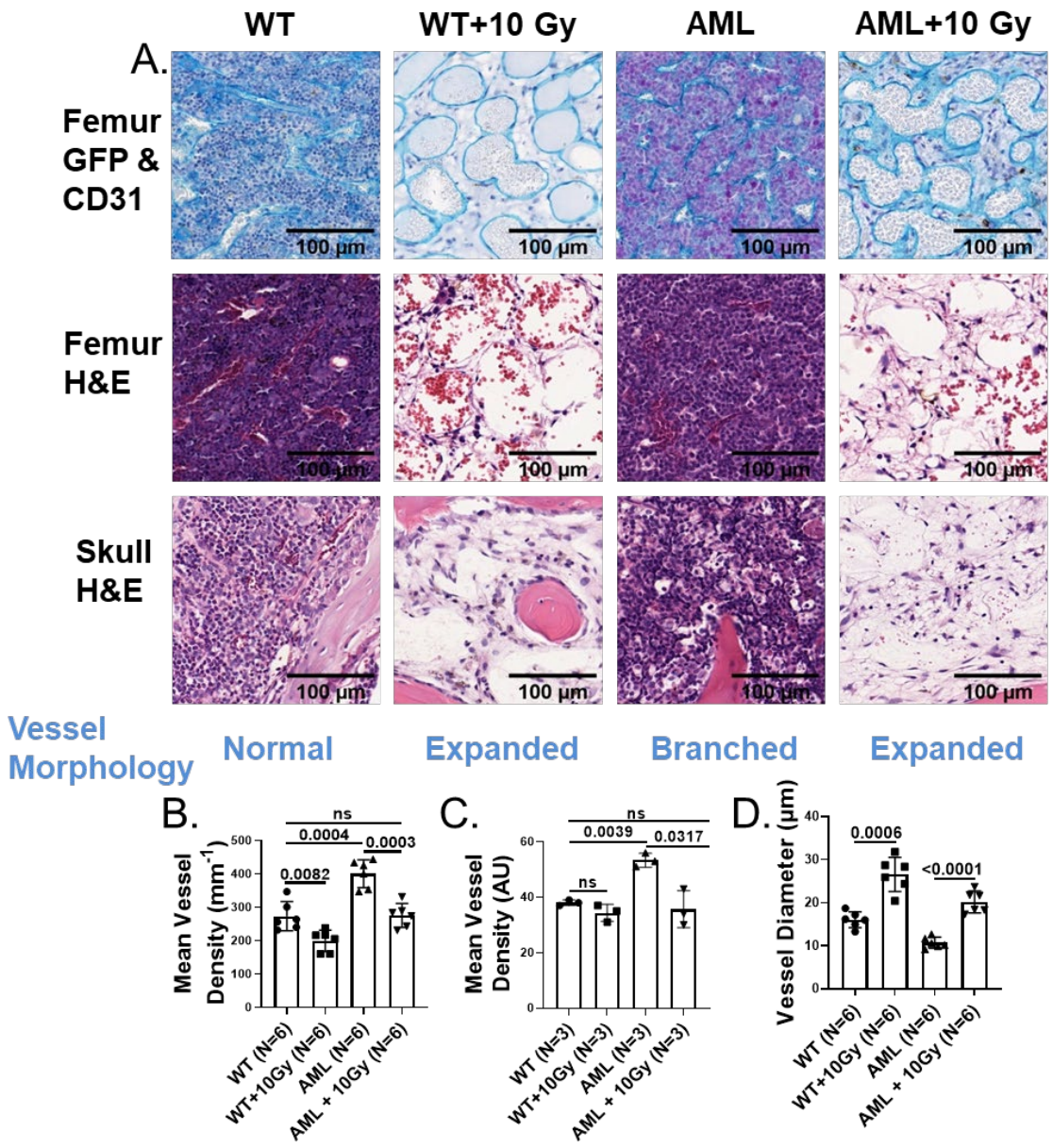

Figure 3-14: (A) Top: Femur histology sections stained for GFP+ AML cells (purple) and CD31 endothelial cells (blue) (top); middle: femur hematoxylin and eosin stained sections (middle); bottom: skull stained for hematoxylin and eosin sections (bottom). Vessel dilation was observed 5 days after 10Gy TBI for WT mice and mice bearing AML. (B) Mean vessel density measurements from L-QMPM imaging of mice with matching conditions to histology. (C) Vessel density scoring of individual vessels in CD31+ endothelial stained femur sections. Two different image locations were used for vessel scoring. (D) Vessel diameter measurements from L-QMPM imaging of mice with matching treatment conditions to histology.

3.3.4 RT increased drug delivery potential to the healthy and leukemic bone marrow

We observed increases in WIS_{tissue} for all mice 2 days after both 2 Gy and 10 Gy TBI compared to either pretreatment time-points, or untreated mice (Figure 3-15). Percent increases in WIS_{tissue} mean values ranged from 39% to 81% for WT mice and 139% to 227% for mice bearing leukemia compared to pretreatment. Similar increases post-treatment for K_{trans} and K_{ep} were observed. We observed increases in WIS_{tissue} 5 days after 10 Gy TBI for mice bearing leukemia compared to untreated mice, and, for mice bearing ALL, pretreatment time-points. We additionally observed significant increases in WIS_{tissue} 5 days after 10 Gy TBI compared to 2Gy for mice bearing AML or ALL (mean percent increases of 165% and 188%, respectively). We found significant decreases in WIS_{tissue} prior to treatment intervention in mice bearing AML or mice bearing ALL treated with 10 Gy at high disease burden compared to WT mice (P=0.0279 and 0.0003, respectively), demonstrating that increases in WIS_{tissue} after TBI occurred in healthy or leukemic bone marrow microenvironments (Figure 3-16). We observed increases in PH_{tissue} and v_{ec} after TBI at a variety of doses and time-points likely due to changes in cellularity (Table 3-2, 3-3, 3-4, & 3-5). Similar results are observed in DCE imaging [52].

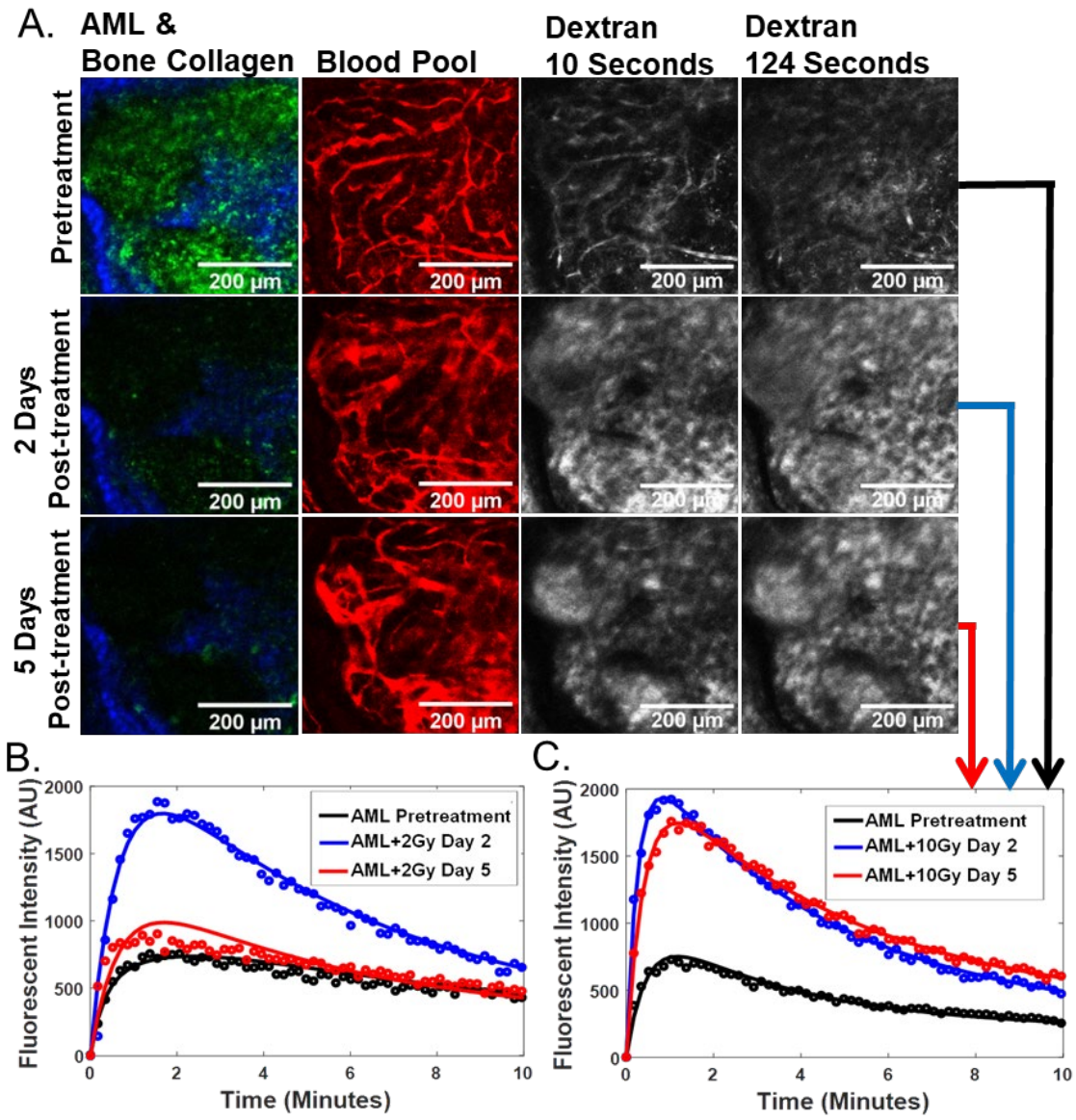

Figure 3-15: Images of AML (green) and second harmonic generation from the collagen in the bone (blue) (far left). Images of Qtracker™ 655 vascular label (red) (left middle). Images of dextran (white) from the first frame after injection of dextran (right middle). Images of dextran (white) from the 12th frame after dextran injection (far right). A dose of 10 Gy TBI was given to the imaged mouse. Below the images, plots of fluorescent intensity values from the extravascular tissue ROI taken from time-lapsed images of dextran from 2 separate mice treated with either 10Gy or 2 Gy TBI are shown. The plotted data from the mouse receiving 10Gy matches the images above. Solid lines indicate the extravascular fitting function for compartment modeling.

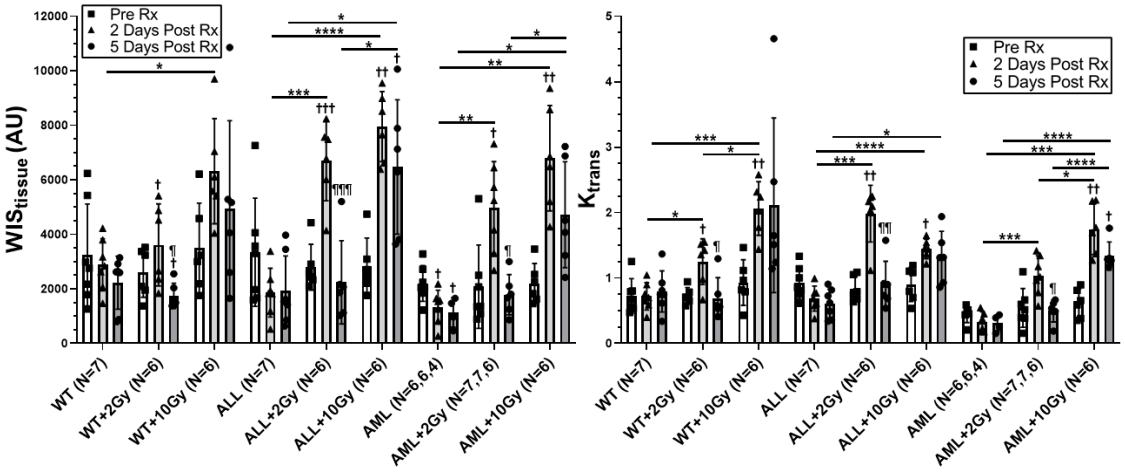

Figure 3-16: The effects of TBI on WIS_{tissue}, and K_{trans} for WT mice and mice bearing ALL or AML. (∗P < .05, ∗∗P < .01, ∗∗∗P < .001, ∗∗∗∗P < .0001, compared to pretreatment time-point: †P < .05, ††P < .01, †††P < .001, ††††P < .0001, compared to 2 days post-treatment time-point ¶P < .05, ¶¶P < .01, ¶¶¶P < .001, ¶¶¶¶P < .0001 Tukey's post hoc comparison)

A summary of the effects of TBI is shown in Figure 3-17. We found positive linear correlations with WIS_{tissue} for K_{trans}, K_{ep}, v_{ec}, single-vessel blood flow, and mean vessel diameter, while no correlation was found for vessel density (Figure 3-18).

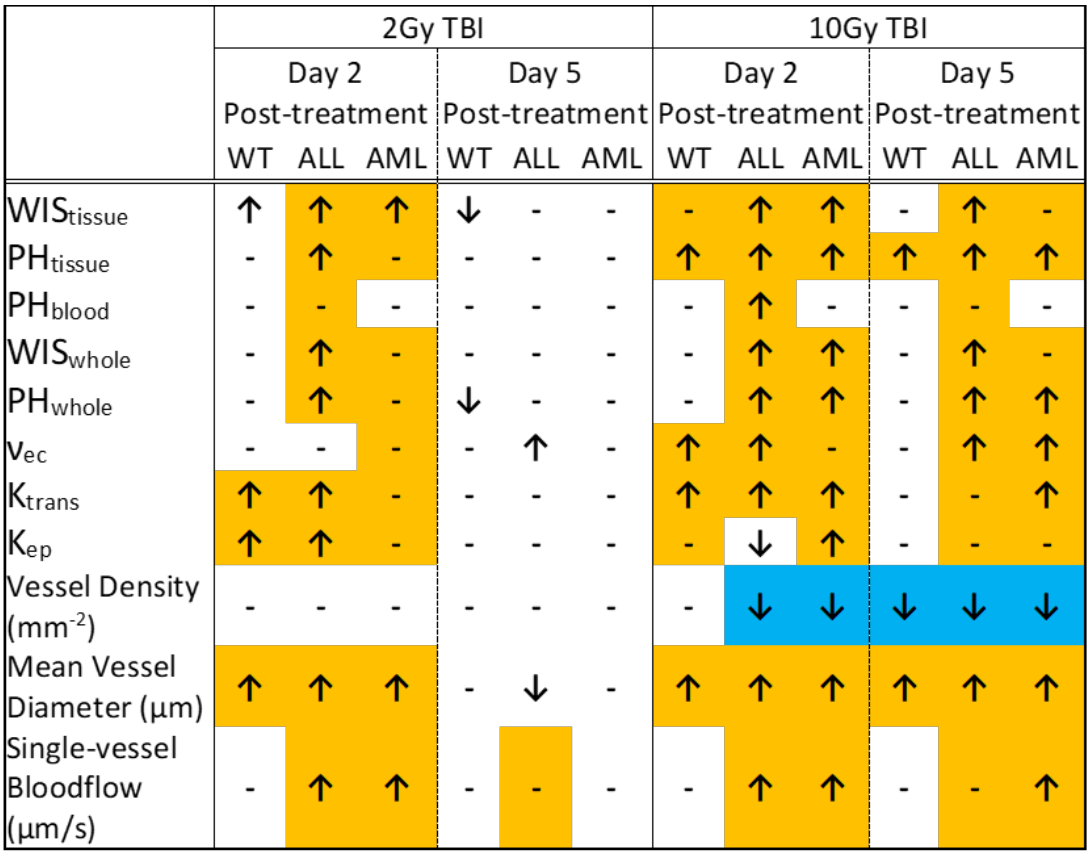

Figure 3-17: A summary of the response of WT mice, and mice bearing ALL and AML to 2 Gy and 10 Gy TBI treatments. Arrows indicate a significant increase or decrease compared to pretreatment time-points, orange indicates a significant increase compared to the untreated group, and blue indicates a decrease compared to the untreated group (P=0.05 for all).

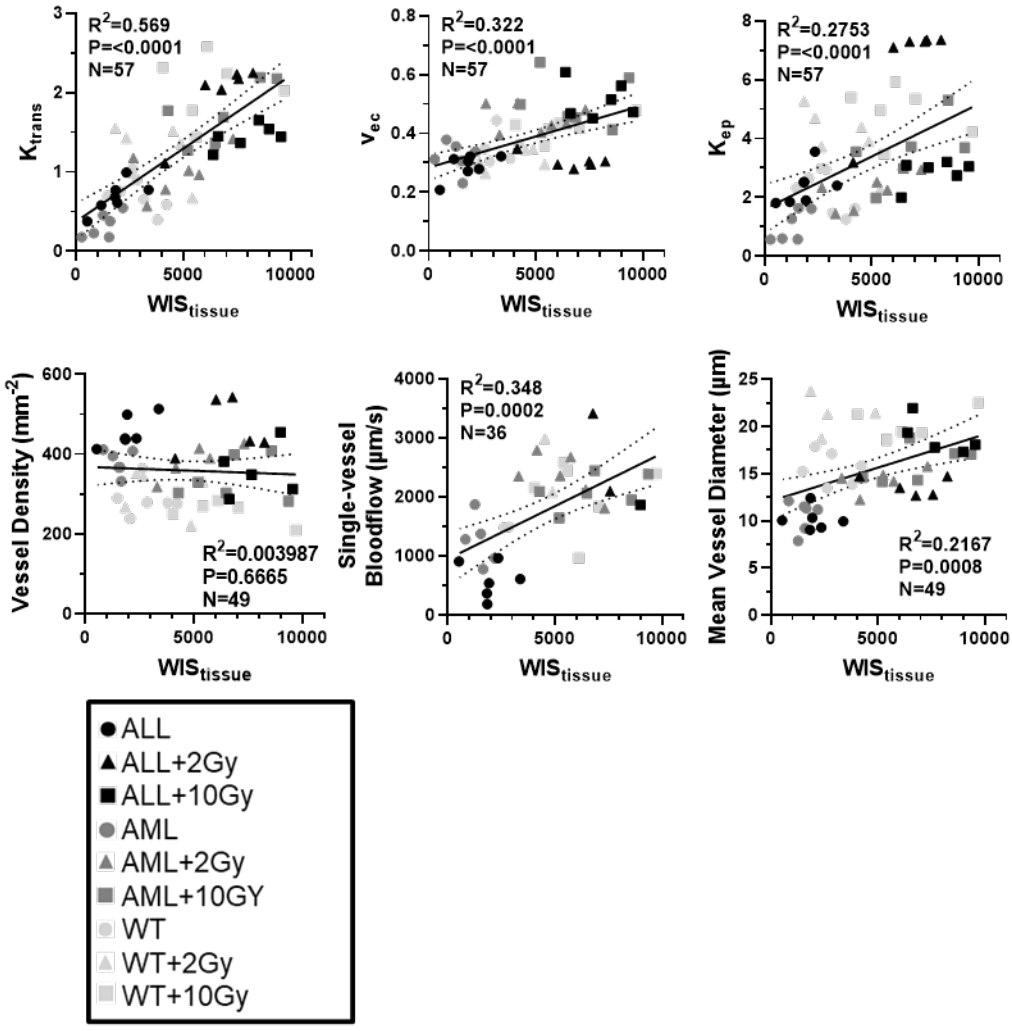

Figure 3-18: Linear correlation plots for various L-QMPM imaging parameters plotted with data from the time-point 2 days after TBI treatments. A single image time-point was used per mouse for linear correlation calculations.

3.4 Discussion

We developed L-QMPM imaging to measure several parameters that quantified the BMV and drug delivery potential before and after RT. Decreased WIS_{tissue}, WIS_{whole}, PH_{whole}, K_{ep}, single-vessel blood flow and mean vessel diameter, as well as increased vessel density and v_{ec} were observed with the onset of leukemia. WIS_{whole} was the most effective contrast-based, time-lapsed imaging parameter to identify mice bearing leukemia. As hypothesized, 2 Gy and 10 Gy TBI treatments increased WIS_{tissue}, K_{trans},

and mean vessel diameter in WT mice and mice bearing leukemia 2 days after TBI. We also observed increased single-vessel blood flow for mice bearing AML and ALL. Changes in BMV morphology and function were observed 5 days after 10 Gy TBI, while 2 Gy caused minimal changes. Linear correlations between WIS_{tissue} and vessel diameter, single-vessel blood flow, K_{trans}, v_{ec} and K_{ep} were found, while vessel density was not correlated with WIS_{tissue}.

DCE imaging analysis applies mathematical models to or infers the BMV changes that influence the delivery of contrast agents. We calculated WIS_{whole} and PH_{whole} as measurements commonly interpreted as the volumetric tissue blood flow rate, and tissue blood volume for DCE imaging [42]. Several studies using DCE imaging identified changes in PH_{whole} or similar mathematically modeled parameters to be positively correlated with vessel density and have proposed DCE imaging as an alternative method to quantify vessel density in the untreated malignant bone marrow [53, 97]. This circumstance is desirable as it would reduce the need for invasive bone marrow biopsies to quantify vessel density, which is a prognostic marker for tumor aggressiveness [98]. However, in this work, we found no correlation between PH_{whole} and vessel density with leukemia onset likely due to the reduction in mean vessel diameter present in mice bearing leukemia. Additionally, over half of the fluorescent signal contributing to PH_{whole} was from the extravascular ROI, suggesting that PH_{whole} measurements may be significantly influenced by leakage of contrast into the extravascular tissue. Our results demonstrate that positive correlations of PH_{whole} with vessel density or vessel volume cannot be assumed without pathological validation, and that mathematical modeling should be used to account for signal contributions from the extravascular tissue when quantifying vascular parameters using DCE.

We identified WIS_{whole} as the most effective time-lapsed imaging measurement to identify mice bearing leukemia. As WIS_{whole} is primarily a measurement of volumetric blood flow, it will be closely related to mean vessel diameter, vessel density, and single-vessel blood flow, which are all affected early in leukemia progression. This enables WIS_{whole} to better identify mice bearing leukemia than other contrast-based time-lapsed imaging parameters, which are less sensitive to early vascular alterations.

Because WIS_{whole} is primarily a measurement of volumetric blood flow, it is enticing to infer improved drug delivery potential when increases in WIS_{whole} are observed. However, we observed that changes in WIS_{whole} and WIS_{tissue} did not occur at the same disease burden. Additionally, changes in WIS_{tissue} were observed in WT mice after TBI, but no changes were observed in WIS_{whole}. Our results demonstrated that WIS_{whole} may not accurately identify changes in drug delivery potential, likely because WIS_{whole} is a convolution of signals from vascular and extravascular tissues. These observations identified the importance of validating drug delivery potential when changes in DCE imaging parameters are observed.

Increases in WIS_{tissue} 2 days after TBI in WT mice were accompanied only by increases in K_{trans} and mean vessel diameter, suggesting that increases in WIS_{tissue} were due to increased vascular permeability or increases in vascular surface area, which commonly influence K_{trans} [48]. Similar alterations in K_{trans} after TBI have been observed previously using DCE-MRI [52]. For mice bearing leukemia, increases in blood flow after TBI may also contribute to increased WIS_{tissue}. Similar observations of improved tissue drug perfusion after RT have been made in solid tumor models [27, 28], suggesting that the leukemic BMV and solid tumor vasculature may have similar responses to RT. These results suggest that increased WIS_{tissue} may be found shortly after a variety of TBI

doses, and directly demonstrate the role of the BMV in contributing to improved cellular chemotherapy uptake after LDRT that is identified in Chapter 2.

Although we observed similar changes in WIS_{tissue} 2 days after 2 Gy and 10 Gy TBI, the duration of the changes was different. These finding suggests that the window of opportunity for synergistic combination therapy with therapeutics after reduced-intensity TBI regimens may be smaller than with standard myeloablative regimens of TBI [99]. We observed significant changes in vessel density and vessel diameter 5 days after 10 Gy TBI compared to 2 days, while no significant differences were noticed in WIS_{tissue}. These data suggest that maximum BMV morphological changes after TBI may occur later than the maximum increases in WIS_{tissue}. These findings are in agreement with other studies observing vasodilation and macromolecular contrast leakage 4-7 days after myeloablative doses [100, 101]. Future studies should identify how long-term vascular damage after myeloablative TBI and bone marrow transplantation influence drug delivery potential.

We observed decreases in vessel density 2 days after 10 Gy treatment for mice bearing leukemia, but not for WT mice, suggesting that the leukemic BMV may have increased radiosensitivity. Newly formed immature vessels have been shown to be sensitive to RT [102, 103] and more mature vascular structures have been found after fractionated RT in solid tumors [104]. This suggests that the appropriate RT treatment may be able to preserve mature vessels, while eliminating newly formed vessels present from leukemia signaling. Synergistic effects have been observed with RT and vascular based therapeutic agents for solid tumors [105], making combination therapy an attractive option for the treatment of leukemia. Future studies employing dose fractionation need to be performed to understand how RT can be used to normalize the

vascular system, and whether enhancements to drug delivery potential are observed after successive fractions of LDRT.

Although L-QMPM is useful to accurately assess drug delivery potential, it is limited to preclinical models, making DCE imaging modalities such as MRI or CT necessary for clinical translation. In this work, we provide direct observations of BMV morphology and function, as well as measurements used in DCE imaging. These observations will be invaluable for interpretation of DCE imaging of the bone marrow.

3.5 Conclusion

We identified WIS_{whole} as the most effective parameter to distinguish between WT mice and mice bearing AML or ALL. This suggests that DCE imaging should focus on the rate of initial increase in whole tissue contrast signal during time-lapsed imaging as a biomarker for leukemia. Our results show that the response of the leukemic BMV to neo-adjuvant RT improves drug delivery to the bone marrow by improving blood flow and increasing drug permeation through the BMV to the extravascular tissue.

Chapter 4: In vivo assessment of the tumor vascular response to radiotherapy using a macroscopic dynamic fluorescent contrast enhanced imaging system

This chapter is based largely on the following published work:

4.2 Introduction

Stereotactic body radiotherapy treatment (SBRT) uses a reduced number of treatment fractions at higher doses (hypofractionation), typically 10-20 Gy/fraction to treat solid tumors. Compared to conventional fractionation, hypofractionation has significantly decreased the relative risk of local tumor progression for patients with squamous, non-small cell lung cancer resulting in a 27% reduction in relative risk of local progression [106]. Additionally, SBRT has been shown to be tolerable and effective in patients for a variety of solid tumor cancers [107]. There has recently been much debate over whether the traditional linear quadratic model, which assumes cell death arises from direct ionizing radiation based DNA damage, adequately accounts for the success

of SBRT or whether tumor vascular damage contributes to indirect tumor cell death through a loss of blood supply to the tumor [108-111]. Histological evaluations have provided evidence for extensive vascular damage following SBRT treatment, however histology is unable to perform non-invasive longitudinal assessments directly measuring blood flow. Since tumor recurrence with SBRT is still a common problem, longitudinal assessments of blood flow would be desirable because they would allow for direct correlation between tumor vascular response (TVR) and treatment outcome over time. Additionally, while the evaluation of the whole tumor is needed due to vascular heterogeneity, it is time consuming when analyzed by histology. Fast, whole-tumor, non-invasive techniques that allow for whole tumor measurements of vascular function would be able to correlate TVR to treatment response. This would enable TVR to be investigated as a prognostic factor for treatment outcome in SBRT and enable a better understanding of the role of TVR in SBRT tumor control.

Initial work using intravital multiphoton microscopy by the author has observed large amounts of vascular heterogeneity in solid tumor models (Figure 4-1)[112]. While QMPM can simultaneously perform DCE imaging and observe single-vessel characteristics during radiotherapy, it typically requires invasive surgery and is only able to image a small region of tissue during DCE imaging (approximately 0.5 mm x 0.5 mm). Since the vascular distribution in solid tumor malignancies is highly heterogenous, similar fluorescent imaging techniques capable of observing contrast uptake and clearance over the entire tumor structure before and after radiotherapy would be desirable to ensure that results from the small regions imaged with QMPM are representative of the entire tumor.

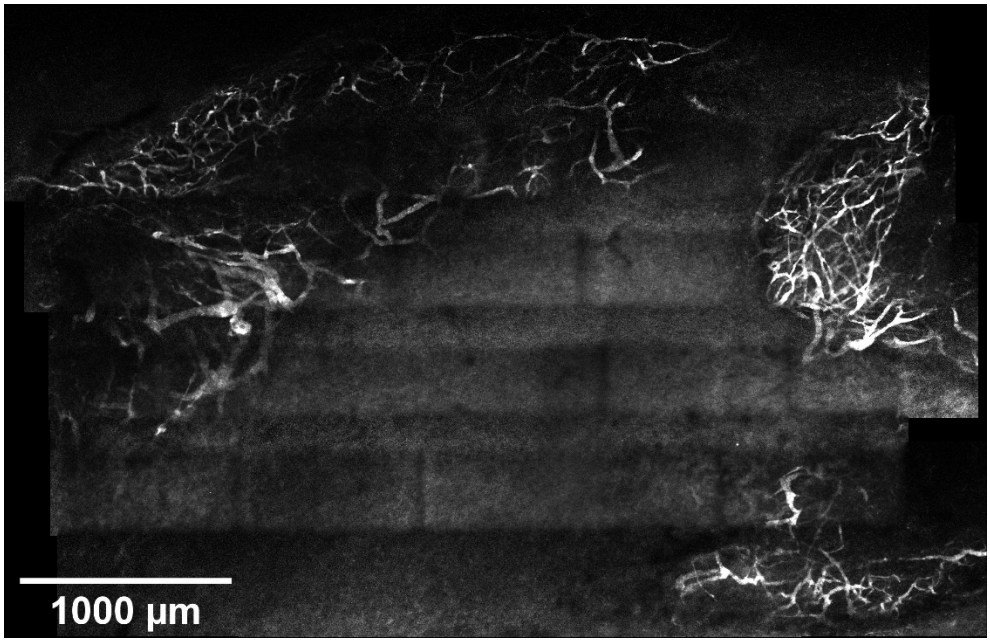

Figure 4-1: Large set of 5 by 6 tiled images showing the vascular heterogeneity in an E0771 breast cancer tumor during live intra-vital imaging of a NOD/SCID mouse. The mouse was anesthetized, injected with 70kDa fluorescent dextran, and surgery was performed to expose the tumor for imaging using a 10x microscope objective with a Prairie Ultima multiphoton microscope. The tumor Vasculature is located at the periphery of the tumor with the center showing minimal functional vasculature.

One such technique that is well suited to obtain whole tumor measurements of blood flow is macroscopic near-infrared dynamic fluorescence imaging (DynFI) [113-115]. DynFI is based on time-series analysis of a given fluorescent probe's pharmacokinetics and can be used to accurately and quantitatively measure functional parameters such as blood flow and vascular permeability for many clinical and preclinical applications [116-121]. A fluorescent agent commonly used for DynFI is indocyanine green (ICG). After injection, ICG rapidly binds to albumin making the kinetics of ICG fully governed by the temporal dynamics of albumin in vivo [122]. Using the FDA approved near-Infrared fluorescent agent ICG, DynFI has been used to characterize blood flow and vascular permeability in solid tumors making it suitable for monitoring TVR in SBRT tumor treatments [123, 124].

Acquiring spatiotemporal DynFI data using CCD camera-based systems typically yields extremely large data sets (i.e., number of pixels x dynamic time points) that require time consuming analysis. This hampers the practical application of this technique [125]. Analysis time can often be shortened by temporal or spatial dimension reduction. Typically, temporal dimension reduction is achieved through extraction of important temporal features (blood flow index, perfusion rate, mean transit time, etc.) that characterize pharmacokinetics [119]. However, the use of these temporal features is limited by their susceptibility to noise and motion artifacts [121]. Spatial dimension reduction of DynFI data is usually achieved by averaging DynFI signals within the tumor region, discarding any spatial information and ignoring vascular heterogeneity. One way to quickly assess the entire DynFI spatiotemporal data while preserving spatial information is to perform by using principal component analysis (PCA) [121, 125-129]. Analysis using PCA can be performed using pharmacokinetics of a wide variety of imaging agents in many tissues. PCA enables a rapid automated analysis of longitudinal data to quantitatively measure TVR, while still preserving spatial information.

In this chapter, I describe a first-of-its-kind theranostic CCD-based DynFI/microCT-guided targeted irradiator that longitudinally assesses TVR to SBRT treatments in tumor bearing mice. A rapid, automated data analysis method using PCA of the spatiotemporal data is used to extract pharmacokinetic information of ICG. Differences in the first and second principal component feature (PC1 & PC2) of ICG pharmacokinetics were found in tumors immediately before and two days after 10 Gy SBRT. The dose of 10 Gy was chosen as early changes in tumor vasculature have been seen at a wide range of doses (5-20 Gy/fraction) [11, 130]. Pretreatment and posttreatment data were plotted as a scatterplot in PC1-PC2 space and a classification algorithm based on a 99.9% confidence covariance ellipse was used to identify

responding (TVR_{pos}) and non-responding (TVR_{neg}) tumor pixels for rapid spatial mapping of tumor heterogeneity. Results demonstrate the ability of the theranostic system to both observe changes in ICG pharmacokinetics and perform fast, automated assessments of vascular response to SBRT.

4.3 Materials and Methods

4.3.1 Animal and tumor model

Four 10-15 week old C57/B6 mice (Strain 000664, The Jackson Laboratory) were subcutaneously injected in the right thigh muscle with aggressive murine oral cavity cancer, MOC2 cells ($1x10^5$ cells) [131] suspended in phosphate buffered saline (100 µl). Mice were injected 21 days before the start of imaging and treatment. Before imaging, the hair on the thighs and backs of the mice was removed using hair depilatory cream (Church & Dwight Company). During the treatment and imaging sessions, mice were anesthetized initially with 3% isoflurane mixed with O_2 at a flow rate of 2 L/min, then maintained with 1.5% isoflurane at an O_2 flow rate of 1.5 L/min. For imaging, an intravenous catheter was inserted into the tail vein to administer ICG (4.7 µg, approximately 0.19 mg/kg) suspended in saline (75 µl) during image acquisition. Pretreatment imaging was acquired just prior to radiation treatments. All mice fully recovered after the imaging procedure. Tumors volumes were measured by calipers before and two days after treatment. Tumor volume was calculated using the formula $volume=length*width^2/2$. All animal experiments were performed according to City of Hope guidelines and approved by the Institutional Animal Care and Use Committee.

4.3.2 MicroCT image acquisition and SBRT treatment

The X-ray irradiation was performed using the preclinical X-ray microCT image-guided radiation therapy platform (X-RAD SmART). MicroCT images were acquired (0.1

mm x 0.1 mm) using a low-dose of radiation (<50 cGy). After CT images were acquired, a Monte Carlo-based planning treatment simulation tool was used to establish and deliver the optimal image-guided 10 Gy treatment to the tumor ROI.

4.3.3 Instrumentation and DynFI data acquisition

The theranostic system was built by incorporating a CCD-based fluorescence molecular imaging (FMI) system [132] into a commercial preclinical X-ray CT image-guided radiation therapy platform (X-RAD SmART, Precision X-Ray, Inc.). The FMI system uses a 785 nm laser diode (75 mW, Thorlabs) for ICG excitation. The laser diode mounts and drivers were integrated into the system gantry. The drivers were operated in constant power mode to ensure output stability during the experiments. The laser output was collimated then sent towards an illumination point below the mouse using a galvano-mirror scanner. A cooled CCD camera (Perkin Elmer, Cold Blue) was positioned directly above the mouse to perform transillumination data acquisition. A sigma MACRO 50 mm F2.8 lens was coupled to the CCD camera, providing 2280 pixels x 1528 pixels images. The pixels were binned during acquisition using a factor of 4, resulting in 570 pixels x 382 pixels images with a pixel size of 0.2 mm × 0.2 mm. A computer-controlled filter-wheel (Tofra, Inc.) was installed between the CCD camera body and the lens. Two 830 nm band-pass filters (MK Photonics) were stacked and used to eliminate excitation light at 785 nm. This filter combination was used to minimize the strong excitation leakage with a maximum transmission rate at the fluorophore emission wavelength (830 nm).

A DynFI series of 46 images was acquired with an integration time of 10 seconds per frame. ICG was injected at the start of acquisition of the 5^{th} frame. The four frames acquired before ICG injection were averaged and used as baseline, which was subtracted from the remaining 42 DynFI images. This was used to correct for both the

residual fluorescence signals and the excitation light leakage through the rejection filters (Figure 4-2) [133].

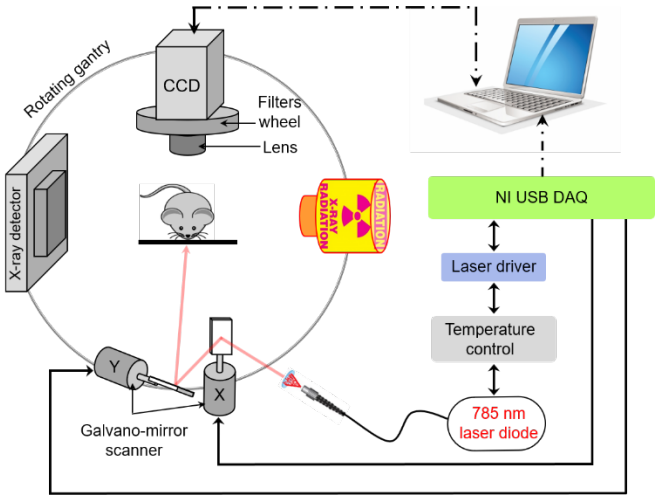

Figure 4-2: Diagram of the theranostic system. The X-ray source is used to both perform CT imaging and high-dose irradiation. For DynFI, a CCD camera is positioned above the mouse while it is illuminated from below using a 785 nm laser and an XY Galvano-mirror scanner. A temperature control unit is used to maintain the laser operating temperature. NI USB DAQ: National Instrument USB data acquisition card. The dashed lines indicate USB connections. © 2020 IEEE

4.3.4 Kinetics features extraction and visualization.

PCA was performed using the "pca" Matlab® function, on the DynFI fluorescence signals within the tumor ROI and kidney ROI. Before quantifying the induced PC variation, the pretreatment and posttreatment pixel PC feature values were normalized by subtracting the mean pretreatment PC feature value for each tumor. An RGB image was made by assigning the normalized PC1 and PC2 feature values to the red channel and blue channels, respectively [125]. The green channel was set to zero. Each of the channels was individually converted to gray scale using the "mat2gray" Matlab® function then normalized to 255. Finally, the ROIs of the resulting PC-RGB image were superimposed on the corresponding gray scale ambient-light images.

4.3.5 Data representation and statistics

The 99.9% confidence covariance ellipse is defined based on the covariance of data. Its two major axes are calculated from the two-dominant data eigenvectors, while their magnitude corresponds to data eigenvalues. The orientation of the ellipse is given by the angle between the major eigenvector and the x-axis.

Significance measurements were calculated using Prism (V.7.01, GraphPad). A p-value of 0.05 or lower was considered significant. For box and whisker plots, boxes represent the 25^{th} and 75^{th} percentile, and error bars indicate the min and max of the data. All paired t-tests are performed using two-sided difference based statistical testing.

4.4 Results

4.4.1 SBRT-induced changes in pharmacokinetics of ICG

To monitor and quantify TVR after high-dose irradiation, we acquired a series of 46 DynFI images before and two days after the irradiation of the tumor. We first analyzed the DynFI images simply using mean dynamic fluorescence signals obtained over the tumor ROI. Tumor ROIs from pre and two days posttreatment imaging were automatically segmented on the respective pre and posttreatment microCT images. The multimodal system is fully integrated enabling fast, accurate, and automated co-registration of DynFI and microCT ROIs.

A delay in both tumor uptake and tumor clearance of ICG two days after SBRT treatment can be observed, while no such delays are observed in the kidney (Figure 4-3). Additionally, the size of tumors did not change during treatment (336.1±152.7 and 320.9±155.7 mm^2, P=0.5971 Paired t-test) suggesting any changes in ICG kinetics were related to tumor biology rather than tumor geometry changes. Post-irradiation tumor ICG kinetics showed a slight delay during the ICG uptake compared to the pre-irradiation

kinetics. However, a considerable delay was seen in the ICG clearance from the tumor. Significant increases in averaged ICG retention was observed in tumors, resulting in a 40.5±16.1% decrease in the exponential decay parameter of ICG after it had reached peak concentration (P=0.0405 Paired t-test n=4). As control, we analyzed the DynFI signal from the left kidney. The kidney ROI was determined by comparison to an open source mouse atlas [134]. No significant variation in the half-life of ICG decay was seen for the kidney ROI. This suggests that changes in ICG dynamics of the tumor after treatment are due to vascular damage with SBRT therapy (Figure 4-3)[10].

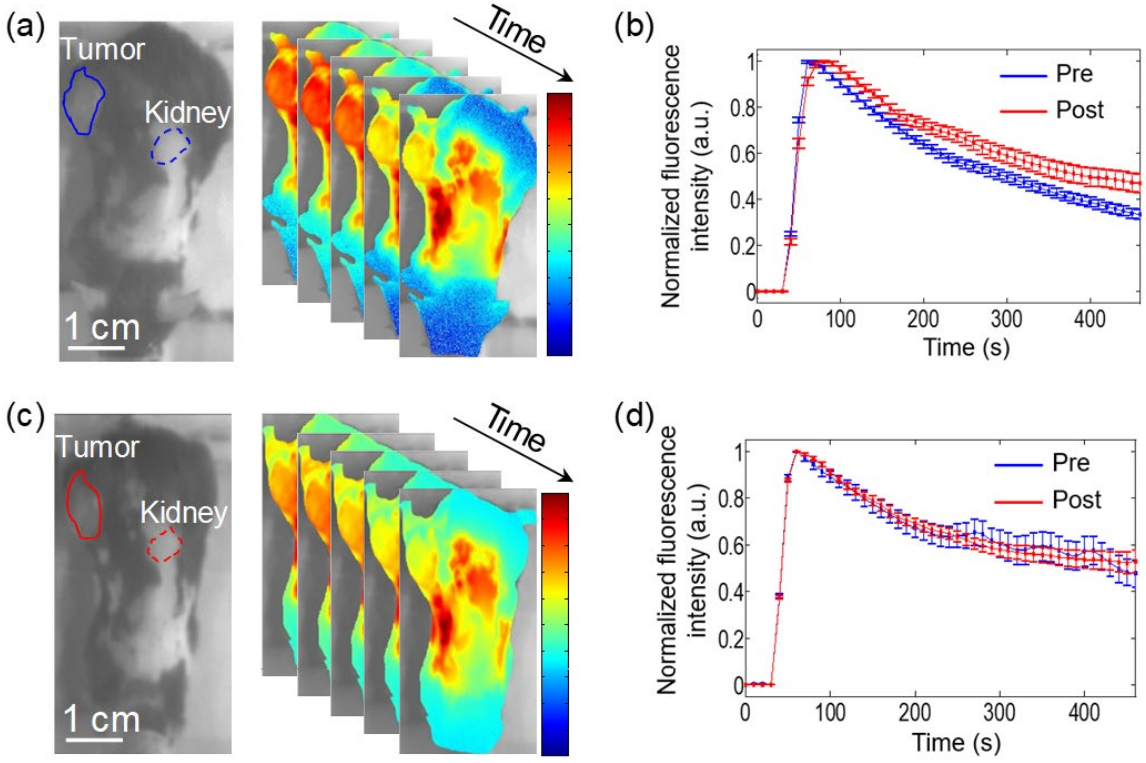

Figure 4-3: Representative ICG Kinetics (a) pretreatment and (c) posttreatment gray scale ambient-light images (left) and DynFI images acquired at 40 s, 60 s, 130 s, 350 s, and 450 s superimposed onto gray scale ambient-light images (right). DynFI images are presented using a logarithmic scale for better visualization. Ambient-light images (left) show the locations of the tumor ROI (solid-line) and the kidney ROI (dashed-line) used for analysis. (b) The plotted mean fluorescence intensity values of DynFI data for (b) the tumor ROI and (d) the kidney ROI for pretreatment (blue) and two days posttreatment (red). Error bars represent standard deviation.

4.4.2 SBRT-induced changes in the principal components

Taking DynFI pixel data, we obtained a simplified spatiotemporal feature representation by PCA analysis. Only the first two projected PC features (PC1 and PC2) were evaluated, as they were shown to be proportional to the area under the kinetic curve and to the exponential decay parameter of ICG, respectively [121]. The additional 44 components were discarded since they were sensitive to image noise and have not been shown to directly represent ICG kinetics [121]. Spatial mapping of the DynFI spatiotemporal pharmacokinetics of ICG using PC space mapping allowed for a straight-forward observation of SBRT-induced TVR (Figure 4-4). A clear change in normalized PC1 and PC2 feature values for the tumor are seen after SBRT treatment, while no change is observed for kidney. Nearly significant and significant differences in mean normalized whole-tumor PC feature values were observed for PC1 (P=0.0559 Paired t-test n=4) and PC2 (P=0.0432 Paired t-test n=4) respectively (Figure 4-5).

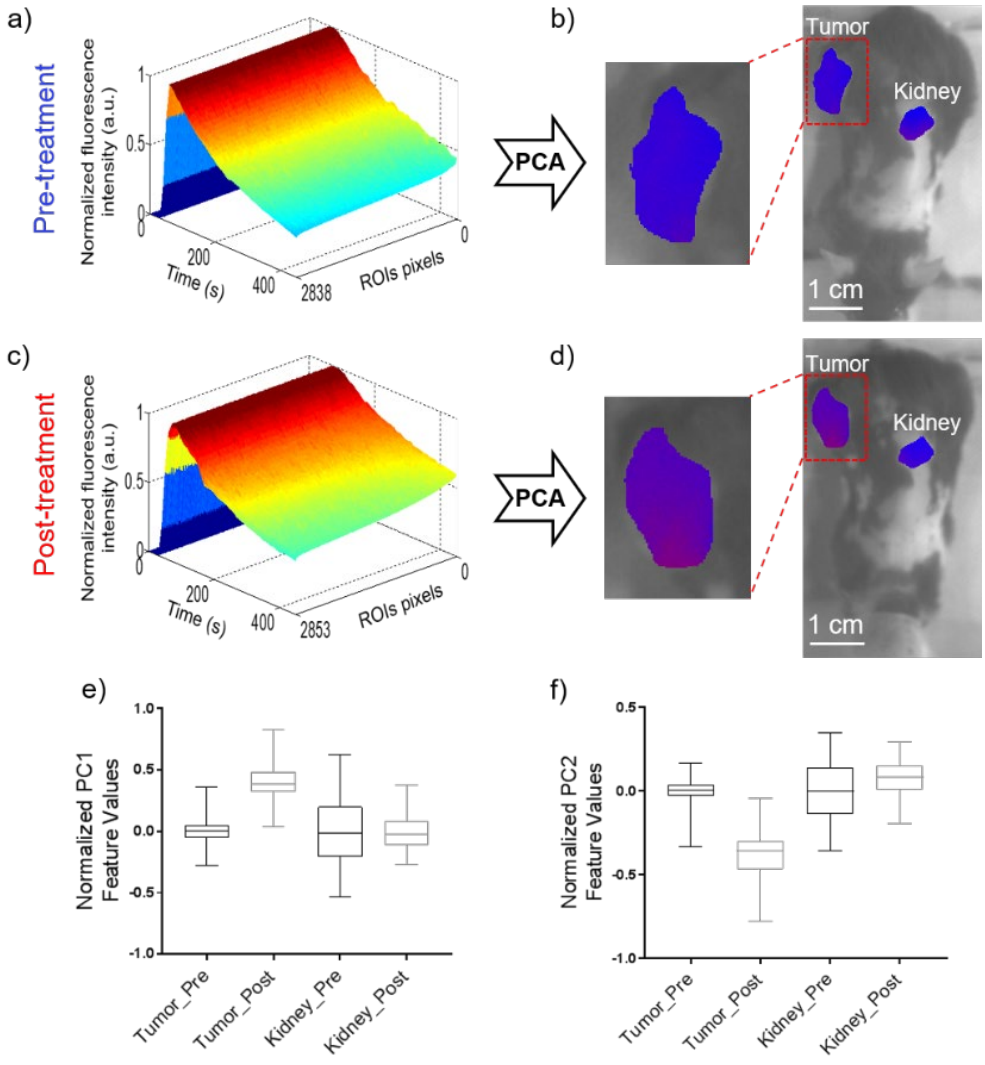

Figure 4-4: PC feature-based analysis of the DynFI data obtained from the mouse shown in Figure 4-3. Normalized time-series of ICG fluorescence intensity for all individual pixels in (a) the pretreatment tumor ROI (2838 pixels) and (c) the two days posttreatment tumor ROI (2853 pixels). PC-RGB images of normalized PC1 and PC2 feature values superimposed on ambient-light images are shown (b) before and (c) two days after 10Gy SBRT treatment. The normalized PC1 and PC2 feature values were assigned to the red and blue channels, respectively. Green intensities were set to zero. A clear change from blue to red can be seen from pretreatment to two days posttreatment, showing TVR. Box and whisker plots of normalized PC feature values for (e) PC1 and (f) PC2 tumor and kidney ROIs from the corresponding pretreatment and two days posttreatment DynFI data. An increase in normalized PC1 feature values and a decrease in normalized PC2 feature values are seen in the tumor posttreatment, while no change is seen for kidney.

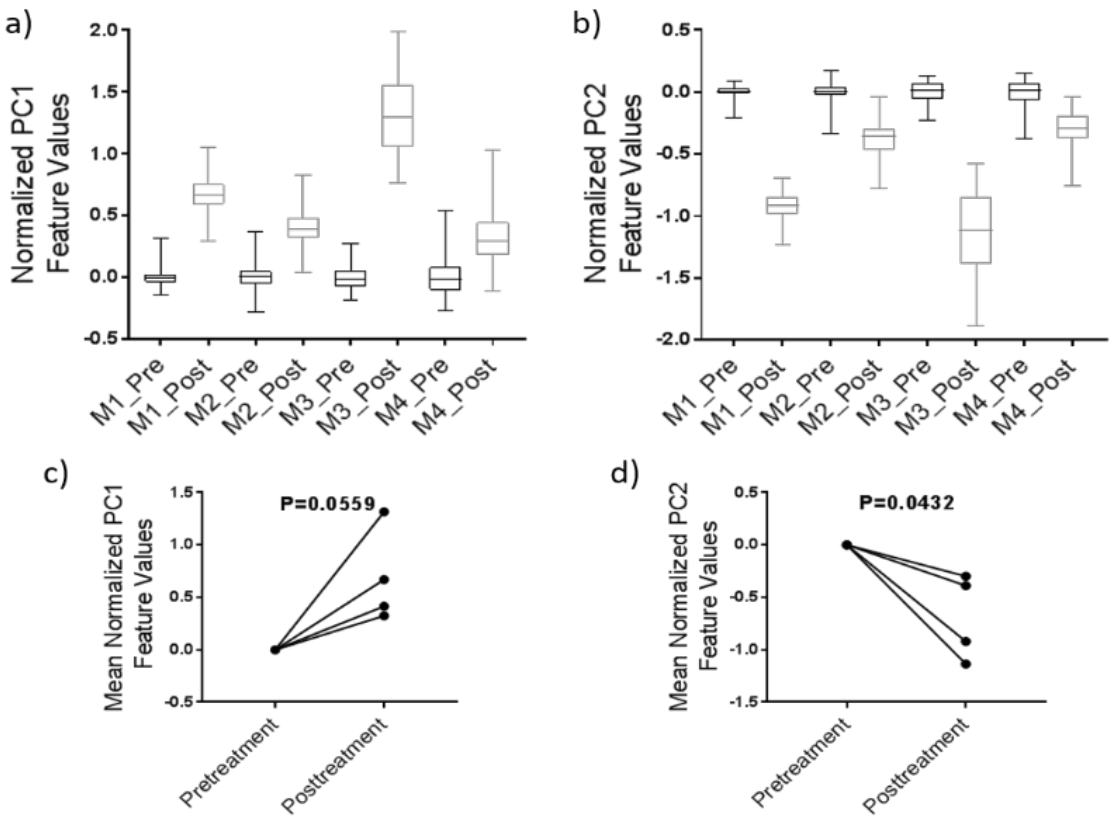

Figure 4-5: Box and whisker plots comparing the pre and two days posttreatment normalized (a) PC1 and (b) PC2 feature values for all four mice. The mean whole-tumor normalized (c) PC1 and (d) PC2 tissue values are shown along with the corresponding paired t-test. © 2020 IEEE

4.4.3 Automated assessment of SBRT TVR response

After observing distinctions between PC feature values before and after SBRT tumor treatments, we sought to create an automatic analysis process to quantify the degree of SBRT-induced TVR. To do this, pretreatment and posttreatment scatter plots of normalized PC1 and PC2 feature values were generated.

Tumor pixels were classified as non-responding, partially responding, or fully responding based on their pretreatment and posttreatment normalized PC1 and PC2 feature values unlikelihood. To perform this classification, a 99.9% confidence covariance ellipse was calculated for the pretreatment tumor pixels [135]. Posttreatment

tumor pixels were identified as tumor vascular response positive (TVR_{pos}) if they were outside of the confidence ellipse or tumor vascular response negative (TVR_{neg}) if they were inside the confidence ellipse. The classification algorithm identified mouse two as a partial responder with 86.5% of pixels being TVR_{pos} and mouse three as a complete responder with 100% TVR_{pos} pixels. The spatial location of TVR_{pos} and TVR_{neg} pixels were displayed for rapid identification of TVR spatial heterogeneity. Results demonstrate the ability of the classification algorithm to effectively measure TVR caused by SBRT (Figure 4-6).

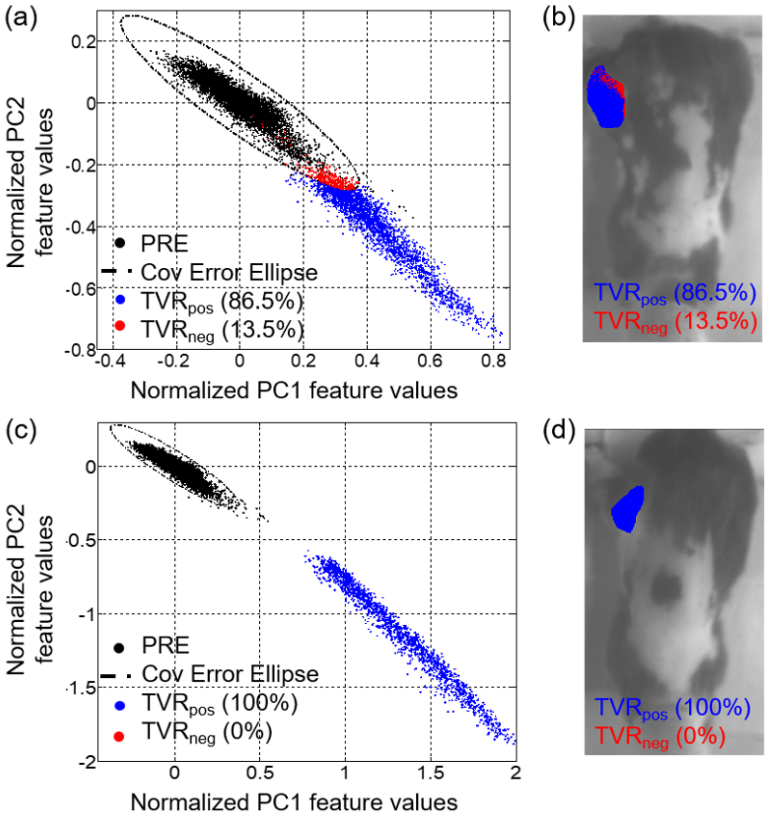

Figure 4-6: Automated classification of TVR using a confidence covariance Ellipse algorithm. Scatter plots of normalized PC1 and PC2 feature values for (a) mouse two and (c) mouse three are shown. The normalized PC feature values from pretreatment images (PRE) are shown as black dots. The classification algorithm calculated a 99.9% confidence covariance ellipse (dashed line) from pretreatment data, which was used to classify the posttreatment pixels as TVR_{pos} (blue) and TVR_{neg} (red). Ambient-light posttreatment images of (b) mouse two and (d) mouse three with the overlaid tumor ROI pixels classified as TVR_{pos} (blue) and TVR_{neg} (red) are shown.

4.5 Discussion

In this work we demonstrated the effects of SBRT on ICG tumor perfusion using longitudinal in vivo DynFI imaging and showed that SBRT leads to delayed clearance of tumor bound ICG. To our knowledge this is the first preclinical report using a multimodal theranostic system combined with automated analysis to monitor spatiotemporal TVR to SBRT. The effects of SBRT were quantified using PCA to assess TVR heterogeneity. Significant increases in PC1 and decreases in PC2 feature values were seen in treated mice. Principal component analysis was used to identify tumor pixels as TVR_{pos} and TVR_{neg}. Data acquisition and principal component analysis could be performed right after treatment and allows for rapid treatment and imaging without moving the animal. Rapid data acquisition and analysis of early TVR will help determine whether additional treatments are needed for tumor control. The developed system will enable correlation of TVR to metastatic and local tumor control during radiation therapy.

Dynamic Fluorescence imaging of ICG can detect changes in tissue perfusion. This is crucial in solid tumors where the efficiency of blood flow through the tumor likely contributes to the number of circulating tumor cells (CTCs) in the blood, potentially contributing to metastasis. The presence of functional tumor vasculature plays an integral role in the mobilization of CTCs [5]. The number of CTC's after radiation therapy are elevated, but significantly less in patients with hypofractionated radiation therapy compared to conventional radiation therapy [136, 137]. However the degree to which radiation therapy contributes to metastasis through the migration of irradiated tumor cells is of some debate, as irradiation has been shown to promote the growth of previously dormant metastatic clones through cellular signaling [138, 139]. Longitudinal observation

of tumor perfusion correlated to both CTCs and metastatic occurrence after SBRT will give further insight into this area.

The impact of vascular function on local tumor control post SBRT has recently been of much debate. Vascular damage with high-dose SBRT contributes to hypoxia and nutrient deprivation, but the degree to which this contributes to local tumor control has not been fully explored. It has been shown that high-dose single fraction SBRT has led to indirect cell death in multiple preclinical tumor types. Poor oxygen and nutrient perfusion as well as reperfusion injury have been proposed as causes of indirect cell death [110, 140]. However, other studies have observed that endothelial/stromal cell radiosensitivity had no influence on the amount of radiation needed to induce local tumor control of xenografted human tumors, but affected the regrowth rate of relapsed tumors [141]. Other studies have observed similar findings, but also found that increased tumor cell radiosensitivity resulted in increased tumor control [142, 143]. These studies demonstrate the importance of accurate measurements of tissue perfusion for radiation therapy related studies. Direct correlation between tissue perfusion and tumor control should be performed in multiple tumor types to understand the effects of radiation-induced TVR.

Current imaging modalities used to assess TVR in preclinical studies have some limitations [11]. For example, DCE MRI [144] and Nuclear Imaging [145] are expensive and require constraining scheduling for longitudinal preclinical imaging studies. Although already integrated into the irradiator, CT is limited by its low sensitivity and raises dose accumulation concerns [146]. Ultrasound, is user dependent, requires direct tissue contact and dedicated instrumentation [147]. As an alternative, we have presented a simple, low-cost optical technique as an add-on to a commercial CT-guided preclinical

irradiator for in vivo monitoring of the spatiotemporal TVR. The system can assess whole tumor vascular heterogeneity longitudinally in response to SBRT.

4.6 Conclusion

In conclusion, DynFI imaging will allow for longitudinal whole-tumor observations of early TVR and tumor perfusion. This will enable a better understanding of how the tumor vasculature affects metastasis, tumor growth, and local tumor control. Our recent study modeled from solid tumor data taken from QMPM imaging revealed radiation-induced vascular alterations may modulate hypoxia, adversely affecting tumor control probability in successive fractionated treatments [112]. DynFI imaging combined with QMPM will provide a novel set of tools to observe the relationship between the tumor vasculature, tissue perfusion, and local tumor control for conventional and hypofractionated radiation therapy.

Chapter 5: Summary and Future Work

5.1 Summary

In this work two novel DCE imaging systems capable of identifying longitudinal changes in the healthy and malignant vasculature during radiotherapy were developed. The development of L-QMPM allowed for a thorough characterization of the BMV that included observations of angiogenesis, poor perfusion, and decreased drug delivery to the leukemic bone marrow. Furthermore, the assessment of low and high dose RT showed transient increases in drug delivery several days after RT likely due to vasodilation and increased blood flow in mice bearing leukemia. Changes in drug delivery after RT increased cellular uptake of chemotherapy, leading to increased survival for mice bearing ALL in combination therapy. Results demonstrate the importance of the BMV in the outcome of leukemia treatments. A summary of the effects of leukemia and RT is shown in Figure 5-1.

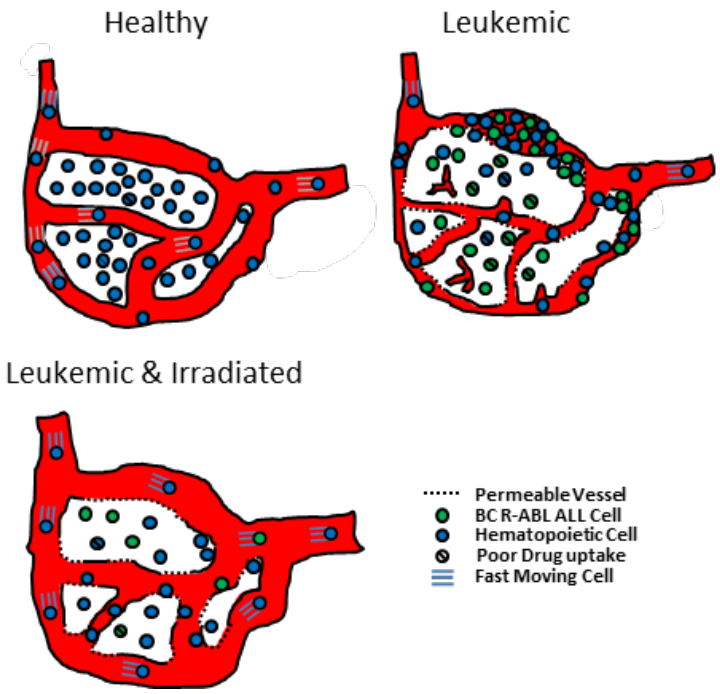

Figure 5-1: A diagram of the healthy, leukemic, and leukemic irradiated BMV showing changes in vascular morphology, blood flow, vascular permeability, and drug delivery between healthy mice, mice bearing leukemia, and mice bearing leukemia given RT.

Macroscopic DynFI enabled observations of early vascular changes during radiotherapy of solid tumors. The integration of this system into a commercial irradiator has the potential to allow for early observations (minutes to hours) of changes in the uptake and clearance of ICG after RT. The semi-automated analysis using PCA identified pixelwise changes in the uptake and clearance of ICG from solid tumors. DynFI with PCA represents a powerful tool that can be useful to rapidly identify changes in the tumor while preserving spatial information needed to understand the heterogeneity of the tumor vasculature.

5.2 Future Work

L-QMPM can perform direct validations of macroscopic DCE modeling through direct observation of the underlying vasculature. Several models exist for macroscopic DCE imaging [148], however the accuracy of such models has largely not been tested in a single platform capable of directly observing the underlying vascular structure while performing DCE imaging [47]. Future studies directly comparing L-QMPM imaging to DCE MRI may help better understand the differences between DCE imaging in the clinical and preclinical observations in the malignant bone marrow.

Potential biological applications for L-QMPM include 1) studying long term vascular damage and repair during hematological bone marrow transplant regimens [101] with radioprotectant therapeutics, 2) characterizing the BMV for different applications such as sickle cell disease, solid tumor metastasis, osteoporosis, or aging, and 3) studying the solid tumor vasculature in mice with the development of a window chamber [26] in combination with DynFI imaging.

Future work using DynFI macroscopic imaging should perform a thorough characterization of the changes in ICG uptake and clearance for standard fractionation and hypofractionated radiotherapy. This would allow for a powerful characterization of changes in the tumor vasculature and blood flow during treatment.

Bibliography

1. Bertout, J.A., S.A. Patel, and M.C. Simon, *The impact of O2 availability on human cancer.* Nature reviews. Cancer, 2008. **8**(12): p. 967-975.
2. Schaefer, C., et al., *Time-course-dependent microvascular alterations in a model of myeloid leukemia in vivo.* Leukemia, 2007. **22**: p. 59.
3. Passaro, D., et al., *Increased Vascular Permeability in the Bone Marrow Microenvironment Contributes to Disease Progression and Drug Response in Acute Myeloid Leukemia.* Cancer Cell, 2017. **32**(3): p. 324-341.e6.
4. Bergers, G. and L.E. Benjamin, *Tumorigenesis and the angiogenic switch.* Nature Reviews Cancer, 2003. **3**(6): p. 401-410.
5. Liotta, L.A., J. Kleinerman, and G.M. Saidel, *Quantitative Relationships of Intravascular Tumor Cells, Tumor Vessels, and Pulmonary Metastases following Tumor Implantation.* Cancer Research, 1974. **34**(5): p. 997.
6. Rockwell, S., et al., *Hypoxia and radiation therapy: past history, ongoing research, and future promise.* Current molecular medicine, 2009. **9**(4): p. 442-458.
7. Jordan, B.F. and P. Sonveaux, *Targeting tumor perfusion and oxygenation to improve the outcome of anticancer therapy.* Frontiers in pharmacology, 2012. **3**: p. 94-94.
8. Duarte, D., et al., *Inhibition of Endosteal Vascular Niche Remodeling Rescues Hematopoietic Stem Cell Loss in AML.* Cell Stem Cell.
9. Webster, R.M., *Combination therapies in oncology.* Nat Rev Drug Discov, 2016. **15**(2): p. 81-2.
10. Song, C.W., et al., *Indirect tumor cell death after high-dose hypofractionated irradiation: implications for stereotactic body radiation therapy and stereotactic radiation surgery.* International Journal of Radiation Oncology• Biology• Physics, 2015. **93**(1): p. 166-172.
11. Park, H.J., et al., *Radiation-Induced Vascular Damage in Tumors: Implications of Vascular Damage in Ablative Hypofractionated Radiotherapy (SBRT and SRS).* Radiation Research, 2012. **177**(3): p. 311-327.
12. Jain, R.K., *Normalization of Tumor Vasculature: An Emerging Concept in Antiangiogenic Therapy.* Science, 2005. **307**(5706): p. 58-62.
13. Goel, S., et al., *Normalization of the Vasculature for Treatment of Cancer and Other Diseases.* Physiological Reviews, 2011. **91**(3): p. 1071-1121.
14. Shah, D.K., *Pharmacokinetic and pharmacodynamic considerations for the next generation protein therapeutics.* Journal of pharmacokinetics and pharmacodynamics, 2015. **42**(5): p. 553-571.
15. Goel, S., A.H.-K. Wong, and R.K. Jain, *Vascular normalization as a therapeutic strategy for malignant and nonmalignant disease.* Cold Spring Harbor perspectives in medicine, 2012. **2**(3): p. a006486-a006486.
16. Bhattacharya, A., et al., *Tumor vascular maturation and improved drug delivery induced by methylselenocysteine leads to therapeutic synergy with anticancer drugs.*

Clinical cancer research : an official journal of the American Association for Cancer Research, 2008. **14**(12): p. 3926-3932.
17. Wildiers, H., et al., *Effect of antivascular endothelial growth factor treatment on the intratumoral uptake of CPT-11.* British journal of cancer, 2003. **88**(12): p. 1979-1986.
18. Stylianopoulos, T. and R.K. Jain, *Combining two strategies to improve perfusion and drug delivery in solid tumors.* Proceedings of the National Academy of Sciences of the United States of America, 2013. **110**(46): p. 18632-18637.
19. Gillies, R.J., et al., *Causes and effects of heterogeneous perfusion in tumors.* Neoplasia (New York, N.Y.), 1999. **1**(3): p. 197-207.
20. Sonveaux, P., *Provascular strategy: Targeting functional adaptations of mature blood vessels in tumors to selectively influence the tumor vascular reactivity and improve cancer treatment.* Radiotherapy and Oncology, 2008. **86**(3): p. 300-313.
21. Thews, O., D.K. Kelleher, and P.W. Vaupel, *Modulation of Spatial O2 Tension Distribution in Experimental Tumors by Increasing Arterial O2 Supply.* Acta Oncologica, 1995. **34**(3): p. 291-295.
22. Fukumura, D., et al., *Role of nitric oxide in tumor microcirculation. Blood flow, vascular permeability, and leukocyte-endothelial interactions.* The American journal of pathology, 1997. **150**(2): p. 713-725.
23. Song, C.W., *Effect of Local Hyperthermia on Blood Flow and Microenvironment: A Review.* Cancer Research, 1984. **44**(10 Supplement): p. 4721s.
24. Song, C.W. and S.H. Levitt, *Vascular Changes in Walker 256 Carcinoma of Rats Following X Irradiation.* Radiology, 1971. **100**(2): p. 397-407.
25. Wong, H.H., C.W. Song, and S.H. Levitt, *Early Changes in the Functional Vasculature of Walker Carcinoma 256 Following Irradiation.* Radiology, 1973. **108**(2): p. 429-434.
26. Demidov, V., et al., *Preclinical longitudinal imaging of tumor microvascular radiobiological response with functional optical coherence tomography.* Scientific Reports, 2018. **8**(1): p. 38.
27. Kleibeuker, E.A., et al., *Low dose angiostatic treatment counteracts radiotherapy-induced tumor perfusion and enhances the anti-tumor effect.* Oncotarget, 2016. **7**(47): p. 76613-76627.
28. Potiron, V.A., et al., *Improved functionality of the vasculature during conventionally fractionated radiation therapy of prostate cancer.* PloS one, 2013. **8**(12): p. e84076-e84076.
29. Goedegebuure, R.S.A., et al., *Combining Radiotherapy With Anti-angiogenic Therapy and Immunotherapy; A Therapeutic Triad for Cancer?* Frontiers in Immunology, 2019. **9**(3107).
30. Janssen, M.H.M., et al., *Tumor perfusion increases during hypofractionated short-course radiotherapy in rectal cancer: Sequential perfusion-CT findings.* Radiotherapy and Oncology, 2010. **94**(2): p. 156-160.
31. Sonveaux, P., et al., *Modulation of the tumor vasculature functionality by ionizing radiation accounts for tumor radiosensitization and promotes gene delivery.* The FASEB Journal, 2002. **16**(14): p. 1979-1981.
32. Marenzana, M. and T.R. Arnett, *The Key Role of the Blood Supply to Bone.* Bone Research, 2013. **1**(1): p. 203-215.
33. Hussong, J.W., G.M. Rodgers, and P.J. Shami, *Evidence of increased angiogenesis in patients with acute myeloid leukemia.* Blood, 2000. **95**(1): p. 309-313.

34. Konopleva, M., et al., *Phase I/II study of the hypoxia-activated prodrug PR104 in refractory/relapsed acute myeloid leukemia and acute lymphoblastic leukemia.* Haematologica, 2015. **100**(7): p. 927-934.
35. Ossenkoppele, G.J., et al., *Addition of bevacizumab to chemotherapy in acute myeloid leukemia at older age: a randomized phase 2 trial of the Dutch-Belgian Cooperative Trial Group for Hemato-Oncology (HOVON) and the Swiss Group for Clinical Cancer Research (SAKK).* Blood, 2012. **120**(24): p. 4706-4711.
36. Jain, P., et al., *FCR and bevacizumab treatment in patients with relapsed chronic lymphocytic leukemia.* Cancer, 2014. **120**(22): p. 3494-501.
37. Haibe, Y., et al., *Resistance Mechanisms to Anti-angiogenic Therapies in Cancer.* Frontiers in Oncology, 2020. **10**(221).
38. Aristei, C. and A. Tabilio, *Total-Body Irradiation in the Conditioning Regimens for Autologous Stem Cell Transplantation in Lymphoproliferative Diseases.* The Oncologist, 1999. **4**(5): p. 386-397.
39. Dombret, H. and C. Gardin, *An update of current treatments for adult acute myeloid leukemia.* Blood, 2016. **127**(1): p. 53-61.
40. Hui, S.K., et al., *Feasibility study of helical tomotherapy for total body or total marrow irradiation.* Med Phys, 2005. **32**(10): p. 3214-24.
41. Johnson, R.E., *Radiosensitivity of leukemic and nonleukemic lymphocytes.* Cancer Res, 1967. **27**(1): p. 39-42.
42. Cuenod, C.A. and D. Balvay, *Perfusion and vascular permeability: Basic concepts and measurement in DCE-CT and DCE-MRI.* Diagnostic and Interventional Imaging, 2013. **94**(12): p. 1187-1204.
43. Shih, T.T.-F., et al., *Bone marrow angiogenesis magnetic resonance imaging in patients with acute myeloid leukemia: peak enhancement ratio is an independent predictor for overall survival.* Blood, 2009. **113**(14): p. 3161.
44. Chu, S., et al., *Measurement of blood perfusion in spinal metastases with dynamic contrast-enhanced magnetic resonance imaging: evaluation of tumor response to radiation therapy.* Spine (Phila Pa 1976), 2013. **38**(22): p. E1418-24.
45. Zhu, J., et al., *Reduction of Longitudinal Vertebral Blood Perfusion and Its Likely Causes: A Quantitative Dynamic Contrast-enhanced MR Imaging Study of a Rat Osteoporosis Model.* Radiology, 2016. **282**(2): p. 369-380.
46. Bäuerle, T., et al., *Imaging anti-angiogenic treatment response with DCE-VCT, DCE-MRI and DWI in an animal model of breast cancer bone metastasis.* European Journal of Radiology, 2010. **73**(2): p. 280-287.
47. Faye, N., et al., *Dynamic Contrast Enhanced Optical Imaging of Capillary Leakage.* Technology in Cancer Research & Treatment, 2011. **10**(1): p. 49-57.
48. Tofts, P.S., *Modeling tracer kinetics in dynamic Gd-DTPA MR imaging.* Journal of Magnetic Resonance Imaging, 1997. **7**(1): p. 91-101.
49. Lassailly, F., et al., *Multimodal imaging reveals structural and functional heterogeneity in different bone marrow compartments: functional implications on hematopoietic stem cells.* Blood, 2013. **122**(10): p. 1730-1740.
50. Osmond, D.G. and N.B. Everett, *BONE MARROW BLOOD VOLUME AND TOTAL RED CELL MASS OF THE GUINEA-PIG AS DETERMINED BY 59-FE-ERYTHROCYTE DILUTION AND LIQUID NITROGEN FREEZING.* Q J Exp Physiol Cogn Med Sci, 1965. **50**: p. 1-14.
51. Daldrup, H.E., et al., *Monitoring radiation-induced changes in bone marrow histopathology with ultra-small superparamagnetic iron oxide (USPIO)-enhanced MRI.* Journal of Magnetic Resonance Imaging, 1999. **9**(5): p. 643-652.

52. Wang, K., et al., *MRI Study on the Changes of Bone Marrow Microvascular Permeability and Fat Content after Total-Body X-Ray Irradiation.* Radiat Res, 2018. **189**(2): p. 205-212.
53. Shih, T.T.F., et al., *Functional MR imaging of tumor angiogenesis predicts outcome of patients with acute myeloid leukemia.* Leukemia, 2006. **20**(2): p. 357-362.
54. Daldrup-Link, H.E., T. Henning, and T.M. Link, *MR imaging of therapy-induced changes of bone marrow.* European Radiology, 2007. **17**(3): p. 743-761.
55. Rafii, S., et al., *Regulation of Hematopoiesis by Microvascular Endothelium.* Leukemia & Lymphoma, 1997. **27**(5-6): p. 375-386.
56. Bixel, M.G., et al., *Flow Dynamics and HSPC Homing in Bone Marrow Microvessels.* Cell Reports, 2017. **18**(7): p. 1804-1816.
57. Jung, Y., et al., *Intravital Imaging of Mouse Bone Marrow: Hemodynamics and Vascular Permeability*, in *Intravital Imaging of Dynamic Bone and Immune Systems : Methods and Protocols*, M. Ishii, Editor. 2018, Springer New York: New York, NY. p. 11-22.
58. Benninger, R.K.P. and D.W. Piston, *Two-photon excitation microscopy for the study of living cells and tissues.* Current protocols in cell biology, 2013. **Chapter 4**: p. Unit-4.11.24.
59. Pendleton, E.G., et al., *Second harmonic generation characterization of collagen in whole bone.* Biomedical optics express, 2020. **11**(8): p. 4379-4396.
60. Pustylnikov, S., et al., *Targeting the C-type lectins-mediated host-pathogen interactions with dextran.* Journal of pharmacy & pharmaceutical sciences : a publication of the Canadian Society for Pharmaceutical Sciences, Societe canadienne des sciences pharmaceutiques, 2014. **17**(3): p. 371-392.
61. Egawa, G., S. Ono, and K. Kabashima, *Intravital Imaging of Vascular Permeability by Two-Photon Microscopy*, in *Animal Models of Allergic Disease: Methods and Protocols*, K. Nagamoto-Combs, Editor. 2021, Springer US: New York, NY. p. 151-157.
62. Vandoorne, K., et al., *Imaging the Vascular Bone Marrow Niche During Inflammatory Stress.* Circulation Research, 2018. **123**(4): p. 415-427.
63. Leunig, M., et al., *Angiogenesis, Microvascular Architecture, Microhemodynamics, and Interstitial Fluid Pressure during Early Growth of Human Adenocarcinoma LS174T in SCID Mice.* Cancer Research, 1992. **52**(23): p. 6553-6560.
64. Lipowsky, H.H. and B.W. Zweifach, *Application of the "two-slit" photometric technique to the measurement of microvascular volumetric flow rates.* Microvascular Research, 1978. **15**(1): p. 93-101.
65. Kim, D.-Y., et al., *Nilotinib combined with multiagent chemotherapy for newly diagnosed Philadelphia-positive acute lymphoblastic leukemia.* Blood, 2015. **126**(6): p. 746.
66. Manlove, L.S., et al., *Adaptive Immunity to Leukemia Is Inhibited by Cross-Reactive Induced Regulatory T Cells.* Journal of immunology (Baltimore, Md. : 1950), 2015. **195**(8): p. 4028-4037.
67. Raybuck, J.D., N.J. Hargus, and S.A. Thayer, *A GluN2B-Selective NMDAR Antagonist Reverses Synapse Loss and Cognitive Impairment Produced by the HIV-1 Protein Tat.* The Journal of Neuroscience, 2017. **37**(33): p. 7837-7847.
68. Schindelin, J., et al., *Fiji: an open-source platform for biological-image analysis.* Nature Methods, 2012. **9**: p. 676.
69. Carpenter, A.E., et al., *CellProfiler: image analysis software for identifying and quantifying cell phenotypes.* Genome Biology, 2006. **7**(10): p. R100.

70. Preibisch, S., S. Saalfeld, and P. Tomancak, *Globally optimal stitching of tiled 3D microscopic image acquisitions.* Bioinformatics, 2009. **25**(11): p. 1463-1465.
71. Otsu, N., *A Threshold Selection Method from Gray-Level Histograms.* IEEE Transactions on Systems, Man, and Cybernetics, 1979. **9**(1): p. 62-66.
72. van Hoof, S.J., P.V. Granton, and F. Verhaegen, *Development and validation of a treatment planning system for small animal radiotherapy: SmART-Plan.* Radiother Oncol, 2013. **109**(3): p. 361-6.
73. Faddegon, B.A., et al., *The accuracy of EGSnrc, Geant4 and PENELOPE Monte Carlo systems for the simulation of electron scatter in external beam radiotherapy.* Phys Med Biol, 2009. **54**(20): p. 6151-63.
74. Downes, P., et al., *Monte Carlo simulation and patient dosimetry for a kilovoltage cone-beam CT unit.* Med Phys, 2009. **36**(9): p. 4156-67.
75. Kumar, B., et al., *Acute myeloid leukemia transforms the bone marrow niche into a leukemia-permissive microenvironment through exosome secretion.* Leukemia, 2017.
76. Kabacik, S. and K. Raj, *Ionising radiation increases permeability of endothelium through ADAM10-mediated cleavage of VE-cadherin.* Oncotarget, 2017. **8**(47): p. 82049-82063.
77. Song, C.W., R.S. Anderson, and J. Tabachnick, *Early Effects of Beta Irradiation on Dermal Vascular Permeability to Plasma Proteins.* Radiation Research, 1966. **27**(4): p. 604-615.
78. Kusumbe, A.P., S.K. Ramasamy, and R.H. Adams, *Coupling of angiogenesis and osteogenesis by a specific vessel subtype in bone.* Nature, 2014. **507**: p. 323.
79. Tao, X., et al., *DCE-MRI Perfusion and Permeability Parameters as predictors of tumor response to CCRT in Patients with locally advanced NSCLC.* Scientific reports, 2016. **6**: p. 35569-35569.
80. O'Connor, J.P.B., et al., *Dynamic contrast-enhanced imaging techniques: CT and MRI.* The British journal of radiology, 2011. **84 Spec No 2**(Spec Iss 2): p. S112-S120.
81. Yurkiewicz, I.R., L. Muffly, and M. Liedtke, *Inotuzumab ozogamicin: a CD22 mAb-drug conjugate for adult relapsed or refractory B-cell precursor acute lymphoblastic leukemia.* Drug design, development and therapy, 2018. **12**: p. 2293-2300.
82. DasGupta, R.K., et al., *A review of CD19-targeted immunotherapies for relapsed or refractory acute lymphoblastic leukemia.* Journal of Oncology Pharmacy Practice, 2017. **24**(6): p. 453-467.
83. Ryman, J.T. and B. Meibohm, *Pharmacokinetics of Monoclonal Antibodies.* CPT: pharmacometrics & systems pharmacology, 2017. **6**(9): p. 576-588.
84. Wong, J.Y.C., et al., *Targeted Total Marrow Irradiation Using Three-Dimensional Image-Guided Tomographic Intensity-Modulated Radiation Therapy: An Alternative to Standard Total Body Irradiation.* Biology of Blood and Marrow Transplantation, 2006. **12**(3): p. 306-315.
85. Hui, S., et al., *Early assessment of dosimetric and biological differences of total marrow irradiation versus total body irradiation in rodents.* Radiotherapy and Oncology, 2017. **124**(3): p. 468-474.
86. Stein, A., et al., *Phase I Trial of Total Marrow and Lymphoid Irradiation Transplant Conditioning in Patients with Relapsed/Refractory Acute Leukemia.* Biology of Blood and Marrow Transplantation, 2017.
87. Gill, J.H., et al., *Vascular Disrupting Agents in cancer treatment: Cardiovascular toxicity and implications for co-administration with other cancer chemotherapeutics.* Pharmacology & Therapeutics, 2019.

88. Quesada, A.R., M.A. Medina, and E. Alba, *Playing only one instrument may be not enough: limitations and future of the antiangiogenic treatment of cancer.* Bioessays, 2007. **29**(11): p. 1159-68.
89. Moserle, L., G. Jimenez-Valerio, and O. Casanovas, *Antiangiogenic therapies: going beyond their limits.* Cancer Discov, 2014. **4**(1): p. 31-41.
90. Kleibeuker, E.A., et al., *Optimal treatment scheduling of ionizing radiation and sunitinib improves the antitumor activity and allows dose reduction.* Cancer Medicine, 2015. **4**(7): p. 1003-1015.
91. Klug, F., et al., *Low-Dose Irradiation Programs Macrophage Differentiation to an iNOS+/M1 Phenotype that Orchestrates Effective T Cell Immunotherapy.* Cancer Cell, 2013. **24**(5): p. 589-602.
92. Atallah, E., et al., *Establishment of baseline toxicity expectations with standard frontline chemotherapy in acute myelogenous leukemia.* Blood, 2007. **110**(10): p. 3547-3551.
93. Kaveh, K., et al., *Combination therapeutics of Nilotinib and radiation in acute lymphoblastic leukemia as an effective method against drug-resistance.* PLOS Computational Biology, 2017. **13**(7): p. e1005482.
94. Brooks, J., et al., *Biophysical Characterization of the Leukemic Bone Marrow Vasculature Reveals Benefits of Neoadjuvant Low-Dose Radiation Therapy.* International Journal of Radiation Oncology, Biology, Physics, 2021. **109**(1): p. 60-72.
95. Dewhirst, M.W. and T.W. Secomb, *Transport of drugs from blood vessels to tumour tissue.* Nature reviews. Cancer, 2017. **17**(12): p. 738-750.
96. Hossain, D.M.S., et al., *Leukemia cell–targeted STAT3 silencing and TLR9 triggering generate systemic antitumor immunity.* Blood, 2014. **123**(1): p. 15-25.
97. Moehler, T.M., et al., *Bone marrow microcirculation analysis in multiple myeloma by contrast-enhanced dynamic magnetic resonance imaging.* International Journal of Cancer, 2001. **93**(6): p. 862-868.
98. Hlatky, L., P. Hahnfeldt, and J. Folkman, *Clinical Application of Antiangiogenic Therapy: Microvessel Density, What It Does and Doesn't Tell Us.* JNCI: Journal of the National Cancer Institute, 2002. **94**(12): p. 883-893.
99. Gyurkocza, B. and B.M. Sandmaier, *Conditioning regimens for hematopoietic cell transplantation: one size does not fit all.* Blood, 2014. **124**(3): p. 344-353.
100. Le, V.-H., et al., *In vivo longitudinal visualization of bone marrow engraftment process in mouse calvaria using two-photon microscopy.* Scientific Reports, 2017. **7**(1): p. 44097.
101. Slayton, W.B., et al., *The Role of the Donor in the Repair of the Marrow Vascular Niche Following Hematopoietic Stem Cell Transplant.* STEM CELLS, 2007. **25**(11): p. 2945-2955.
102. Grabham, P., et al., *Effects of ionizing radiation on three-dimensional human vessel models: differential effects according to radiation quality and cellular development.* Radiat Res, 2011. **175**(1): p. 21-8.
103. Park, M.-T., et al., *The radiosensitivity of endothelial cells isolated from human breast cancer and normal tissue in vitro.* Microvascular Research, 2012. **84**(2): p. 140-148.
104. Chen, F.-H., et al., *Combination of Vessel-Targeting Agents and Fractionated Radiation Therapy: The Role of the SDF-1/CXCR4 Pathway.* International Journal of Radiation Oncology, Biology, Physics, 2013. **86**(4): p. 777-784.

105. Wachsberger, P., R. Burd, and A.P. Dicker, *Tumor Response to Ionizing Radiation Combined with Antiangiogenesis or Vascular Targeting Agents.* Exploring Mechanisms of Interaction, 2003. **9**(6): p. 1957-1971.
106. Saunders, M., et al., *Continuous, hyperfractionated, accelerated radiotherapy (CHART) versus conventional radiotherapy in non-small cell lung cancer: mature data from the randomised multicentre trial.* Radiotherapy and Oncology, 1999. **52**(2): p. 137-148.
107. Brown, J.M. and A.C. Koong, *High-Dose Single-Fraction Radiotherapy: Exploiting a New Biology?* International Journal of Radiation Oncology*Biology*Physics, 2008. **71**(2): p. 324-325.
108. Sperduto, P.W., et al., *A hypothesis: indirect cell death in the radiosurgery era.* Int J Radiat Oncol Biol Phys, 2015. **91**(1): p. 11-3.
109. Song, C.W., et al., *Is indirect cell death involved in response of tumors to stereotactic radiosurgery and stereotactic body radiation therapy?* Int J Radiat Oncol Biol Phys, 2014. **89**(4): p. 924-5.
110. Song, C.W., et al., *Radiobiology of stereotactic body radiation therapy/stereotactic radiosurgery and the linear-quadratic model.* Int J Radiat Oncol Biol Phys, 2013. **87**(1): p. 18-9.
111. Brown, J.M., D.J. Carlson, and D.J. Brenner, *The tumor radiobiology of SRS and SBRT: are more than the 5 Rs involved?* Int J Radiat Oncol Biol Phys, 2014. **88**(2): p. 254-62.
112. LINDBLOM, E.K., et al., *Radiation-induced Vascular Damage and the Impact on the Treatment Outcome of Stereotactic Body Radiotherapy.* Anticancer research, 2019. **39**(6): p. 2721-2727.
113. Marshall, M.V., et al., *Near-infrared fluorescence imaging in humans with indocyanine green: a review and update.* Open surgical oncology journal (Online), 2010. **2**(2): p. 12.
114. Hong, G., et al., *Through-skull fluorescence imaging of the brain in a new near-infrared window.* Nature Photonics, 2014. **8**(9): p. 723.
115. Hong, G., et al., *Near-infrared II fluorescence for imaging hindlimb vessel regeneration with dynamic tissue perfusion measurement.* Circulation: Cardiovascular Imaging, 2014. **7**(3): p. 517-525.
116. Keller, E., et al., *Estimation of cerebral oxygenation and hemodynamics in cerebral vasospasm using indocyaningreen dye dilution and near infrared spectroscopy: a case report.* Journal of neurosurgical anesthesiology, 2001. **13**(1): p. 43-48.
117. Leung, T.S., et al., *Theoretical investigation of measuring cerebral blood flow in the adult human head using bolus Indocyanine Green injection and near-infrared spectroscopy.* Applied optics, 2007. **46**(10): p. 1604-1614.
118. Fischer, T., et al., *Detection of rheumatoid arthritis using non-specific contrast enhanced fluorescence imaging.* Academic radiology, 2010. **17**(3): p. 375-381.
119. Kang, Y., et al., *Segmental analysis of indocyanine green pharmacokinetics for the reliable diagnosis of functional vascular insufficiency.* Journal of biomedical optics, 2011. **16**(3): p. 030504.
120. Kang, Y., et al., *Dynamic fluorescence imaging of indocyanine green for reliable and sensitive diagnosis of peripheral vascular insufficiency.* Microvascular research, 2010. **80**(3): p. 552-555.
121. Seo, J., et al., *Principal component analysis of dynamic fluorescence images for diagnosis of diabetic vasculopathy.* Journal of biomedical optics, 2016. **21**(4): p. 046003.

122. Ntziachristos, V., et al., *Concurrent MRI and diffuse optical tomography of breast after indocyanine green enhancement.* Proc Natl Acad Sci U S A, 2000. **97**(6): p. 2767-72.
123. Lin, Y., et al., *Tumor characterization in small animals using magnetic resonance-guided dynamic contrast enhanced diffuse optical tomography.* J Biomed Opt, 2011. **16**(10): p. 106015.
124. Unlu, M.B., O. Birgul, and G. Gulsen, *A simulation study of the variability of indocyanine green kinetics and using structural a priori information in dynamic contrast enhanced diffuse optical tomography (DCE-DOT).* Phys Med Biol, 2008. **53**(12): p. 3189-200.
125. Hillman, E.M. and A. Moore, *All-optical anatomical co-registration for molecular imaging of small animals using dynamic contrast.* Nat Photonics, 2007. **1**(9): p. 526-530.
126. Bruns, O.T., et al., *Next-generation in vivo optical imaging with short-wave infrared quantum dots.* Nature biomedical engineering, 2017. **1**(4): p. 0056.
127. Mohajerani, P., et al., *Spatiotemporal analysis for indocyanine green-aided imaging of rheumatoid arthritis in hand joints.* Journal of biomedical optics, 2013. **18**(9): p. 097004.
128. Welsher, K., S.P. Sherlock, and H. Dai, *Deep-tissue anatomical imaging of mice using carbon nanotube fluorophores in the second near-infrared window.* Proceedings of the National Academy of Sciences, 2011. **108**(22): p. 8943-8948.
129. Wang, X. and K.K. Paliwal, *Feature extraction and dimensionality reduction algorithms and their applications in vowel recognition.* Pattern recognition, 2003. **36**(10): p. 2429-2439.
130. Kim, M.-S., et al., *Radiobiological mechanisms of stereotactic body radiation therapy and stereotactic radiation surgery.* Radiation oncology journal, 2015. **33**(4): p. 265-275.
131. Judd, N.P., et al., *Comparative analysis of tumor-infiltrating lymphocytes in a syngeneic mouse model of oral cancer.* Otolaryngology--Head and Neck Surgery, 2012. **147**(3): p. 493-500.
132. Lin, Y., et al., *Quantitative fluorescence tomography using a combined tri-modality FT/DOT/XCT system.* Optics Express, 2010. **18**(8): p. 7835–7850.
133. Nouizi, F., et al., *A thermo-sensitive fluorescent agent based method for excitation light leakage rejection for fluorescence molecular tomography.* Physics in medicine and biology, 2018.
134. Dogdas, B., et al., *Digimouse: a 3D whole body mouse atlas from CT and cryosection data.* Phys Med Biol, 2007. **52**(3): p. 577-87.
135. Dehlholm, C., P.B. Brockhoff, and W.L. Bredie, *Confidence ellipses: A variation based on parametric bootstrapping applicable on multiple factor analysis results for rapid graphical evaluation.* Food Quality and Preference, 2012. **26**(2): p. 278-280.
136. Oweida, A., et al., *Hypofractionated Radiotherapy Is Superior to Conventional Fractionation in an Orthotopic Model of Anaplastic Thyroid Cancer.* Thyroid, 2018. **28**(6): p. 739-747.
137. Martin, O.A., et al., *Mobilization of Viable Tumor Cells Into the Circulation During Radiation Therapy.* International Journal of Radiation Oncology*Biology*Physics, 2014. **88**(2): p. 395-403.
138. Martin, O.A., et al., *Does the mobilization of circulating tumour cells during cancer therapy cause metastasis?* Nature Reviews Clinical Oncology, 2016. **14**: p. 32.
139. Camphausen, K., et al., *Radiation Therapy to a Primary Tumor Accelerates Metastatic Growth in Mice.* Cancer Research, 2001. **61**(5): p. 2207.

140. Bodo, S., et al., *Single-dose radiotherapy disables tumor cell homologous recombination via ischemia/reperfusion injury.* J Clin Invest, 2019. **129**(2): p. 786-801.
141. Budach, W., et al., *Impact of stromal sensitivity on radiation response of tumors.* J Natl Cancer Inst, 1993. **85**(12): p. 988-93.
142. Torok, J.A., et al., *Deletion of Atm in Tumor but not Endothelial Cells Improves Radiation Response in a Primary Mouse Model of Lung Adenocarcinoma.* Cancer Res, 2019. **79**(4): p. 773-782.
143. Castle, K.D. and D.G. Kirsch, *Establishing the Impact of Vascular Damage on Tumor Response to High-Dose Radiation Therapy.* Cancer Research, 2019: p. canres.1323.2019.
144. Zahra, M.A., et al., *Dynamic contrast-enhanced MRI as a predictor of tumour response to radiotherapy.* The lancet oncology, 2007. **8**(1): p. 63-74.
145. Rafat, M., R. Ali, and E.E. Graves, *Imaging radiation response in tumor and normal tissue.* American journal of nuclear medicine and molecular imaging, 2015. **5**(4): p. 317.
146. Clark, D. and C. Badea, *Micro-CT of rodents: state-of-the-art and future perspectives.* Physica medica, 2014. **30**(6): p. 619-634.
147. Kasoji, S.K., et al., *Early assessment of tumor response to radiation therapy using high-resolution quantitative microvascular ultrasound imaging.* Theranostics, 2018. **8**(1): p. 156.
148. Sourbron, S.P. and D.L. Buckley, *Classic models for dynamic contrast-enhanced MRI.* NMR in Biomedicine, 2013. **26**(8): p. 1004-1027.